Dissertation

submitted to the
Combined Faculties for the Natural Sciences and for Mathematics
of the Ruperto-Carola University of Heidelberg, Germany
for the degree of

Doctor of Natural Sciences

Put forward by

Dipl. Phys. Thomas Kaindl

Born in Ingolstadt an der Donau, Germany

Oral examination: 2nd February 2011

Control of Specific Cell Response with Strongly Correlated Functional Domains Embedded in Supported Membranes

Referees:
Prof. Dr. Motomu Tanaka
Prof. Dr. Rasmus Schröder

Zusammenfassung

Höchst gleichförmige und stark korrelierte Domänen, bestehend aus vollständig fluorinierten Lipiden, wurden in Festkörpergestütze Lipidmembranen eingebaut. Die systematische Charakterisierung der fluorinierten Lipide zeigte eine signifikante Abhängigkeit des Domänengleichgewichtsradius von der Länge der Fluorkohlenstoffketten. Dies konnte im Rahmen der gleichwertigen Dipolmomentstheorie quantitativ erklärt werden. Eine Analyse der gleichverteilten Domänen mit enger Größenverteilung und die präzise Bestimmung von molekularen Strukturparametern durch Röntgen-Beugungsmessungen unter streifendem Einfall ermöglichte es, die Korrelationen zwischen den Domänen als eine zwei-dimensionale Kristallisation von Kolloiden zu behandeln. Weiterhin konnten die Kopfgruppen der fluorinierten Lipide mit α-D-Mannose und einem spezifischen Liganden eines Apoptose verursachenden Rezeptors (CD95L) modifiziert werden. Beide biofunktionale, in die Membran eingebundene Moleküle zeigten spezifische Wechselwirkungen mit ausgewählten Zellen, die einen eindeutigen Einfluss der örtlichen Eingrenzung von Domänen auf das dynamische Ausbreiten von Makrophagen und der Apotose von Krebszellen haben. Die gewonnenen Ergebnisse verdeutlichen, dass synthetisch entwickelte Lipidanker als Grundbausteine zur Bildung von biofunktionalen Mikro- und Nano-Domänen benutzt werden können, um somit das statische und dynamische Zellverhalten eindeutig zu regulieren.

◊

Abstract

Highly uniform and strongly correlated domains of synthetic, fluorinated lipids were incorporated into solid supported lipid membranes. The systematic characterization of variable fluorinated lipid domains revealed a significant dependence of the equilibrium radius of domains on the length of fluorocarbon chains. This can be quantitatively explained within the theoretical framework of an equivalent dipole model. An analysis of the mono–dispersive domains with narrow size distributions and the precise determination of molecular structure parameters with grazing–incidence X-ray diffraction measurements enabled treatment of the inter–domain correlations as two–dimensional colloidal crystallization and calculation of the potential of mean force. Furthermore, the head groups of fluorinated lipids can be modified with α–D–mannose and the specific ligand for an apoptosis receptor (CD95L). Both biofunctional molecules attached to the membranes showed specific interactions with target cells, revealing a significant influence of the lateral confinement of domains on the dynamic spreading of macrophages and cancer cell apoptosis. The obtained results demonstrate that synthetically designed lipid anchors can be used as building blocks to create biofunctional micro-/nano- domains for the quantitative regulation of the static and dynamic behavior of cells.

Danksagung

Die vorliegende Arbeit entstand im Rahmen des von der Landesgraduiertenförderung des Landes Baden-Württemberg geförderten Graduiertenkollegs "Molecular machines: mechanisms and functional interconnections" am Zentrum für Quantitative Biology (BIOQUANT). Für das mir gewährte Heinz Götze Memorial Stipendium möchte ich mich an dieser Stelle bedanken.

Mein ganz besonderer Dank gilt Prof. Dr. Motomu Tanaka, der mir als Betreuer und wichtiger Ratgeber jederzeit helfend zur Seite stand und mir diese Arbeit auch durch seine finanzielle Unterstützung ermöglichte.

Weiterhin danke ich Prof. Dr. Rasmus Schröder für die freundliche und sehr schnelle Bereitschaft als Gutachter dieser Arbeit zu fungieren.

Ein besonderer Dank gilt Dr. Andreea Pasc für die Synthetisierung der in dieser Arbeit verwendeten fluorinierten Lipide sowie Dr. Christian Gege für das Modifizieren von Lipiden.

Ein großer Dank gilt natürlich allen aktuellen und ehemaligen Mitgliedern der Arbeitsguppe. Dabei seien Dr. Jochen Ölke für die Wissensvermittlung im Umgang mit fluorinierten Lipiden zu Beginn meiner Arbeit, sowie Dr. Emanuel Schneck, Dr. Peter Seitz, Dr. Thomas Schubert, Dr. Stefan Kaufmann und PhD. Hiroshi Yoshikawa für die vielen anregenden wissenschaftlichen Diskussionen und ihre freundliche Unterstützung mit angeführt. Das tägliche Laborleben wurde sowohl wissenschaftlich, als auch sozial immens von Dr. Murat Tutus, Dr. Fernanda Rossetti, Harden Rieger, Alexander Körner, Wasim Abuillan, PhD. Murat Kazanci, Moritz Hermann und Marco Pascucci bereichert. Allen hier genannten Korrekturlesern/innen dieser Arbeit gilt nochmals ein besonderer Dank!

Für wissenschaftliche Unterstützung bedanke ich mich bei PD Dr. Ana Martin-Villalba (Deutsches Krebsforschungszentrum, Heidelberg) für das erfolgreiche und interessante Kooperationsprojekt und die Bereitstellung von "Todes Rezeptor"-Liganden, sowie bei Dr. Susanne Kleber und Berk Aykut für die Hilfe bei der Krebszellenkultivierung, zudem bei Dr. Ulrike Engel (Nikon Imaging Center, BIOQUANT) für die Einführung in die konfokale Mikroskopietechnik, bei Dr. Oleg Konovalov (European Synchrotron Radiation Facility, Grenoble) und Dr. Sérgio Funari (Hamburger Synchrotronstrahlungslabor am DESY) für die Unterstützung an den Beamlines, bei Prof. Dr. Achim Wixforth (Universität Augsburg) für die Zusammenarbeit in der Mikrofluidik, und bei Prof. David Pink (St. Francis Xavier University, Antigonish, Kanada) für die wissenschaftliche Inspiration und das Korrekturlesen.

Schließlich danke ich auch ganz besonders meinen Eltern und Brüdern für ihre Unterstützung die sie mir während meines gesamten Studiums gewährt haben!

Contents

1. Introduction

One of the fundamental principles that governs the formation of structures in biological systems is self–organization. In nature, the formation of assemblies and confined patterns is ubiquitous on multiple length scales. On the cellular level, i.e., the basic unit of life, plasma membranes define the boundary between extracellular environments and cytosolic compartments (Lodish et al., 2001). They consist mainly of lipids and integral proteins. The extracellular surface of the membrane is covered with carbohydrates, while the cytoplasmic surface is connected to the cytoskeleton. Moreover, there are many membrane compartments, such as organelles or vesicles that facilitate transport, recognition and communication across the membrane. This is the basic requisite of cells to maintain vital functions such as signal transduction, cell adhesion, or endocytotic trafficking.

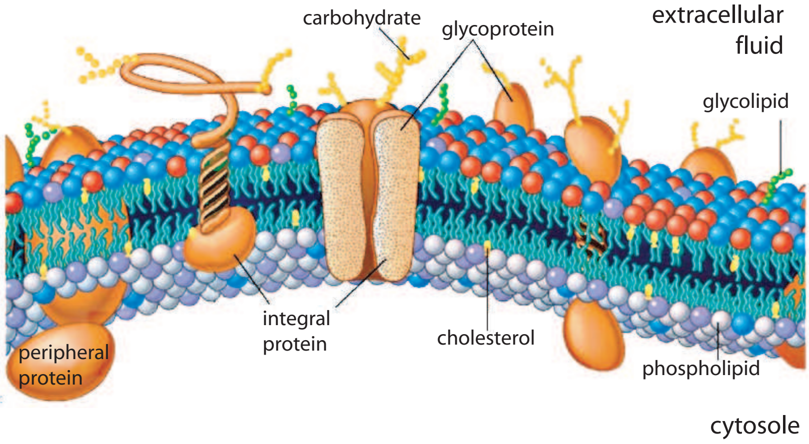

Figure 1.1.: Schematic illustration of the plasma membrane of a cell, adapted from Karp (2005)

A generally accepted structural model for the composition of the plasma membrane is the so-called *fluid–mosaic model* proposed by Singer and Nicolson (1972) and later refined by Jacobson et al. (1995, 2007). The core structure is a bilayer composed of various lipids and cholesterol (see Figure 1.1). A lipid molecule is amphiphilic and consists of a hydrophilic head group region and two hydrophobic hydrocarbon chains. In an aqueous environment, the lipids self–assemble into bilayers to minimize contact between polar solvent molecules and hydrophobic (non–polar)

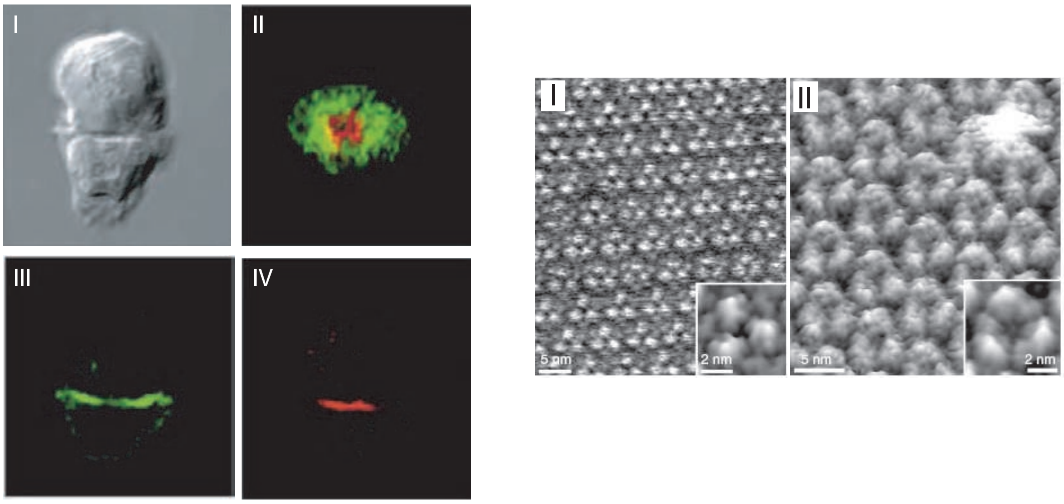

(a) (b)

Figure 1.2.: (a) Bright field image of a T–cell in contact with an antigen-presenting cell (I). Confocal images labeled for talin (green) and protein kinase C (red) in (II) overlaid cross sectional view, and (III–IV) single channel horizontal cut. Both proteins are present in two distinct domains (Monks et al., 1998). (b) Crystalline–like cluster of bacteriorhodopsin in purple membrane imaged by atomic force microscopy from (I) extracellular, and (II) cytoplasimc surface (Müller and Engel, 2007).

lipid chains. This so–called hydrophobic effect (Tanford, 1978) is entropy–driven and determines the thermodynamic equilibrium between lipids in solution and those in the membrane. The fluid bilayer serves as a two–dimensional matrix of integral proteins and a broad variety of proteins coupled to phosphatidylinositol anchors. The intrinsic fluidity of lipid membranes enables lipid molecules and proteins to freely diffuse in the membrane.

As a result of the membrane fluidity, incorporated proteins and lipids do not need to distribute uniformly, but can form local aggregates and domains. The formation of protein clusters and lipid rafts can be relatively dynamic, e.g., the formation of ligand–receptor pairs at immunological synaptic junctions (Figure 1.2a), or static, e.g., the clusters of bacteriorhodopsin in purple membrane (Figure 1.2b). A distinctive feature of these domains is that they facilitate essential membrane functions and can enhance cooperative functions (Mammen et al., 1998). Lipid monolayers that display functional domains can be transferred onto a solid substrate to form so–called supported membranes (Tanaka and Sackmann, 2005). They can be used as a quantitative cell surface model to study the effect of a local density of functional molecules on cellular functions. The complexity of embedded molecular structures makes it difficult to directly investigate and describe their interactions. Accordingly, the design of biomimetic model membranes with a reduced number of components is desirable.

A common strategy to reconstitute artificial domains in model membranes relies on mixtures of sphingolipids, cholesterol (chol), and phospholipids. They form immiscible domains as liquid ordered phases surrounded by liquid disordered phases of phospholipids (Rietveld and Simons, 1998). However, the use of complex lipid mixtures often results in a highly polydispersive domain size distribution and domains with ill-defined shapes (Figure 1.3). Such inhomogeneous domains, whose diameters are often comparable to those of cells, cannot be used as well defined sub-cellular structures to regulate cell behaviors.

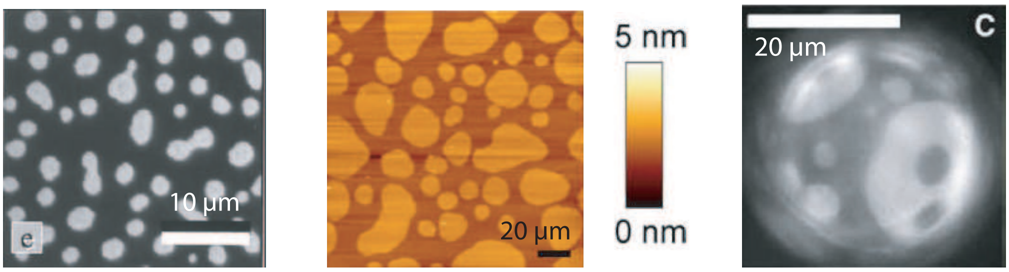

(a) (b) (c)

Figure 1.3.: (a) Fluorescence micrography of sphingomyelin:chol:POPC 1:2:2 domains (Dietrich et al., 2001). (b) Membrane composed of sphingomyelin:chol:DOPC 1:2:2 imaged by atomic force microscopy (García-Sáez and Schwille, 2010). (c) Fluorescence micrography of a giant unilamellar vesicle containing 1:4 diPhyPC:SOPC + $40\,\%$ cholesterol (Veach et al., 2006).

The main goal of this thesis is to design a new class of functional domains based on a binary mixture of phospholipids and synthetic (thus not naturally occurring) lipids with fluorinated chains. This simplification of the biomimetic system on a two component lipid system enables one to draw a simpler and better-defined phase diagram, where the size of domains is regulated by the chemical structure of incorporated lipids. Owing to their unique hydrophobic and oleophobic nature, the fluorinated lipid phase is completely separated from the phospholipid matrix. In recent years, surfactants with partially fluoroalkylated chains have proven their biocompatibility for medical applications, e.g. drug delivery (Riess, 2002). Gege et al. (2004) demonstrate that partially fluoroalkylated lipids with sLe^X head groups can be utilized to regulate the adhesion of Chinese hamster ovarial cells expressing E-selectin, but need a higher degree of fluorination to form well-defined microdomains. In this study, a set of custom–designed, fully perfluorinated lipids with variable head group functions (synthesized by Dr. Andreea Pasc, Université Henri

Poincaré, Nancy, France) have been used as an alternative to biological "raft" mixtures in order to stimulate the highly dynamic response of cells.

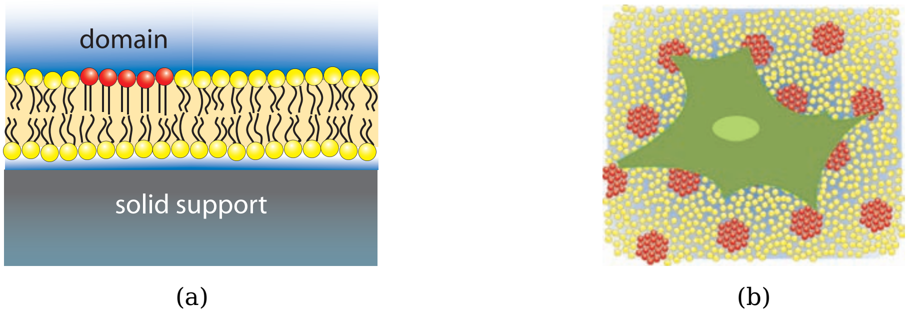

(a)

(b)

Figure 1.4.: Schematic illustration of the supported membrane that (a) locally displays domains of fluorinated lipids and (b) induces cellular response.

Micro- and nano- domains with a narrow, mono–disperse size distribution initially formed under thermodynamic equilibrium at the air–water interface can be transferred onto planar solid supports. Fourier transforms of fluorescence images and self–written analysis routines were used to deduce characteristic length scales and autocorrelations of micro–domains. To quantitatively determine the size of nano–domains below optical resolution and the short range intermolecular interactions, grazing incidence X-ray diffraction (GIXD) experiments with an analyzer crystal were carried out. The precise control of chemical structures and the measurement of structural parameters (e.g. lateral dipole density, tilt angle, molecular length) enabled the equilibrium domain size to be quantitatively accounted within the framework of the equivalent dipole theory. Moreover, the correlation between highly uniform, fluorinated lipid domains in a fluid lipid matrix can be related to the two–dimensional crystallization of colloids. Stable and well controlled domains can be further functionalized with a variety of biofunctional molecules, such as carbohydrate and peptide moieties, for specific recognition. In this thesis, supported membranes displaying micro-/nano- domains of fluorinated lipids were modified with α–D–mannose and the specific ligand for an apoptosis receptor (CD95L). The specific cell response on supported membranes displaying laterally confined domains can be analyzed with three-dimensional image reconstruction of cells by confocal microscopy and with reflection interference contrast microscopy. Details of the results will be presented in the following chapters.

2. Materials and Experimental Techniques

This chapter lists all utilized materials and chemicals, and presents a short description of the most important experimental setups which were used in this thesis. In addition, protocols for cell culturing and sample preparation are explained.

2.1. Fluorinated Compounds

The fluorinated amphiphilic molecules used in this thesis were synthesized by Dr. Andréea Pasc (Université Henri Poincaré, Nancy, France). The chemical structures of all fluorinated molecules are shown in Figure 2.1. Details about the synthesis can be found in Section A.1 and Kaindl et al. (2010); Oelke et al. (2008). The perfluorinated carbon chains of FLn molecules have varying carbon chain lengths (n = 10, 13, and 17), and are symmetrically connected to glycerol backbones. To study the impact of carbohydrate ligands on cell adhesion behavior, the hydroxy–headgroup of FL10Man molecules was replaced by an α-D-mannose monomer. On the hFL17 molecules, the glycerol backbone was replaced by a beta glutamic acid providing a free amine for further modification. This headgroup was acetylated for acFL17 molecules by Dr. Christian Gege (University Heidelberg, Germany). btnFL17 molecules provide a flexible molecular linker, where a short aminohexanoic acid-spacer carrying biotin at its end is attached to the headgroup.

2.2. Solvents and Chemicals

Purified water was always freshly drawn with a specific electrical resistance greater than $18\,\mathrm{M\Omega\,cm}$. The used water purification system from TKA (TKA GenPure, Niederelbert, Germany) was equipped with a UV lamp and ensured a total organic carbon content (TOC) below 6 ppb upon drawing. All organic solvents including Freon® 113 (1,1,2-trichloro-1,2,2-trifluoroethane) were obtained in absolute concentration from the center of chemistry at the University Heidelberg (Germany). If not stated otherwise, all other chemicals, including perfluorohexan and methylperfluorobutan were purchased from Sigma-Aldrich (Munich, Germany) and used without further purification.

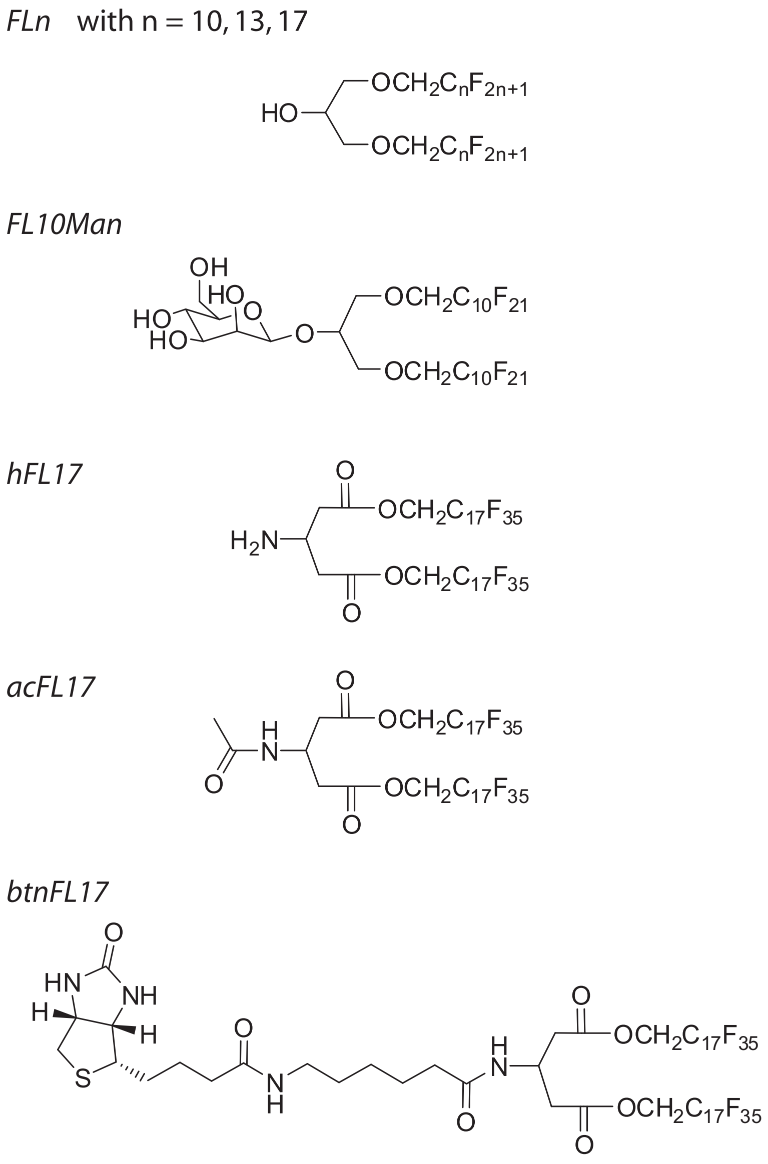

FLn with n = 10, 13, 17

FL10Man

hFL17

acFL17

btnFL17

Figure 2.1.: Structural formulas of fluorinated molecules used in this study.

1,2-dioleoyl-*sn*-glycero-3-phophocholine (DOPC) lipids with unsaturated hydrocarbon chains were ordered from Avanti Polar Lipids (Alabaster, AL, USA). DOPC has its main transition temperature at $-16.5\,°\mathrm{C}$ (Silvius and McElhaney, 1979; Ulrich et al., 1994) and remains in the liquid-crystalline lamellar phase L_α (Phillips et al., 1969) under all experimental conditions. For cell adhesion experiments (Section 7.2), a head group modified lipid with a flexible biotin tag, 1,2-dioleoyl-*sn*-glycero-3-phosphoethanolamine-N-(cap biotinyl) (DOPE-btn) from Avanti Polar Lipids (Alabaster, AL, USA), was doped into the DOPC matrix. 1,2-dihexa-decanoyl-*sn*-glycero-3-phosphoethanolamine triethylammonium salt (TexasRed®-DHPE) was used as a fluorescent lipid. When mixed with DOPC, it accumulates in the L_α phase. Its excitation maximum is located at $582\,\mathrm{nm}$ and emission maximum at $601\,\mathrm{nm}$. TexasRed®-DHPE was purchased from Invitrogen (Karlsruhe, Germany). The chemical structures of commercially purchased alkylchain lipids are presented Section A.2. For better handling, the lipid concentrations were diluted to $1\,\mathrm{mg\,ml^{-1}}$ in a Chloroform:Freon® 113 ($1\,\mathrm{v\%}$:$1\,\mathrm{v\%}$) solution.

NeutrAvidin™, a $60\,\mathrm{kDa}$ deglycosylated avidin molecule was purchased from Invitrogen (Karlsruhe, Germany) both as unlabeled and Texas Red®-tagged conjugate. The apoptosis signaling ligand hsCD95L and its biotinylated conjugate CD95L-T4-btn were custom designed for this study by Apogenix GmbH (Heidelberg, Germany). Cell staining of fixed cells was done with DRAQ5$^{\mathrm{TM}}$from biostatus limited (Leicestershire, UK), a far-red fluorescent DNA dye with excitation maximum at $647\,\mathrm{nm}$ and emission maximum at $683\,\mathrm{nm}$. Actin was stained with Alexa Fluor® 488 phalloidin (ex: $499\,\mathrm{nm}$, em: $520\,\mathrm{nm}$) from Invitrogen (Karlsruhe, Germany).

2.3. Substrates

For fluorescence microscopy experiments, glass cover slips made from borosilicate glass (D 263M) were custom-ordered from Menzel GmbH (Braunschweig, Germany). The dimensions were $75\,\mathrm{mm} \times 25\,\mathrm{mm}$ with a thickness of $0.17\,\mathrm{mm} \pm 0.01\,\mathrm{mm}$. X-ray reflection experiments were performed on Si(100)–substrates (Si-Mat, Landsberg / Lech, Germany) with native oxide that were cut to $25\,\mathrm{mm} \times 25\,\mathrm{mm}$. Experiments for cell adhesion were done in $0.8\,\mathrm{mm}$ high μ-slide I luer channels, whereas time series experiments with subsequent fixation of cells were performed in μ-slide VI 0.4 channels. All flow chambers were purchased from Ibidi GmbH (Martinsried, Germany) without bottoms to allow custom preparation of substrates. Delo®-Photobond 4442 from *Delo* (Windach, Germany) was used as adhesive and cured under UV-light for at least $5\,\mathrm{h}$. The assembly of flow chambers under aqueous conditions was done with a low viscous Baysoline-Paste from Bayer (Leverkusen, Germany). The preparation of substrates is described in Subsection 2.5.2.

2.4. Substrate Cleaning Protocol

To remove any contaminants and produce hydrophilic surfaces, all substrates were cleaned according to a modified RCA Standard Clean 1 (Kern and Puotinen, 1970) protocol:

- successive ultrasonication for $5\,\mathrm{min}$ in acetone, ethanol, methanol and purified water
- incubation for $30\,\mathrm{min}$ at $60\,°\mathrm{C}$ in 1:1:5 (v/v/v) parts of $30\,\%$ ammonia : $30\,\%$ hydrogen peroxide : purified water
- intensive rinsing with purified water and storage overnight under vacuum conditions

Clean glass cover slides were made hydrophobic with n-octadecyltrimethoxysilane (ODTMS) from ABCR GmbH (Karlsruhe, Germany) with the following surface coating protocol:

- soaking slides into $160\,\mathrm{ml}$ toluene directly after vacuum conditions
- adding $8.4\,\mathrm{ml}$ ODTMS of $95\,\mathrm{m}\%$ and $0.8\,\mathrm{ml}$ butylamine of $99.5\,\mathrm{v}\%$ as catalyst
- sonication for $1\,\mathrm{h}$ under cooled conditions below the chain melting temperature $T_c = 18\,°\mathrm{C}$ of ODTMS
- incubation for $30\,\mathrm{min}$ on ice
- intensive rinsing with toluene and ethanol

All glass substrates were used within $14\,\mathrm{d}$ and were stored under vacuum conditions. Flow chamber lids were cleaned in $2\,\mathrm{v}\%$ Hellmanex® II solution from Hellma GmbH (Müllheim, Germany), washed with distilled water, and sonicated for $15\,\mathrm{min}$ in $70\,\mathrm{v}\%$ ethanol for disinfection. The assembly of flow chamber lids was carried out under sterile conditions inside a flow box. After assembly, all flow chambers were instantaneously used for cell experiments.

2.5. Film Balance Techniques

Within this thesis, monolayers of amphiphilic molecules were prepared at the air–water interface and transferred onto solid substrates. Several different Langmuir film balance setups were used. A Langmuir film balance typically consists of a Teflon® (polytetrafluoroethylen) trough filled with aqueous medium. A schematic view of a single barrier Langmuir film balance is shown in Figure 2.2a. Amphiphilic molecules that are spread onto the water surface will accumulate at the air–water interface and orient themselves with the hydrophobic part away from the aqueous subphase. The hydrophobic Teflon® prevents adsorption of the molecules onto the trough walls. The density and the surface pressure Π of the spread molecules are precisely controlled by either one or two barriers that regulate the available area A of the amphiphilic molecules. Depending on the density of the spread amphiphilic molecules, the two–dimensional surface pressure σ can be calculated from the Helmholtz free energy F (see Section 4.2) as,

$$\sigma = \left.\frac{\partial F}{\partial A}\right|_{T,N}. \tag{2.1}$$

The decrease in σ from the aqueous subphase (σ_0) is defined as lateral surface pressure Π,

$$\Pi = \sigma_0 - \sigma, \tag{2.2}$$

and is measured by the Wilhelmy plate technique (Gaines, 1966). Here, an hydrophilic platelet (e.g. filter paper) is immersed into the subphase and completely wetted. The forces acting on the platelet are the gravity, the buoyant force and the surface pressure pulling the Wilhelmy plate downwards. By measuring the resulting force on the Wilhelmy plate, knowing the geometry of the platelet, the surface pressure can be measured by $\sigma = \text{force/perimeter}$. Langmuir film balance techniques allow the deposition of multiple monolayers with alternating lipid orientations onto a solid substrate. The substrate is repeatedly immersed into or withdrawn from the subphase, while amphiphilic molecules transfer from the air–water interface onto the substrate. With increasing numbers of transfer repetitions, the substrate will be decorated with a single monolayer, a lipid membrane, or stacks of membranes. Depending on the monolayer composition of each transfer it is possible to create membranes with asymmetric leaflets.

Before monolayer preparation, the used Langmuir film balance was thoroughly cleaned. The trough was wiped with ethanol and subjected to multiple filling and aspiration cycles with purified water. The final water fill was equilibrated to $20\,°\mathrm{C}$ and the cleanness of the subphase was verified by closing the barriers to a minimum surface area. If this compression resulted in an increase of surface pressure above $0.2\,\mathrm{mN\,m^{-1}}$, the cleaning procedure was repeated. Otherwise, the surface was considered as clean and the surface pressure was set to $\Pi = 0\,\mathrm{mN\,m^{-1}}$. Afterwards the barriers were completely opened and spreading of the desired lipid solution was started.

2.5.1. Langmuir-Blodgett Transfer

Asymmetric membranes on solid supports were prepared with a proximal pure DOPC leaflet and a distal lipid layer consistent of fluorinated lipid domains within a DOPC matrix. The asymmetric deposition allows lateral healing of membrane defects and diffusion of fluorinated lipid domains within the upper leaflet. The lower

DOPC leaflet was transferred by the Langmuir-Blodgett (LB) technique on a self-built film balance equipped with a single barrier and a deep dipping-well for long cover slides. After cleaning (Section 2.4), a hydrophilic glass cover slide was attached to the dipper and immersed into the subphase. Subsequently, the lipid solution was spread onto the water surface and sufficient time ($> 20\,\mathrm{min}$) was allowed for solvent evaporation. Compression of the lipid monolayer was started with a constant rate of $13\,\mathrm{cm}^2/\,\mathrm{min}$ while the surface pressure was continuously monitored. At a preset value of $20\,\mathrm{mN\,m}^{-1}$ the barrier stopped and the surface pressure was kept constant during LB transfer. For monolayer transfer the substrate was withdrawn from the subphase with a slow dipping speed of $7\,\mathrm{mm}/\,\mathrm{min}$ and instantaneously used for Langmuir-Schäfer transfer to avoid dryingout. To assess the quality of the transferred film, the area of the immersed substrate was compared to the diminished area of the trough during LB transfer. An area reduction occurs during LB transfer, since the surface pressure is kept constant by the barrier. Only substrates with a transfer ratio close to unity were used for experiments.

2.5.2. Langmuir-Schäfer Transfer

Langmuir-Schäfer (LS) transfer uses hydrophobic substrates, either prepared by LB deposition or by silanization (Section 2.4). The monolayer preparation and transfer was done on a Nima 311D (Coventry, UK) filmbalance. Before calibrations, a polished Teflon®lid ($65\,\mathrm{cm} \times 95\,\mathrm{cm}$) was placed on the trough bottom. The lid was immersed completely into the water subphase and later used to remove the sample. After temperature equilibration to $20\,°\mathrm{C}$ the lipid monolayer was spread onto the water surface and more than $50\,\mathrm{min}$ solvent evaporation time were allowed for chloroform/Freon®dissolved lipid solutions. The monolayer was slowly compressed ($2\,\mathrm{cm}^2/\,\mathrm{min}$) to the desired surface pressure in order to remain close to the thermodynamic equilibrium of domains during compression. After an additional $15\,\mathrm{min}$ equilibration at a constant surface pressure, the substrate was held slightly oblique above the water level with the hydrophobic surface facing downwards. LS transfer was completed by gently dropping the substrate onto the water surface and immersing it subsequently into the water subphase. The sample was placed onto the immersed Teflon®lid. A remaining water interlayer between solid supported membrane and the Teflon®lid prevents the membrane from disruption. This was confirmed with bleaching tests of fluorescence tracer labeled membranes (Section 3.5). Finally, a suited Teflon®frame was clamped onto the lid and the sample was transferred under immersed conditions into an external water bath. There, flow chamber lids were mounted under water onto the substrates to prevent drying of the membrane. The water filled channel volume was exchanged with cell culture medium and chambers were ready for use. A schematic overview of the LS transfer steps is shown in Figure 2.2.

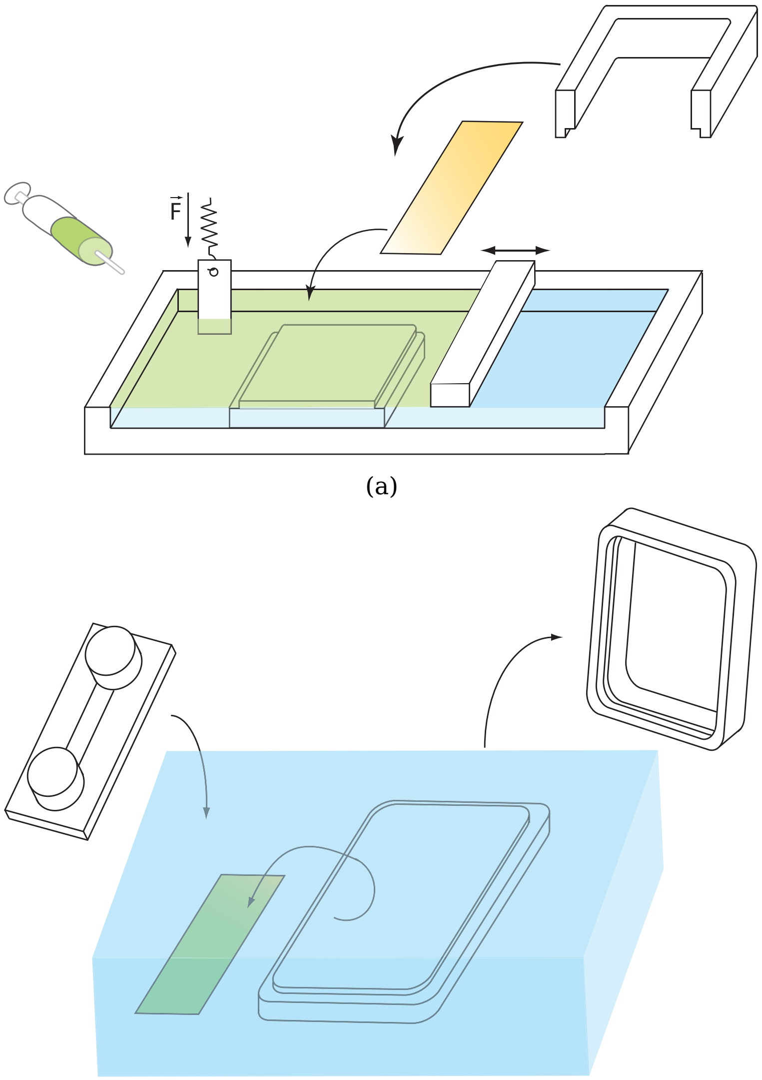

Figure 2.2.: (a) Schematic cross section through a single barrier film balance used for Langmuir Schäfer transfer. (b) Schematic illustration of flow chambers assembly in a water bath for solid supported membranes.

Table 2.1.: Filter sets used for fluorescence microscopy. The wavelength for excitation and emission filters denote the center wavelength and the width of the bandpass.

Fluorescent marker	Excitation [nm]	Dichroic mirror [nm]	Emission [nm]	Producer
Texas Red®	560/40	585	630/75	Carl Zeiss
TRITC	525/45	560	595/60	Omega Optical
DRAQ5	640/30	660	695/50	Carl Zeiss

2.5.3. Film Balance with Kelvin Probe

Surface potential measurements at the air–water interface were performed on a two barrier, metal coated film balance µSpot mini trough from Kibron Inc. (Espoo, Finland). The trough is equipped with a macroscopic vibrating Kelvin probe gold electrode that was placed in central position between the two closed barriers. Before monolayer spreading, the trough was intensively rinsed under a continuous flow of distilled water from the tap and thoroughly wiped with ethanol. A subphase of $25\,\mathrm{ml}$ distilled water was spread on the trough and a test compression with pure water subphase was performed. Only if the surface potential had been constant ($\pm 10\,\mathrm{mV}$), was the interface considered clean and the measured surface potential was set to $0\,\mathrm{V}$. Otherwise the cleaning procedure was repeated. The surface pressure was set to $\Pi = 0\,\mathrm{mN\,m^{-1}}$ at an open barrier position. The lipid solutions were spread in very small drops only close to the barriers, to avoid ripening of the water subphase due to solvent displacement.

2.6. Fluorescence Microscopy

Fluorescence microscopy was used to quantify the size distribution of fluorinated lipid domains and to reconstruct the three-dimensional shape of stained cells. For monolayers, a Zeiss Axiovert 200 microscope (Göttingen, Germany) equipped with a X-cite® 120Q PC mercury lamp (EXOF, Mississauga, ON-Canada) illumination system and suitable filter sets (Table 2.1) were used. Table 2.2 lists all objectives used in this study together with their magnification and numerical aperture. Images were recorded with an Orca ER CCD-camera (Hamamatsu Photonics, Herrsching, Germany) at exposure times below $10\,\mathrm{ms}$. The acquisition software Hokawo version 2.1 (Hamamatsu Photonics, Herrsching, Germany) allowed for time laps imaging and video capturing to be transferred via a frame grabber card from Coreco Imaging (Gröbenzell, Germany).

Image stacks for three-dimensional cell reconstruction were recorded with a con-

Table 2.2.: Objectives used in this thesis. N.A. denotes the numerical aperture of the objective and phase ring the standardized size of the implemented phase contrast ring.

Magnification	Medium	N.A.	Correction	Phase Ring	Producer
20x LD	air	0.40	Achroplan	Ph1	Carl Zeiss
20x ELWD	air	0.45	Plan Fluor	Ph1	Nikon
40x ELWD	air	0.60	Plan Fluor	Ph2	Nikon
60x	air	0.95	Plan Apo	Ph2	Nikon
60x	water	1.20	Plan Apo VC	Ph2	Nikon
63x LD	air	0.75	Achroplan	Ph2	Carl Zeiss
63x Antiflex	oil	1.25	PlanNeofluar	Ph2	Carl Zeiss
100x	water	1.00	Achroplan	—	Carl Zeiss

focal microscope setup at the Nikon Imaging Center (BIOQUANT, Heidelberg, Germany). A Perkin Elmer (Waltham, MA-USA) confocal UltraView spinning disc unit was mounted on an inverted Nikon Eclipse TI microscope (Nikon, Düsseldorf, Germany) equipped with a 60x Plan Apo VC water immersion objective (N.A. 1.2). Image acquisition was performed with Volocity 5.2 software (Perkin Elmer, Waltham, MA-USA) and a Hamamatsu EM-CCD camera (Herrsching, Germany) with matched exposure times below $400\,\mathrm{ms}$. The image stacks were deconvolved with Huygens software 3.4 from Scientific Volume Imaging (Hilversum, The Netherlands). Visualization and further image processing were performed with ImageJ 1.44 (Abramoff et al., 2004) and Volume Viewer V1.05 plugin. Calculation of the cell volume was performed with the Volumest plugin (Markko, 2008).

2.7. Reflection Interference Contrast Microscopy

Images for reflection interference contrast microscopy (RICM) were recorded with the same Axiovert 200 inverted microscope and camera setup as described for fluorescence microscopy. The monochromatic wavelength of ($546\,\mathrm{nm} \pm 12\,\mathrm{nm}$) was extracted with an appropriate green band pass filter from the EXOF X–cite® 120Q PC metal halogenide lamp (Mississauga, ON-Canada) that was connected with a liquid fiber to the microscope. To reduce background signal and provide enhanced contrast of interference fringes, a 63x Antiflex Plan-Neofluar oil objective with numerical aperture of 1.25 and built–in lambda quarter plate (Carl Zeiss, Göttingen, Germany) was used. A polarizer was inserted in the illumination pathway and unretarded light that passes twice through the lambda quarter plate was filtered at a crossed Sénarmont analyzer. The numerical aperture of illumination was set approximately to 0.5. Image sequences of cells consisted of 12 frames per second with

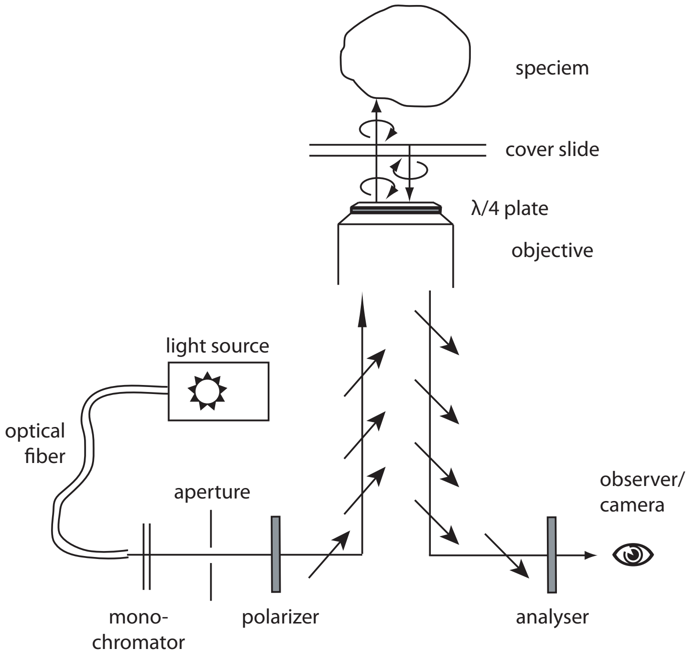

Figure 2.3.: (a) Schematic alignment of optical components for RICM setup with antiflex contrast enhancement.

an individual exposure time of $75\,\mathrm{ms}$. A sketch of the instrumental RICM setup with antiflex contrast enhancement is shown in Figure 2.3.

2.8. Synchrotron X-ray Measurements

Specular X-ray reflectivity and grazing incidence X-ray diffraction measurements were performed at the beamline ID10B of the European Synchrotron Radiation Facility (ESRF) in Grenoble, France. The energy of the incoming beam was set with a diamond [111] double crystal setup to $8.00\,\mathrm{keV}$ ($\lambda = 1.55\,\text{Å}$). For grazing–incidence X-ray diffraction (Figure 2.4a), a collimating slit for the incoming beam was set in horizontal direction to $0.2\,\mathrm{mm}$ and in vertical direction to $0.05\,\mathrm{mm}$. The sample stage was equipped with a film balance that guaranteed a horizontal air–water interface and allowed height displacements to position the impinging beam on the water surface. The linear detector was modified with an analyzer crystal setup (Section 5.1) and mounted on a 3 circle diffractometer arm which allowed out–of–plane detection up to $\sim 40°$. Calibration of the analyzer crystal yielded Bragg condition for the diffracted beam under $\tau_B = 14.35°$ for the used X-ray wavelength ($\lambda = 1.55\,\text{Å}$).

Θ–2Θ X-ray reflection measurements (Figure 2.4b) were performed on solid substrates. Collimating slits for the incoming beam were set to $0.5\,\mathrm{mm}$ in horizontal, and

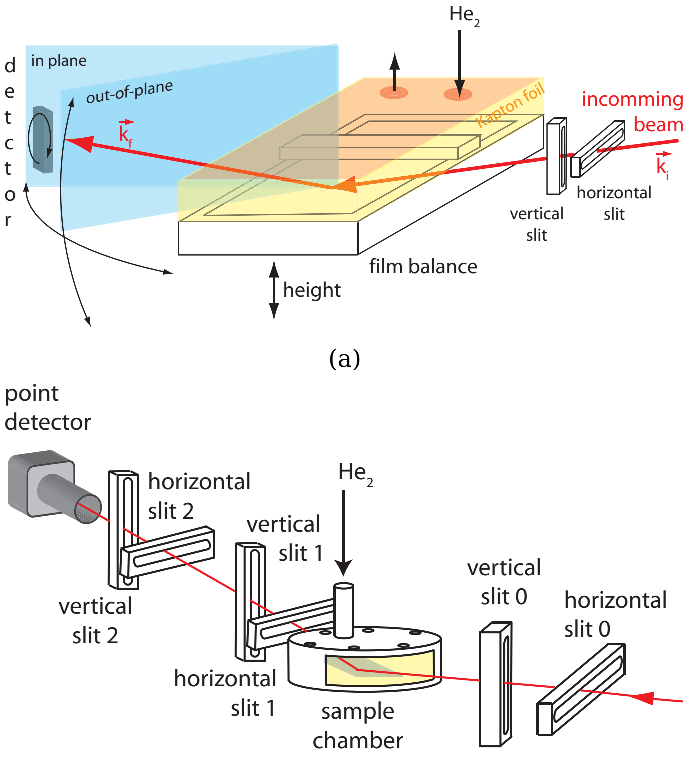

(a)

(b)

Figure 2.4.: (a) Grazing incidence X-ray diffraction setup for the air-water interface and (b) specular X-ray reflectivity measurement setup for an air-solid interfaces at the beamline ID10B of the ESRF.

$0.05\,\mathrm{mm}$ in vertical direction. The sample was placed on a 3 circle diffractometer, which allowed sample alignment in all directions. In front of a fixed point detector, two resolution confining slits with horizontal openings of $0.6\,\mathrm{mm}$ and $0.3\,\mathrm{mm}$ were placed in series.

For both setups, the samples were enclosed in a gas-tight sample chamber with embedded Kapton®foil windows, to allow transmittance of the incoming and outgoing beam. The sample chambers were purged with He_2 and oxygen concentration was reduced to a level of below $0.1\,\%$ to minimize radiation damage.

2.9. Macrophages

The murine macrophages cell line J774.A1 was purchased from the Deutsche Sammlung von Mikroorganismen und Zellkulturen GmbH (DSMZ GmbH, Braunschweig, Germany). Cell culture was maintained under standard conditions ($37\,°\mathrm{C}$ and $5\,\%$ CO_2) in $89\,\mathrm{v\%}$ Dulbecco's Modified Eagle's Medium (DMEM) with high ($4500\,\mathrm{mg\,l^{-1}}$) glucose content, $10\,\mathrm{v\%}$ fetal bovine serum (FBS), and $1\,\mathrm{v\%}$ penicillin and streptomycin (Sigma–Aldrich Chemie GmbH, Munich, Germany). Macrophages were harvested and split at densities of $\sim 8 \times 10^5\,\mathrm{cells\,cm^{-2}}$ and seeded for $\sim 2 \times 10^5\,\mathrm{cells\,cm^{-2}}$. For experiments, cells were diluted to concentrations of $\sim 2 \times 10^5\,\mathrm{cells\,ml^{-1}}$. At least $16\,\mathrm{h}$ before harvesting macrophages with a scraper, the cell culture medium was exchanged to a FBS, phenol red, and glucose–free DMEM medium to synchronize cells. Cell adhesion experiments were carried out in $140\,\mathrm{mM}$ NaCl and $1\,\mathrm{mM}$ CaCl aqueous solution buffered with tris(hydroxymethyl)aminomethane (TRIS) at $7.4\,\mathrm{pH}$.

2.10. Pancreatic Cancer Cells

Cancer cells were isolated from a male patient suffering an invasive malignant pancreas tumor. In the following they are referred as PanD24 or pancreatic cancer cells. PanD24 cells were cultured in freshly prepared and sterile filtered medium composed of:

- $250\,\mathrm{ml}$ DMEM : $250\,\mathrm{ml}$ Ham's Nutritient Mixture F12 with L-glutamine
- $1\,\mathrm{v\%}$ penicillin and streptomyicin
- $250\,\mathrm{ml}$ N2 supplements
- $10\,\mathrm{ml}$ B–27 supplements
- $20\,\mathrm{\mu l}$ bFGF
- $20\,\mathrm{\mu l}$ EGF

Supplements and growth factors (bFGF, EGF) were received in ready-made concentrations from the Deutsches Krebsforschungszentrum (DKFZ, Heidelberg, Germany) and medium was purchased from (Sigma–Aldrich Chemie GmbH, Munich, Germany). PanD24 grew in solution under standard conditions (37 °C, 5 % CO_2) and became not adherent. Cells were split by a factor of $\sim 1:8$ as soon as cell agglomerates were well visible to the eye. Prior to experiments, cells were twice washed with 150 mM phosphate buffered saline (PBS) at 7.4 pH and centrifuged down at 1200 rps for 5 min. Experiments were carried out in a freshly prepared culture medium without phenol red, penicillin and streptomycin at concentrations of $\sim 2 \times 10^5\,\mathrm{cells\,ml^{-1}}$.

2.11. Vesicle Preparation

For preparation of small unilamellar vesicles (SUV), lipid suspensions with a total lipid content of 1 mg were dried in RCA cleaned flasks with a rotary evaporator. For a complete removal of the solvent, lipids were stored overnight in vacuum. The dried lipids were resuspended in 1 ml aqueous buffer and incubated for 2 h at 37°, where they formed multilamellar vesicles with broad size distribution. Subsequent sonication for 30 min with a titanium tip sonicator formed SUVs. The vesicle solution was centrifuged to remove remaining titanium particles and was stored for experiments no longer than 3 d at 4°.

Giant unilamellar vesicles (GUV) were prepared by electroformation. Lipid solutions with a total lipid content of 1 mg were dried on two indium tin oxide (ITO) coated glass plates. Both glass plates were fixed inside a Teflon®holder with ITO sides facing to each other and an inter-electrode spacing of $\sim 2\,\mathrm{mm}$. After filling the spacing with distilled water, a weak AC field of 10 Hz and 0.5 V is applied on the ITO electrodes. Every 20 min the electric field is gradually increased by 0.5 V to a final potential of 2 V. The final lipid solution is a mixture of unilamellar and multilamellar giant vesicles and was immediately used for experiments.

2.12. Ligand Deposition

The deposition of CD95L-T4-btn on btnFL17-domains and DOPE-btn lipid membranes was realized by a NeutrAvidin™-biotin bridge with the following preparation steps:

- incubation of supported membrane with $1\,\mathrm{\mu g\,ml^{-1}}$ NeutrAvidin™for 15 min
- intensive rinsing with purified water (50 ml)
- incubation with CD95-T4-btn 20 nM for 40 min
- intensive rinsing with PBS (50 ml)
- exchange to cell culture medium and prewarming to 37 °C
- addition of (60 µl) cell suspension at a final concentration of $2 \times 10^6\,\mathrm{cells\,ml^{-1}}$
- if required, addition of fluoresence marker molecules

3. Preparation Techniques of Domains

The usage of highly fluoric and at the same time lipophobic molecules leads to difficulties regarding the solubility and handling of lipids. This chapter deals with adapted preparation techniques for fluorolipid containing monolayer deposition on solid supports. Protocols were systematically tested and optimized to prepare homogeneously distributed, large scale (several cm^2) domain patterns on solid supports that allowed for subsequent cell experiments under comparable conditions.

3.1. Solvent Tuning for Fluorous/Organic Systems

In standard organic solvents the solubility of heavily fluoric molecules turned out to be very low. An attempt to increase the solvating power was done with regards on polarity and fluorophility of the solvents (Chu et al., 2007; Yu et al., 2005). The tuning strategy had to account for simultaneous handling of amphiphatic hydrocarbon based lipids and lipophobic fluorocarbon lipids. Requirements of the choice of possible fluorous solvents were miscibility to chloroform – where hydrocarbon lipids were dissolved – and a low boiling point near room temperature, to allow for evaporation at the air–water interface prior to LS deposition (Subsection 2.5.2). Dissolving of fluorinated lipids was tested in a series of solvent mixtures, starting with fluorophilic, but low polar perfluoroalkanes, and increasing the polarity with the addition of hydrofluoroethers or more polar chlorinated ethanes and methanes. Table 3.1 lists the set of different solvent mixtures, where $1\,\mathrm{mg}$ FL17 molecules (powder), having highest fluorocarbon–content within this study, were dissolved in up to $5\,\mathrm{ml}$ solvent mixture. The lipid concentration decreased by addition of $500\,\mathrm{\mu l}$ solvent from $1\,\mathrm{mg\,ml^{-1}}$ to a final concentration of $0.2\,\mathrm{mg\,ml^{-1}}$. After each dilution step, the mixtures were subjected to a heating and cooling cycle between $40\,°\mathrm{C}$ and $0\,°\mathrm{C}$ in a closed test–tube, followed by subsequent sonication for $15\,\mathrm{min}$.

As shown in Table 3.1, no solvation of FL17 was observed in pure perfluoroheaxan and chloroform. In mixtures that indicated *low* solubility, a small fraction of crystallites remained in solution. These crystallites were hardly detectable to the eye and could not be disrupted by longer sonication cycles. Spreading efficiency of these solvent mixtures on Langmuir monolayers confirmed poor dissolution of FL17. Acceptable solvation of molecules was only reached for tri-chloro-tri-fluoroethane (commercial name: Freon® 113) : chloroform mixtures at concentrations below $0.4\,\mathrm{mg\,ml^{-1}}$, and methylperfluorbutan : chloroform mixtures less concentrated than

Table 3.1.: Solubility of fluorinated molecules in low polar, fluorous solvent mixtures. The polarity of the solvent was stepwise increased by varying the solvent composition.

mixture	ratio	solubility
perfluorohexan	1	no
perfluorohexan : methylperfluorobutan	1:1	low
perfluorohexan : methylperfluorobutan : chloroform	1:1:1	low
perfluorohexan : Freon® 113 : chloroform	2:1:1	low
methylperflurobutan : chloroform	1:1	medium
Freon® 113 : chloroform	1:1	medium
chloroform	1	no

$0.6\,\mathrm{mg\,ml^{-1}}$. The latter one was excluded after monolayer compression experiments (see Section 3.2). Flourinated molecules carrying additional organic modifications at the head group (FL10Man, btnFL17) were dissolved in Freon® 113 : chloroform mixtures with addition of a small droplet of ethanol.

3.2. Spreading Efficiency

The low solubility of fluorinated lipids caused small concentration fluctuations between independently prepared lipid solutions. These lipid solutions were the basis of binary lipid mixtures of DOPC and fluorinated lipids with varying molar content. In order to reduce the systematic error in molar concentration of binary mixtures, each fluorinated lipid stock solution was adjusted for its theoretical expected value. From grazing–incidence X-ray diffraction experiments presented in Section 5.1, the molecular area for each fluorinated lipid molecule is known. For a lateral surface pressure of $\Pi = 20\,\mathrm{mN\,m^{-1}}$ a molecular area of $56.4\,\text{Å}^2$ for FL10, $56.3\,\text{Å}^2$ for FL13, and $55.0\,\text{Å}^2$ for FL17 molecules was obtained. Spreading lipid solutions with molecular concentration lower than expected onto the air–water surface leads to an underestimation of the molecular area in the compression isotherm. This error was corrected for each fluorinated lipid stock solution by recording the respective isotherms. Special care was taken during lipid spreading at the air–water interface to minimize loss of lipids to the subphase. Figure 3.1a and Figure 3.1b show the area of corrected isotherms for all fluorinated lipids used in this study. The correction factor for each stock solution was calculated from the relative mismatch of molecular areas at a surface pressure Π of $25\,\mathrm{mN\,m^{-1}}$.

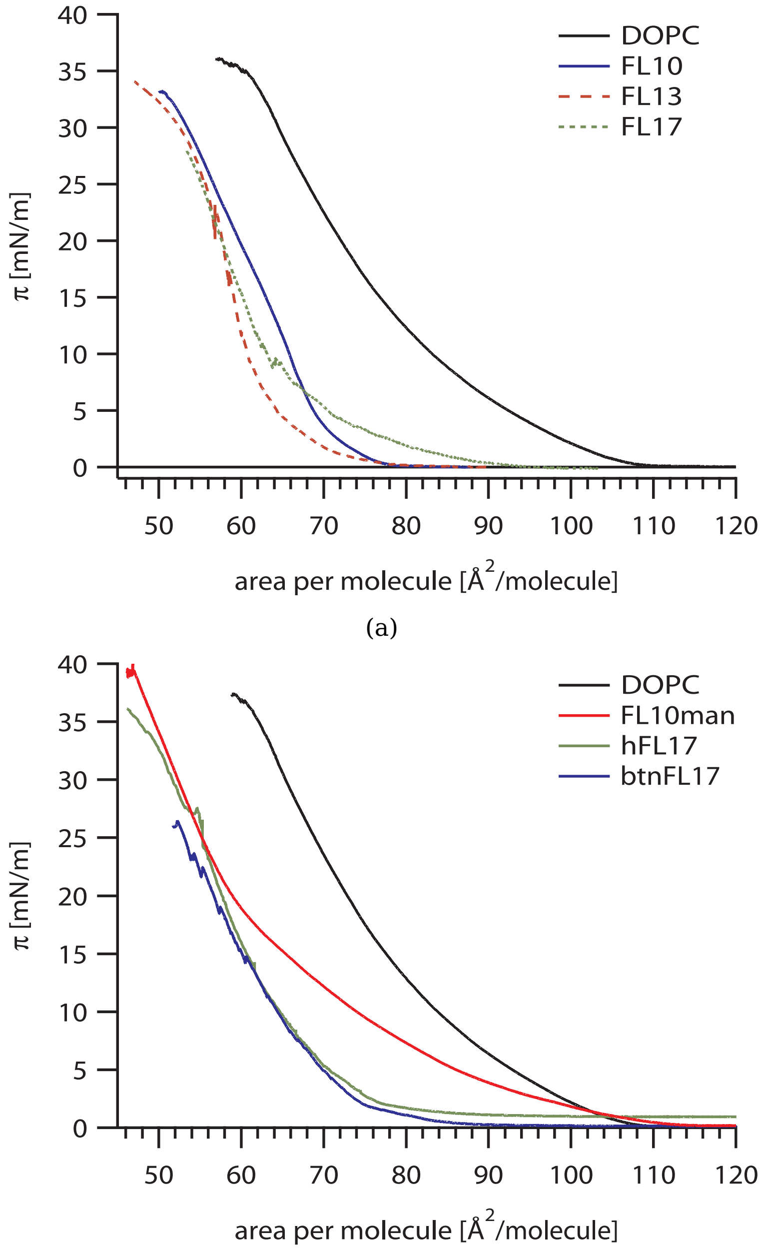

(a)

(b)

Figure 3.1.: *Top:* Langmuir isotherms of DOPC, FL10, FL13, and FL17 after spreading area correction. *Bottom:* Compression isotherms of FL10Man, btnFL17, and acFL17.

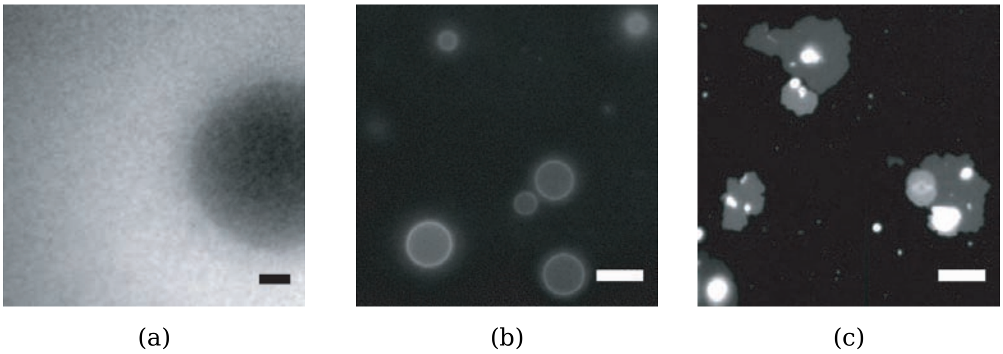
(a) (b) (c)

Figure 3.2.: (Vesicles were prepared from $33\,\mathrm{mol\%}$ fluorinated lipid mixtures. (a) Fluorescence micrography of supported membrane after vesicle fusion with SUVs. Bleaching spot demonstrates the successful deposition of a membrane. (b) GUVs in water hovering above the substrate and (c) forming inhomogeneous membrane patches after rupturing in aqueous buffer solution. No domain formation was observed. Scale bars are $10\,\mathrm{\mu m}$.

3.3. Vesicle Fusion

A widely used and fast approach for preparation of high quality supported lipid bilayers is the vesicle fusion technique (Reviakine and Brisson, 2000). It originates from cell experiments of immune cells with supported model membranes (Watts et al., 1986; McConnell et al., 1986). For vesicle fusion, the composition of lipid vesicles is one important factor for successful deposition of membranes onto the solid substrates (Nollert et al., 1995). Lipid mixtures consisting of $33\,\mathrm{mol\%}$ FL10, $66.9\,\mathrm{mol\%}$ DOPC, and $0.1\,\mathrm{mol\%}$ TexasRed®-DHPE were tested for a potential application of the vesicle fusion technique to simplify and fasten domain formation on solid supports.

Small unilamellar vesicles (SUV) with diameters below $100\,\mathrm{nm}$ were prepared as described in Section 2.11. For membrane deposition, flow chambers with silanized and hydrophilic glass slides were filled with $200\,\mathrm{\mu l}$ SUV solution. The samples were incubated for $30\,\mathrm{min}$ at $37\,°\mathrm{C}$ and afterwards vigorously rinsed with buffer. Figure 3.2a shows a fluorescence micrography after vesicle fusion. All substrates displayed homogeneous membranes without domains of phase separated fluorinated lipids. The dark spot was generated through bleaching of the membrane for $30\,\mathrm{sec}$ with a closed field blend. A healing of the bleaching spot was observed through lateral diffusion of the fluorescent lipids, which demonstrates the good quality of the membrane. The lack of FL10 domains (compare Figure 5.6) indicates a separation of fluorinated molecules from the DOPC already before vesicle fusion, i.e., during SUV preparation. An electrostatic repulsion of fluorinated lipids from the substrate due to high dipole contributions was excluded by usage of $150\,\mathrm{mM}$

monovalent PBS buffer. The high salt concentration reduces the Debye screening length below $8\,\text{Å}$ (Israelachvili, 1991, p. 238) and allows SUVs to approach the surface and to rupture (Kalb et al., 1992; Reviakine and Brisson, 2000).

To reduce stress on fluorinated lipids that are incorporated in membranes of high curvature, vesicle fusion was also performed with giant unilamellar vesicles (GUV) with diameters much larger than $1\,\mu\mathrm{m}$. Preparation of GUVs was performed by electro-swelling and is described in Section 2.11. Figure 3.2b shows fluorescence pictures of GUVs in water and Figure 3.2c after addition of $150\,\mathrm{mM}$ PBS buffer. GUVs displayed a homogeneous fluorescence without phase separated FL10 domains. After addition of $150\,\mathrm{mM}$ monovalent buffer, vesicles became adherent and ruptured onto the substrate. The formed membrane patches showed inhomogeneous superposition of membranes with incomplete surface coating, but did not reveal phase-excluding domains of fluorescent lipids.

Since no phase separated FL10 domains were observed, vesicle fusion was excluded as possible preparation technique for fluorinated lipid mixtures.

3.4. Solvent Exchange

A different approach to form membranes on solid supports is the so-called solvent exchange method. Dissolved lipids are injected into a closed sample chamber and the relative water content of the solvent is increased. The low solubility of lipid molecules in water (below $1 \times 10^{-12}\,\mathrm{mol\,l^{-1}}$) (Sackmann and Merkel, 2010, p. 301) forces the lipid molecules to aggregate within the aqueous phase or to assemble on top of the chamber walls. For $33\,\mathrm{mol\%} : 66.9\,\mathrm{mol\%} : 0.1\,\mathrm{mol\%}$ FL10 : DOPC : TexasRed®-DHPE lipid mixtures, $50\,\mathrm{v\%}$ methanol to the $1\,\mathrm{v\%}$:$1\,\mathrm{v\%}$ Chloroform:Freon® 113 stock solution was added, since Freon® 113 and chloroform can be regarded as immiscible with water. The sample chamber was filled with $200\,\mu\mathrm{l}$ of solution and the solvents were slowly exchange by a methanol:water mixture with increasing water content. Figure 3.3a shows vesicles that emerged in the aqueous phase during a slow solvent exchange process. Differences in fluorescence intensities indicate an inhomogeneous demixing of fluorinated lipids from the DOPC matrix. After a complete solvent exchange process, the formation of monolayers and membranes on the sample chamber walls was observed. Figure 3.3b shows a selected area of a fluorescence image where fluorinated lipids (dark spots) are surrounded by a DOPC:TexasRed®-DHPE matrix (bright area). Domains are randomly distributed and are larger in size compared to other transfer techniques (see Figure 5.6). The missing control on film properties, like the lateral surface pressure Π, led to an uncontrolled formation of monolayers, membranes and stacked structures. Figure 3.3c shows a fluorescence image of an area without surface coating (black region, right), with monolayer formation (gray region with black domains, center), and with multilayer deposition (bright region with bright spots, left). The

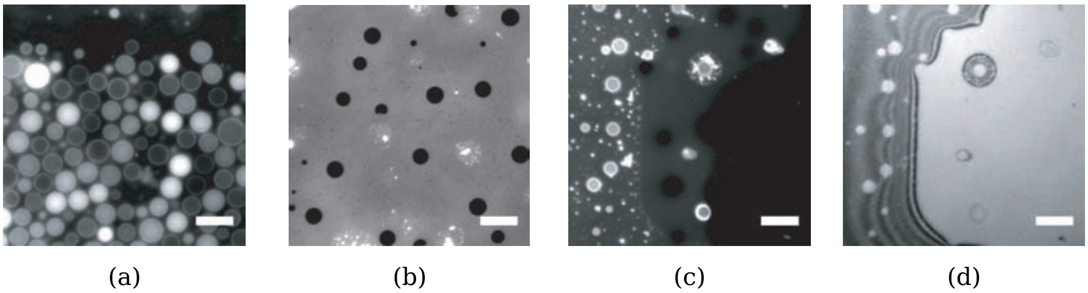
(a) (b) (c) (d)

Figure 3.3.: (a) Vesicles from FL10:DOPC mixtures emerging in aqueous phase during solvent exchange. (b) Fluorescence microscopy images of supported membranes after solvent exchange displaying randomly distributed FL10 domains (dark). (c) Stacked membrane patches that cause (d) interference fringes with RICM. All scale bars are $10\,\mu\mathrm{m}$.

interference patterns of the RICM image on the same scene, Figure 3.3d, confirm stacked structures by alternating fringes. Since it was not possible to precisely control monolayer properties and reproduce the lateral distribution of fluorinated domains, solvent exchange emerged as unfeasible method for membrane deposition of fluorinated lipid mixtures.

3.5. Asymmetric Membrane Deposition

Since membrane preparation by self-assembly methods resulted in dissatisfying membrane qualities for fluorinated binary lipid mixtures, the transfer characteristics of domains from Langmuir films onto solid substrates were quantified. Albeit preparation is far more laborious, the Langmuir preparation methods benefit from a defined molecular monolayer composition, allowing preparation of asymmetric leaflets, and a precise control of the lateral density of lipids.

Monolayers composed of $33\,\mathrm{mol\%}$ hFL17 : $67\,\mathrm{mol\%}$ DOPC enriched with traces of TexasRed®-DHPE were transferred by LS (Subsection 2.5.2) deposition onto silanized glass substrates. Figure 3.4a shows hFL17 domains surrounded by a fluorescent labeled DOPC matrix. The fluorescence tracer lipid preferentially enriches in the liquid disordered phase of DOPC molecules and reveals black spots where olephobic fluorinated lipids are present. The same results were found for monolayers transferred onto glass slides coated beforehand with an underlying, pure DOPC monolayer (Figure 3.4b). The proximal LB transferred (Subsection 2.5.1) DOPC monolayer was instantaneous completed by LS transfer to an asymmetric membrane with incorporated fluorinated lipid domains. In contrast, membranes that were prepared for symmetric $33\,\mathrm{mol\%}$ hFL17 : $66.9\,\mathrm{mol\%}$ DOPC and $0.1\,\mathrm{mol\%}$ TexasRed®-DHPE leaflets by LB transfer revealed irregular distributions of the fluorescence tracer

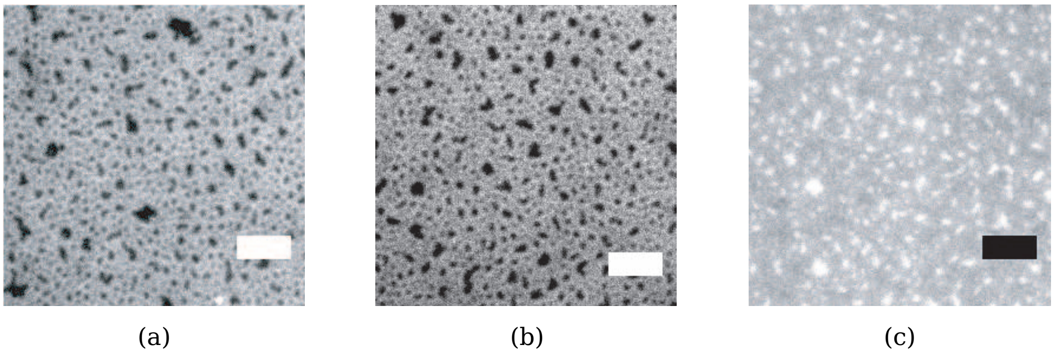
(a) (b) (c)

Figure 3.4.: Preparation of solid supported hFL17:DOPC membrane leaflets by Langmuir filmbalance techniques on (a) silanized, (b) DOPC monolayer coated, and (c) symmetric hFL17:DOPC leaflets. All scale bars correspond to 5 µm.

lipid TexasRed®-DHPE. The domains appeared inverted in luminescence. Since a clear phase separation and full functionality of fluorinated lipids were not guaranteed for symmetric membranes, all further experiments in this study were performed on solid supported substrates with asymmetric membranes.

4. Theory of Domain Formation

This chapter presents a theoretical description of domain formation in Langmuir monolayers under equilibrium conditions. The equivalent dipole model explains the competing effect of the line tension and electrostatic forces that are responsible for phase separation and pattern formation in two-dimensional liquids. A discussion on important structural parameters of mesoscopic patterns, such as equilibrium radius of domains and inter-domain correlation, is followed by a review on domain equilibration processes and phase transition characteristics. The structural parameters derived in this chapter provide a reference for fluorinated lipid domains that are discussed in Chapter 5.

4.1. Thermodynamic Description of Liquids

Liquids are distinguished from highly confined solids by the lack of long-range order, which provides each liquid particle with a higher degree of translational and rotational freedom. A general, applicable model of liquids that takes all the varying geometrical factors into account is difficult to describe. The nature of liquids is dominated by the importance of collision processes and short range correlations between the liquid constituents. Therefore, the structure of liquids is dominated by core repulsion of these kinetic constituents, associated with the so-called excluded-volume effect (Hansen and McDonald, 2008, p.3). Interaction energies together with two-molecular correlation functions determine the total energy stored in a system which minimizes by law of nature. To calculate the total free energy of a system, all pair-wise interaction energies of particles are summed up as functions of the molecular separation, orientation, and entropy. If the system additionally includes competing long-range interactions, like dipole or electrostatic forces, then variations in the correlation functions can appear and lead to modulated phases (Seul and Andelman, 1995). These variations appear as periodic spatial patterns, like separated domains or stripe-like phases. They were found for a vast variety of systems, like e.g. colloidal suspensions (Belloni, 2000), superconducting and ferrofluidic systems (Cape and Lehman, 1971), or more biologically relevant Langmuir films (Weis and McConnell, 1984; Möhwald, 1990). This thesis focuses solely on such two-dimensional Langmuir films (Langmuir, 1917) of amphiphilic molecules enriched at the air–water interface. Langmuir monolayers differ from ideal two-dimensional, incompressible liquids by the asymmetric coupling to the surrounding media, air and water. Thus, long ranging dipole- or electrostatic interactions lead to asymmetric, non extensive energy distributions at the interface that induce modulated phases of finite size (Wurlitzer, 2001, p.4).

4.2. Total Free Energy

The total amount of energy stored in a system can be expressed by a set of intensive and extensive state variables, such as pressure p, volume V, chemical potential μ^{ch}, number of particles N, charge q of a particle, or electric potential Φ, that fully describe the experimental system. Typically, by changing one of these variables, mechanical, chemical or electrostatic work W can be applied to or gained from the system. The first law of thermodynamics states that the change of internal energy dU of a system is altered by the work δW and heat δQ applied to the system:

$$dU = \delta Q + \delta W. \tag{4.1}$$

The amount of energy received in forms of heat δQ is expressed by the change in entropy dS at temperature T. In thermodynamics, these state variables are related by a set of state equations that can be transformed into each other by Legendre transformations. Dependent on the set of fixed state variables, they yield different thermodynamic potentials. In this thesis, I describe a liquid phase of closed volume V in equilibrium with its surrounding, i.e., at constant temperature T and with given particle number N. The total energy stored in this system is called Helmholtz free energy F (Ibach, 2006, p.159)

$$dF = dU - SdT = -SdT - pdV + \mu^{ch}dN + \Phi dq... . \tag{4.2}$$

Equation 4.2 reflects a full description of a single homogeneous liquid phase. As soon as a system consists of a second phase, necessarily some boundary line or interface area between the phases must exist. The creation of such an interface introduces inhomogeneities, such as deviations in particle density or chemical potential, and costs energy. In three dimensions the energy stored within this interface of area A is associated with the specific surface free energy:

$$f^s = \frac{F^s}{A}. \tag{4.3}$$

The surface free energy of an existing, stable interface must be positive (in absence of strong inter-particle bonds, like covalent bonds). Otherwise the condensed phase would prefer to dissociate. In different fields of solid state physics f^s is definied for different fixed state variables (Ibach, 2006, p.161) and is then called surface tension. In the following I will refer to an idealized, two-dimensional, infinitely narrow interface, i.e., bulk properties like chemical potential or the electric potential close to the surface are not influenced. This surface free energy is then defined along a contour line l, sensing an attractive line tension λ:

$$l\lambda = F^s - \sum \mu_i^{ch} N_i - \Phi q = F_\lambda \ , \tag{4.4}$$

$$\lambda = \left.\frac{\partial F^s}{\partial p}\right|_{T,l} . \tag{4.5}$$

It is necessary to note, that the line tension in Equation 4.5 is defined for constant temperature T and vanishing dipole interactions. It is not a material constant, but rather depends on the shape and curvature of the contour line.
Several theories (McConnell, 1991; Seul and Andelman, 1995; Iwamoto and Ou-Yang, 2004) explain the existence of modulated phases under equilibrium conditions by the so-called equivalent dipole model. This means, the total free energy F of a two component system is described as the competing effect of line tension and long range electrostatic repulsion. Thus, all energy contributions can be categorized within three major terms. The first is a background free energy F_0 that takes all entropy contributions regarding the molar composition and total accessible area into consideration. In this thesis, F_0 can be seen as constant, since molar fraction and molecular area of lipids were not changed during the experiments. Additionally, the surface free energy caused by the separation of modulated phases is accounted as-second term by the line energy term F_λ. And as third term, electrostatic long range energy contributions that arise from dipole interactions or charged molecules are considered as F_{el}. Since the electrostatic contributions from one phase can be included within the background energy F_0, only the potential difference with respect to the second phases needs to be considered and scales proportional to the domain sizes. Contributions originating from domain shapes and entropic terms from arrangements of domain patterns are not covered within this theoretical framework. In summary, the total free energy F of a system with modulated phases writes as:

$$F = F_0 + F_\lambda + F_{el} \ . \tag{4.6}$$

4.3. Interaction Potentials

Lipid monolayers at the air-water interface minimize their total free energy F and can thereby separate into discrete phases with sharp boundaries (Gibbs phases), where one homogeneous phase is surrounded by a second coexisting phase. As mentioned in Section 4.2, the existence of such separated phases under equilibrium conditions can be explained as the competing effect of line tension and long-range electrostatic repulsion. Here, one has to distinguish between two energy contributions:
(i) On a molecular level, all interactions of lipid molecules take place within an effective inter–molecular pair potential. It is commonly described by a strong, short-ranged core repulsion and a less pronounced, uniform long-range contribution. A

very popular and widely used pair–potential is the Lennard–Jones 12–6 potential:

$$v(r) = 4\epsilon \left[\left(\frac{\sigma}{r} \right)^{12} - \left(\frac{\sigma}{r} \right)^{6} \right] , \tag{4.7}$$

with σ being an collision diameter where $v(r) = 0$. The long-range attractive interactions arise from spontaneous fluctuations in the electric charge distribution of atoms that induce electric moments on other atoms. This causes multipolar dispersion interactions, which can be represented by a power law series. The strongest contribution arises from dipole-dipole interactions (r^{-6}). Higher order terms of weak dipole-quadrupole (r^{-8}) or quadrupole–quadrupole (r^{-10}) interactions are usually neglected. An adequate representation of short range repulsive forces would be represented by an exponential function for relatively small ranges of r (Hansen and McDonald, 2008, p. 4). They originate from an overlap of outer electron shells at close proximity of molecules. Mainly for mathematical reasons (e.g. limiting cases of $r \to \infty$ and $r \to 0$), it is common to use an inverse–power law with high exponent for short-range repulsion. Major impact on the structural behavior of liquid mixtures plays the short-range force that scales with the mixing state, i.e., the length of boundary line between separated phases and entropic contributions. As described in Section 4.2, a thermodynamic approach to describe this multitude of particle pair–interactions is introduced by the definition of the line tension in Equation 4.5. The line tension is difficult to access by measurements. In this thesis, I calculate the line tension based on molecular sizing of lipids that is further discussed in Section 5.3.
(ii) A second energy contribution arises from effective potentials on inter–domain length scales. Permanent dipole contributions from charged lipid head groups or dipolar chain termini lead to repulsive long range interaction potentials that integrate over the complete size of the demixed system. The magnitude and shape of long-range potential is responsible for the formation and arrangement of superstructures, like domains or stripe phases (see Section 4.6). In case of disc-like, isolated domains the long range inter–domain potential can be superimposed by a discrete point-like interaction potential with spherical symmetry. The simplest model to think of are hard discs with diameter *d*, where the pair potential *v(r)* at a separation *r* becomes infinity on disc contact. To account for long-range contributions, the so called hard–core Yukawa potential introduces additionally a potential well of depth/height ϵ with exponential decay–length λ:

$$\begin{aligned} v(r) &= \infty, && r < d, \\ v(r) &= \mp \epsilon e^{-\lambda(r-d)}, && r \geq d. \end{aligned} \tag{4.8}$$

A similar strategy is used in Section 4.7. There, the electrostatic potential of disc-like domains in hexagonal arrangements is superimposed by point-like dipoles on discrete lattice sites. To calculate the total amount of energy stored in a system, it first appears reasonable to start with a molecular description and then further extend the strategy towards modulated superstructures. In the following, important structural parameters for isolated systems are derived which will be corrected in a second step for long range inter–domain interactions.

4.4. Equilibrium Radius of Domains

Equation 4.6 defines the total free energy of a phase-separated system constituted by three major terms, i.e., bulk energy F_0, line energy F_λ, and electrostatic energy F_{el}. The free energy contribution F_λ from the line tension of a single circular domain with radius R scales proportional to its perimeter:

$$F_\lambda = 2\pi R\lambda \ . \tag{4.9}$$

As discussed in Section 4.3, a term from electrostatic energy F_{el} arises due to dipole interactions of the lipid molecules. These dipole energies must be added over all intermolecular long range interactions present in the system. A convenient way to address this problem was introduced by McConnell and Moy (1988) as a simple lattice model. In this model, all molecules occupy one lattice site of rectangular shape with an interlattice distance Δ. As long as the distance $r = |r_1 - r_2|$ between two molecules can be considered large compared to Δ, the interaction potential can be assumed to be of dipolar shape, i.e., $\propto r^{-3}$ (de Koker and McConnell, 1993). Integration over all possible lattice site interactions leads to the electrostatic energy F_{el}:

$$F_{el} = const - \frac{1}{4\pi\epsilon_0}\frac{\mu(r)^2}{2}\iint \frac{dr_1^2 dr_2^2}{\sqrt{(r_1 - r_2)^2 + \Delta^2}^3} \ . \tag{4.10}$$

The constant in Equation 4.10 accounts for electrostatic contributions to the bulk energy and line tension, whereas the second term represents all long range dipolar interactions (McConnell and Moy, 1988). It should be emphasized, that all formulas presented in this study are given in SI units, which requires a prefactor of $1/4\pi\epsilon_0$ for Coulombs law. Accordingly the difference in dipole density $\mu(r) = \frac{p}{\Delta^2}$, with p being the molecular dipole moment, between the two phases (A and B) is defined in analogy to Wurlitzer et al. (2002) as:

$$\mu(r) = \begin{cases} \sqrt{2\pi\epsilon_{\text{eff}}}\epsilon_0(V_B - V_A) & \text{if } r \in \text{phase B}, \\ 0 & \text{if } r \in \text{phase A}. \end{cases} \tag{4.11}$$

Note that the dipole density of phase A is set to zero and its contribution is already included in the bulk energy term F_0 of Equation 4.6. Within a binary monolayer, where neither the total area of the system nor the fraction of the two phases change, one of the two dipole densities acts as a constant background (McConnell, 1991) and only the difference in dipole density is of interest for phase modulation. The introduced cut–off parameter Δ prevents the integral of Equation 4.10 from diverging and is in magnitude close to the separation of the molecular dipoles (McConnell, 1991). In literature, different approaches for evaluation of this double area integral are discussed (McConnell and Moy, 1988; Deutch and Low, 1992; McConnell and de Koker, 1992; Wurlitzer, 2001), leading to distinct differences in the cut–off parameter Δ. In the following, I will use the more recent approach that leads to an electrostatic energy of a single isolated, circular domain with perimeter $2\pi R$ to be:

$$F_{el} = const. + \frac{2\pi R}{4\pi\epsilon_0}\mu^2 \ln\frac{e\Delta}{8R} \ . \tag{4.12}$$

Here, e is Euler's constant and ϵ_0 the dielectric constant, whereas the effective dielectric permittivity is included within the definition of μ. Equation 4.9 together with Equation 4.12 can be substituted into Equation 4.6 to write the total free energy for a system with $N = \frac{A_B}{\pi R^2}$ circular, non–interacting domains. For a fixed area A_B of molecules B in condensed phase the following holds:

$$F = F_0 + 2\pi R N \left(\lambda + \frac{\mu^2}{4\pi\epsilon_0}\ln\frac{e\Delta}{8R}\right) \ . \tag{4.13}$$

The constant term F_0 has no influence on the minimal total free energy F of the system, and will be dropped in the following. Under equilibrium conditions F in Equation 4.13 minimizes and the derivative,

$$\frac{\partial}{\partial R}\left(\frac{a}{R} + \frac{b\log(\frac{c}{R})}{R}\right) = -\frac{a}{R^2} - \frac{b\log(\frac{c}{R})}{R^2} - \frac{b}{R^2} \ , \tag{4.14}$$

becomes zero. This defines an equilibrium radius R_{eq} for all domains, where the total free energy is minimal:

$$R_{eq} = \frac{e^2\Delta}{8}\exp\left(\frac{4\pi\epsilon_0\lambda}{\mu^2}\right) \ . \tag{4.15}$$

4.5. Radius Fluctuations

The presented derivation of R_{eq} in Section 4.4 minimizes the total free energy of a fixed mole fraction of phase separated molecules, with regard to the number N of equally sized domains. This implies a process where domains with constant radius are created or broken up. Thus, the system would need to overcome large activation energies (McConnell, 1991) which is rather unlikely to happen. In reality, during monolayer compression the formation of domains overcomes a nucleation process, after which domains will grow in area until a complete phase separation is reached. To reach equilibrium size R_{eq}, a spontaneous equilibration process is needed, where condensed molecules can exchange between domains. I first express the energy

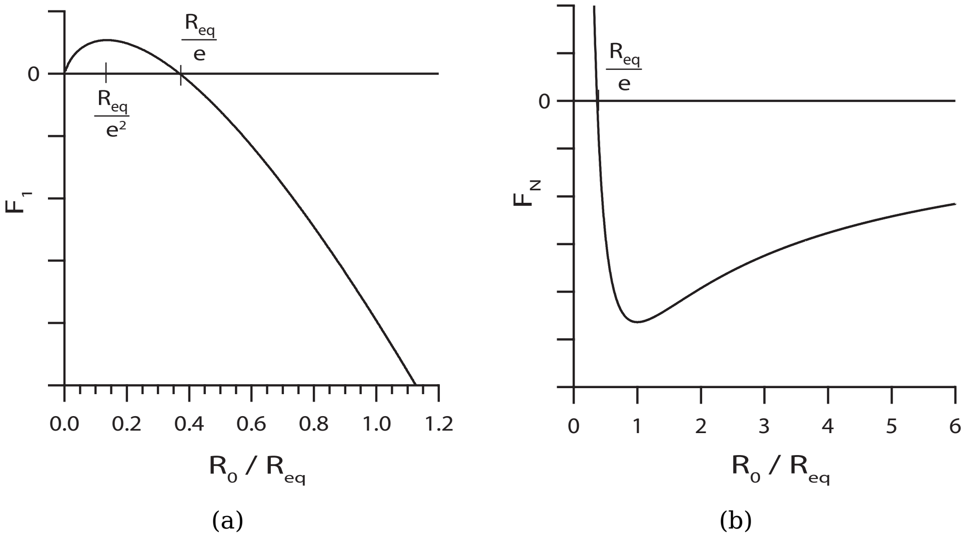

Figure 4.1.: (a) Total free energy of a single domain plotted against its normalized radius R_0/R_{eq} (b) Total free energy of $N \propto \frac{1}{R_0^2}$, non–interacting domains.

(Equation 4.13) of a single, isolated domain with radius R_0 in terms of its equilibrium radius (Equation 4.15):

$$F_1 = R_0 \frac{\mu^2}{2\epsilon_0} \ln \frac{R_{eq}}{eR_0}. \tag{4.16}$$

From Equation 4.16 it is apparent that the energy of a single, isolated domain becomes maximum for a critical radius of $R_c = R_{eq}/e^2$, where the first derivative of $\partial F_1/\partial R_0$ equals zero and its second derivative $\partial^2 F_1/\partial^2 R_0 = -(\mu^2/2\epsilon_0 R_0)$ remains always negative. R_c must be exceeded for any nucleation process before a domain can gain energy and will grow further, even beyond R_{eq} (Figure 4.1a). At $R_0 = R_{eq}/e$ the line tension and electrostatic forces are exactly balanced at the domain boundary. The total free energy for $N \propto \frac{1}{R_0^2}$ domains is shown in Figure 4.1b. F_N finds its minimum at R_{eq} and only domains larger than $R_0 = R_{eq}/e$ are in favor of the total energy. $R_{min} = R_{eq}/e$ should be detectable as lower domain size limit and can be used as upper limit to estimate R_{eq}. As the next step, an area conserving exchange of molecules χ between a pair of domains with radii $R_0(1+\chi)^{1/2}$ and $R_0(1-\chi)^{1/2}$ is considered. The total free energy of any given pair yields:

$$F_2 = R_0 \frac{\mu^2}{2\epsilon_0} \left[(1+\chi)^{1/2} \ln \frac{R_{eq}}{eR_0\,(1+\chi)^{1/2}} + (1-\chi)^{1/2} \ln \frac{R_{eq}}{eR_0\,(1-\chi)^{1/2}} \right]. \tag{4.17}$$

The minimization of the Helmholtz free energy of the total system therefore reduces to the minimization of all pairs of domains (McConnell and de Koker, 1996). The size

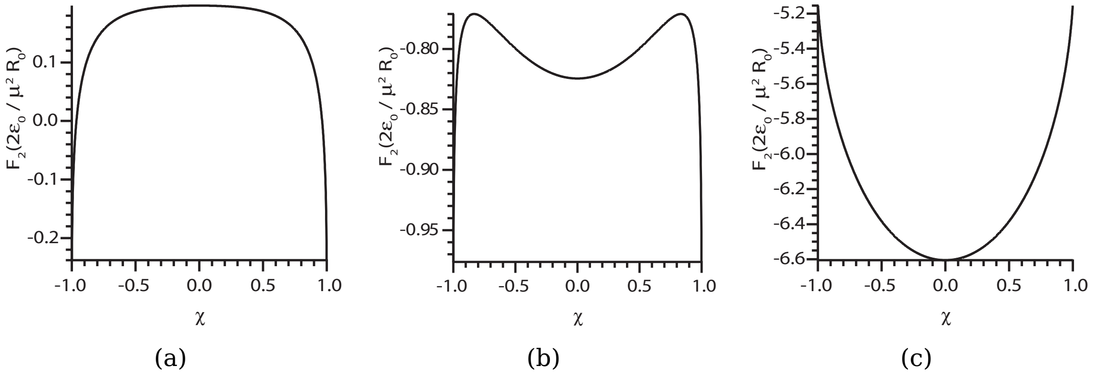

(a) (b) (c)

Figure 4.2.: (a) Energies F_2 (Equation 4.17) for a pair of domains with symmetric radius fluctuations $R_0(1-\chi)^2$ and $R_0(1+\chi)^2$ in units of $2\epsilon_0/\mu^2 R_0$. Minima at $\chi \pm 1$ cause annihilation of domains wheras minima at $\chi = 0$ provide metastable energy levels for domain size equilibration. Ratios of R_0/R_{eq} are (a) 3.0, (b) 1.8, and (c) 0.1.

equilibration process of domains as described by Equation 4.17 has three regions of interest that are exemplarily shown in Figure 4.2:

$R_0 < R_{eq}/e$:

For all values of χ the slope of $\partial F_2/\partial\chi$ is negative (Figure 4.2a). Whereas the larger domain will grow until it reaches the energetically stable region above R_{eq}/e, the smaller domain annihilates and reduces the number N of domains. The remaining domain can grow from this process to a maximum radius of $\sqrt{2}R_0$.

$R_{eq}/e < R_0 < eR_{eq}$:

The energy function of Equation 4.17 has three minima. One for $\chi = 0$ and each with $\chi = \pm 1$. For small fluctuations χ, both domains will equilibrate and stabilize at their average domain radius R_0, where the energy function finds a metastable minimum (Figure 4.2b). If the fluctuation is bigger than $(\frac{R_{eq}}{e^2 R_0})^2 - 1$, then the domains are unstable and the bigger one will grow to an area of $\sqrt{2}R_0$, whereas the smaller one annihilates.

$eR_{eq} < R_0$:

For all values of χ the slope of $\partial F_2/\partial\chi$ is positive (Figure 4.2c). A pair of domains will equilibrate until they both reach the same metastable mean radius R_0.

Domains that equilibrate are metastable with respect to a small exchange of molecules between the two phases. It should be noted, that above R_{eq}/e a broad

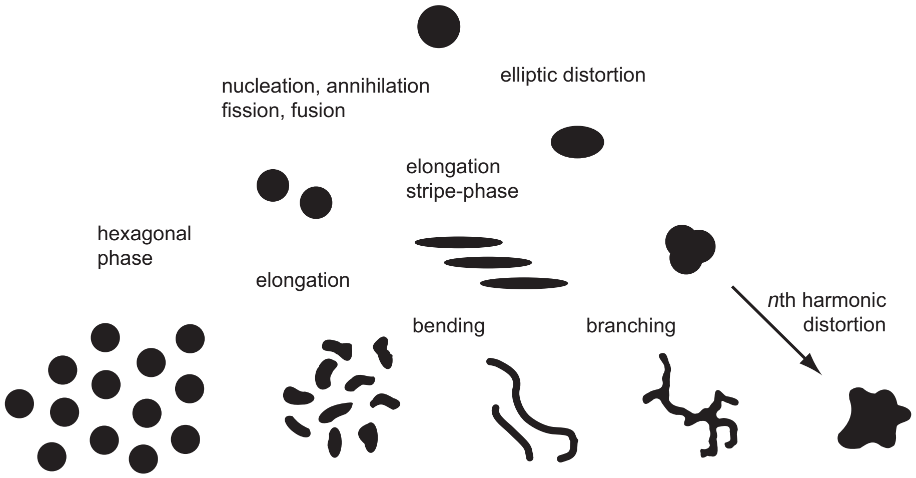

Figure 4.3.: Overview on shape transitions of domains as balance of attractive and repulsive interactions. Adapted from Seul and Andelman (1995).

distribution of metastable domain radii is possible. Dependent on the starting conditions, the compression parameters, and the monolayer history, a random distribution of domain sizes can be reached through domain fission, fusion, creation and annihilation (McConnell and de Koker, 1996; Nag and Boland, 1991).

4.6. Shape Transitions

With increasing domain size repulsive interactions of individual dipoles become more dominant. Thus, elongate shapes of domains are energetically preferred to ensure maximal distance between dipoles. A coarse graphical overview of possible shape transitions is presented in Figure 4.3. The first observed shape instability goes from circular to elliptic shape and is followed by transitions that may split up the modulated phases into higher harmonic distortions, elongated stripes, hexagonal phase arrangements, or highly branched stripe phases. Such shape transitions were theoretically explained by many authors, e.g. Vanderlick and Möhwald (1990); Seul and Andelman (1995); Andelman et al. (1987). Since this study deals with stable, circular domains aligned in hexagonal superstructures, only two major aspects of elliptic shape transitions will be emphasized. As could be demonstrated by Keller et al. (1987); de Koker and McConnell (1993), the first circular mode becomes unstable for $R_0 \geq e^{\frac{1}{3}} R_{eq}$. This offers an upper limit R_{max} for domains with circular shape. Domains larger than R_{max} are trapped in a metastable energy minimum, as discussed in Section 4.5. Experimental observation of these domains allows an estimate on the lower limit of $R_{eq} \geq e^{-\frac{1}{3}} R_{max}$. Another interesting aspect of shape transitions is the ratio between line tension and electrostatic forces. From the instability condition one can estimate the range of the material parameter m of circular domains according to de Koker and McConnell (1993):

$$m = \frac{4\pi\epsilon_0\lambda}{\mu^2} > \ln\left(\frac{8R_{max}}{\Delta} - 3 - \frac{1}{3}\right). \tag{4.18}$$

To demonstrate the importance of this material parameter on shape transitions, a rather simple and qualitative approach of coarse-grained molecular dynamics computer simulation was taken. Here, the electrostatic contribution of interacting particles was gradually increased.

4.6.1. Dissipative Particle Dynamics Simulation

Dissipative particle dynamics (DPD) simulation is a fast and flexible approach to simulate colloidal suspensions even under complicated flow conditions (Español and Warren, 1995; Hoogerbrugge and Koelman, 1992). Particles are regarded as coarse grained groups of molecules that interact collectively with neighboring groups. This tremendously reduces computing power. As a consequence, each collision process between fluid particles no longer requires conserving energy, but the total momentum of the system must still be conserved. The simplest ways to introduce dissipation are expansion terms of random (thermal) and viscous–frictional forces (Español and Warren, 1995). In this study, DPD simulation was used to exemplarily show the formation of modulated phases as interplay between long range electrostatic forces (F_{el}) and short range bulk and interfacial forces ($F_0 + F_\lambda$), as postulated for Equation 4.6. In Figure 4.4 screen shots of stable DPD simulations for two–dimensional binary mixtures of 3600 particles with periodic boundary conditions are shown. The number of yellow particles, representing fluorinated lipids, was fixed to 1200 and the temperature coefficient remained unchanged. An initial random particle distribution is shown in Figure 4.4a. Here, repulsive intermolecular forces decrease linearly for all types of particles (equivalent types of particles), and no long-range electrostatic forces are present. The suspension remained randomly mixed and can be regarded as equilibrated. As soon as repulsive interfacial forces between fluorochain (yellow) and alkylchain (green) lipids are introduced, the suspension completely demixes into two isolated phases (Figure 4.4b). In Figure 4.4c electrostatic forces (represented as red rings) for fluorinated particles were additionally turned on. After the equilibration process, the lipids arranged in domain like phases without preferred direction. Afterwards, no further particle exchange between domains was observed and thus the size distribution was rather dependent on the initial mixing state. For Figure 4.4(d-f) the electrostatic force contribution was successively increased by a factor of 10, 100 and 400. Similar to the phase transitions presented in Figure 4.3, the binary mixture of domains undergoes transitions to elongated (Figure 4.4d), bent stripe phase (Figure 4.4e), and branched (Figure 4.4f) stripe phase. The presented simulation was done with the software Sandbox (OneZero Software, Canada) written by Adam MacDonald in the

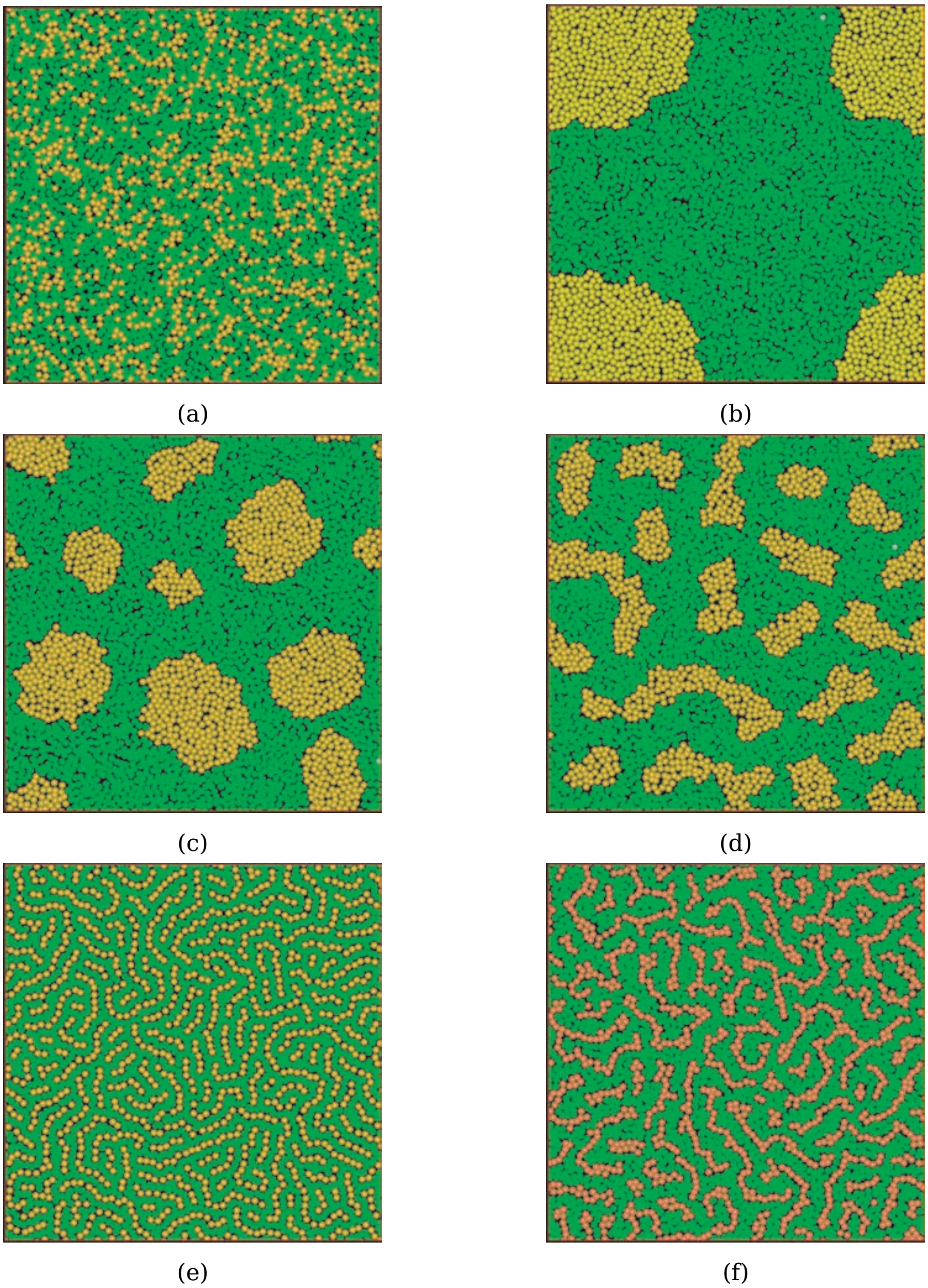
(a) (b) (c) (d) (e) (f)

Figure 4.4.: Dissipative particle dynamics simulation for mixtures of fluorinated (yellow) and alkylchain (green) lipids. (a) Initial random distribution of particles with (b) repulsive inter–particle forces. Domain shape transitions occur after stepwise increase of electrostatic repulsion between fluorinated lipids to form (c) separated domains, (d) elongated domains, (e) elongated stripe phases, and (f) branched stripe phases.

laboratory of Prof. David Pink (Department of Physics, St.Francis Xavier University, Antigonish, Canada). Since a detailed insight into the source code was not possible, the results lack an exact scaling between spatial dimensions and multiplying force factors. Therefore, the presented numerical electrostatic multiplications remain solely qualitative. Nevertheless, the presented DPD simulation method is useful to demonstrate the overall phase behavior of charged lipid mixtures.

4.7. Domain–Domain Interactions

The preliminary discussion on domain sizes and shapes assumed a diluted system of isolated domains. As the concentration of domains increases, the long range electrostatic interactions will also cause domain–domain repulsion. Therefore, the total free energy (Equation 4.6) needs to be augmented by an additional electrostatic inter–domain energy term F_{el}^{d}. An ordering into superstructures will occur as soon as the inter–domain energy exceeds the thermal energy k_BT, i.e., radial symmetric domains will arrange in hexagonal phase. F_{el}^{d} can be calculated by a modulated dipole density μ^d that interacts via a radial interaction potential $v(r)$ as:

$$F_{el}^{d} = \frac{1}{8\pi\epsilon_0} \iint \mu^d(r) v(r - r') \mu^d(r') d^2r d^2r' \; . \tag{4.19}$$

As described by Wurlitzer et al. (2002) and sketched in Figure 4.5, the dipole density modulations of a hexagonal phase can be expressed by the two unit vectors a_1 and a_2 of the primitive vector cell:

$$\mu^d(r) = \mu \sum_{n,m} \Theta\left(R - |na_1 + ma_2 + r|\right) \; , \tag{4.20}$$

where Θ denotes Heaviside's step function and R the domain radius. The latter determines the area fraction Φ of the condensed phase during compression, as:

$$\Phi = \frac{\pi R^2}{|a|^2 \sin\frac{\pi}{3}} \; . \tag{4.21}$$

It should be noted that Φ has a critical upper limit of $\Phi_c = 0.91$, where domains touch each other and must undergo shape changes due to geometrical constrains. McConnell (1986) approximated Equation 4.19 for large inter–domain distances by a point-like dipole interactions, whereas Wurlitzer (2001) treated the integral in a more precise way for dipolar discs with varying distance. This leads to a total free energy of the complete system with area A to be:

$$F_{tot} = \frac{2A\phi}{R}\left(\lambda + \frac{\mu^2}{4\pi\epsilon_0}\ln\frac{e\Delta}{8R} + \frac{\mu^2}{4\pi\epsilon_0}Y(\Phi)\right) \; , \tag{4.22}$$

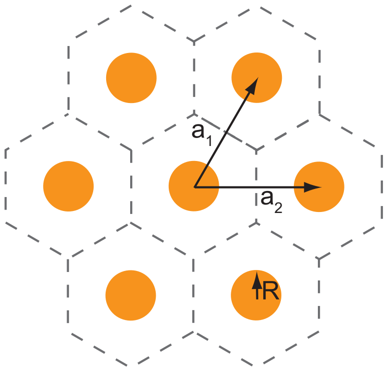

Figure 4.5.: Schematic representation of domains with radius R aligned in a hexagonal superlattice with the two primitive unit cell vectors a_1 and a_2.

using $2\pi NR = 2A\Phi/R$ and $Y(\Phi)$ for $(n,m) \neq (0,0)$:

$$Y(\Phi) = \frac{1}{4\pi} \sum_{n,m=-\infty}^{\infty} \int_0^{\pi/2} dx \frac{(2x - \sin 2x)(\sin 2x)}{(\sqrt{\Phi_c/\Phi_{n,m}} + \cos x)(\sqrt{\Phi_c/\Phi_{n,m}} - \cos x)^2} \cdot E(k)\left[\sqrt{1 - \left(\frac{\sqrt{\Phi_c/\Phi_{n,m}} - \cos x}{\sqrt{\Phi_c/\Phi_{n,m}} + \cos x}\right)^2}\right] \tag{4.23}$$

$E(k) = \int_0^{\pi/2} d\upsilon \sqrt{1 - k^2 \sin^2 \upsilon}$ denotes the elliptic integral of the second kind, where $0 < k < 1$. Equation 4.23 can only be solved numerically by truncating the range of long range dipole intereactions, i.e., the sum over n,m at values that assure reasonable accuracy (error < 0.5%). For diluted systems McConnell and Wurlitzer both attain similar results for the equilibrium radius:

$$R_{eq}^{\Phi} = R_{eq} e^{Y(\Phi)} \cong R_{eq} e^{1.24\Phi^{3/2}} \; . \tag{4.24}$$

For closest packed systems the theory would predict an increase in equilibrium domain radius by a factor of $\exp(Y(\Phi)) \approx 26$. Furthermore, the system minimizes the total free energy F_{tot} (Equation 4.22) by regulating the number density n_{eq} of equilibrated ($R = R_{eq}^d$) domains to:

$$n_{eq} = \frac{N}{A} = \frac{\Phi}{\pi R_{eq}^2} e^{-2Y(\Phi)} \; . \tag{4.25}$$

5. Structural Determination of Lipid Domains

This chapter discusses in detail how the molecular structure of lipids influences size, shape, and density distribution of the fluorinated lipid domains. The molecular structure of fluorinated lipid domains was resolved with high–resolution grazing–incidence X-ray diffraction and specular X-ray reflectivity measurements. The molecular dipole potential of fluorinated monolayers was determined with Kelvin probe measurements and the line tension was derived from the obtained structural results. Afterwards, a detailed analysis of macroscopic domain structure factors was carried out and results were compared to theoretical calculated parameters. A strategy for functional domain modification is presented that allows for flexible biological modification of domains.

5.1. Grazing-Incidence X-ray Diffraction Measurements

Of great interest for this study is the lateral organization of lipids within molecular assemblies. To resolve lateral intermolecular distances between fluorocarbon chains with mesoscopic long range ordering, a wide angle X-ray diffraction technique with high in-plane angular resolution was applied. Therefore, a modified grazing incidence X-ray diffraction (GIXD) technique at the air-water interface (Section 2.8) with an analyzer crystal setup was used at the beamline ID10B of the European Synchrotron Radiation Facility (ESRF) in Grenoble (France). Figure 5.1 presents an overview of the used scattering geometry and lists all necessary scattering angles for data analysis. Details on the instrumental setup are shown in Section 2.8. In the used GIXD setup, the incident beam hits the sample under a fixed vertical angle Θ_i of approximately $80\,\%$ of the critical angle Θ_c ($\Theta_c = 0.15°$ for $E = 8.00\,\mathrm{keV}$ at the air-water interface). Below Θ_c total reflection occurs and an exponentially decaying evanescent field penetrates into the bulk medium. This reduces substantially the background signal caused by the substrate and makes the technique surface sensitive for thin stratified layers. An high horizontal (q_{xy}) angular detection resolution was achieved by a linear point-sensitive detector (PSD) lined up in sequence with a Si(111) analyzer crystal optics. The crystal can be rotated around the z-axis by an angle τ. To reach the highest out of plane (q_z) detection range, the PSD is aligned in an asymmetric way such that the direct beam k_f with zero vertical momentum transfer ($q_z = 0$) hits the lower part of the detector.

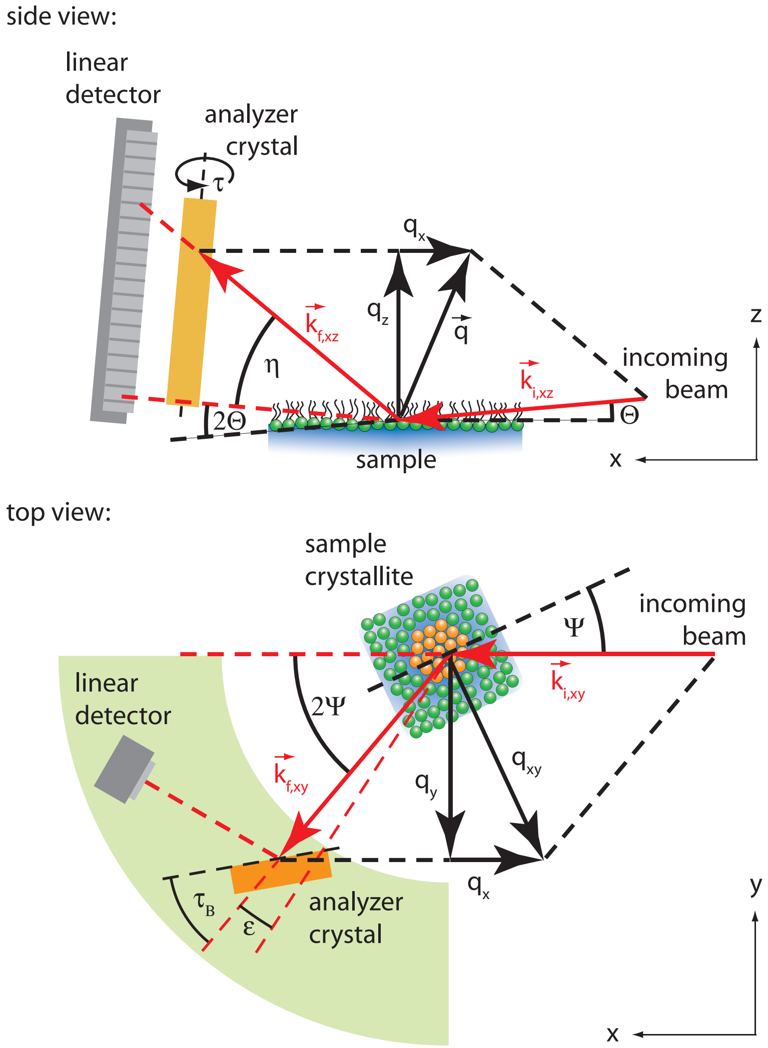

Figure 5.1.: Sketch of the experimental scattering geometry for grazing incidence X-ray diffraction technique as (*Top*) side view and (*Bottom*) top view.

For the direct beam, the analyzer crystal was aligned in a way that it fulfills Bragg condition with $\tau - 2\tau$ between the diffracted beam and its extension line towards the PSD (Smilgies, 2003). This assures that only diffracted X-rays within a narrow energy range, i.e., defined scattering vector, can reach the detector. Since the analyzer crystal optics reduces tremendously the intensity of the detected signal, it is only practical for samples exhibiting a high scattering signal and X-ray sources providing a high flux. Both requisites are fulfilled by fluorocarbon chain lipids and a high brilliance synchrotron radiation source, respectively. Compared to a commonly used Soller collimator setup with angular resolution of around $\Delta\Psi = 0.06°$ ($\Delta q_{xy} = 4 \times 10^{-3}\,\text{Å}^{-1}; \lambda = 1.55\,\text{Å}$), the analyzer crystal setup allows high–resolution scans of $\Delta\Psi = 0.002°$ ($\Delta q_{xy} = 10^{-4}\,\text{Å}^{-1}$). Only for data evaluation, the intensity maps must be corrected for out of plane distortion. An angular scan with fixed crystal–detector (τ_B) configuration yields a bent Bragg sheet, since with increasing q_z momentum the q_{xy} component decreases and fulfills Bragg condition only under a higher out–of plane diffraction angle 2Ψ. The detuning angle $\epsilon(\eta)$ can be calculated for the presented setup with a reference beam ($q_z = 0$) at $\tau_{ref} = \tau_B$ according to (Smilgies, 2003):

$$\epsilon(\eta) = \arcsin(\frac{\sin(\tau_B)}{cos(\eta)}) - \tau_{ref} \; . \tag{5.1}$$

The corrected intensity map allows transformation of the scattering vector k_f into its scattering vector components q_z and q_{xy} by:

$$q_z = \frac{2\pi}{\lambda}(\sin(\Theta_i) + \sin(\eta - \Theta_i)) \; , \tag{5.2}$$

$$q_x = \frac{2\pi}{\lambda}(\cos(\eta - \Theta_i)\sin(2\Psi)) \; , \tag{5.3}$$

$$q_y = \frac{2\pi}{\lambda}(\cos(\eta - \Theta_i)\cos(2\Psi) - \cos(\Theta_i)) \; , \tag{5.4}$$

$$q_{xy} = \sqrt{q_x^2 + q_y^2} \; . \tag{5.5}$$

GIXD scans that integrated over the whole accessible q_z space revealed a single, strong diffraction peak between $q_{xy} = 1.26\,\text{Å}^{-1}$ to $1.28\,\text{Å}^{-1} \pm 0.01\,\text{Å}^{-1}$ for all fluorinated molecules (Oelke, 2008; Kaindl et al., 2010). The high resolution analyzer crystal GIXD scans for FL10 and FL17 lipid domains are shown in Figure 5.2(a–b). Fluorinated lipid domains were measured for $50\,\text{mol\%}$:$50\,\text{mol\%}$ FL*n*:DOPC lipid mixtures at the air-water interface at a constant surface pressure of $20\,\text{mN}\,\text{m}^{-1}$. The bent data range originates from retuning the analyzer crystal according to Equation 5.1. Both Bragg rods show maxima around $q_z = 0.00\,\text{Å}^{-1}$ and a lateral scattering component q_{xy} of $1.271\,\text{Å}^{-1} \pm 0.002\,\text{Å}^{-1}$ for FL10 and $1.287\,\text{Å}^{-1} \pm 0.002\,\text{Å}^{-1}$ for FL17. These observations already allow for basic conclusions on the two–dimensional lattice structure of fluorinated lipid monolayers. The existence of only one out of plane diffraction peak suggests a symmetric unit cell with equidistant nearest

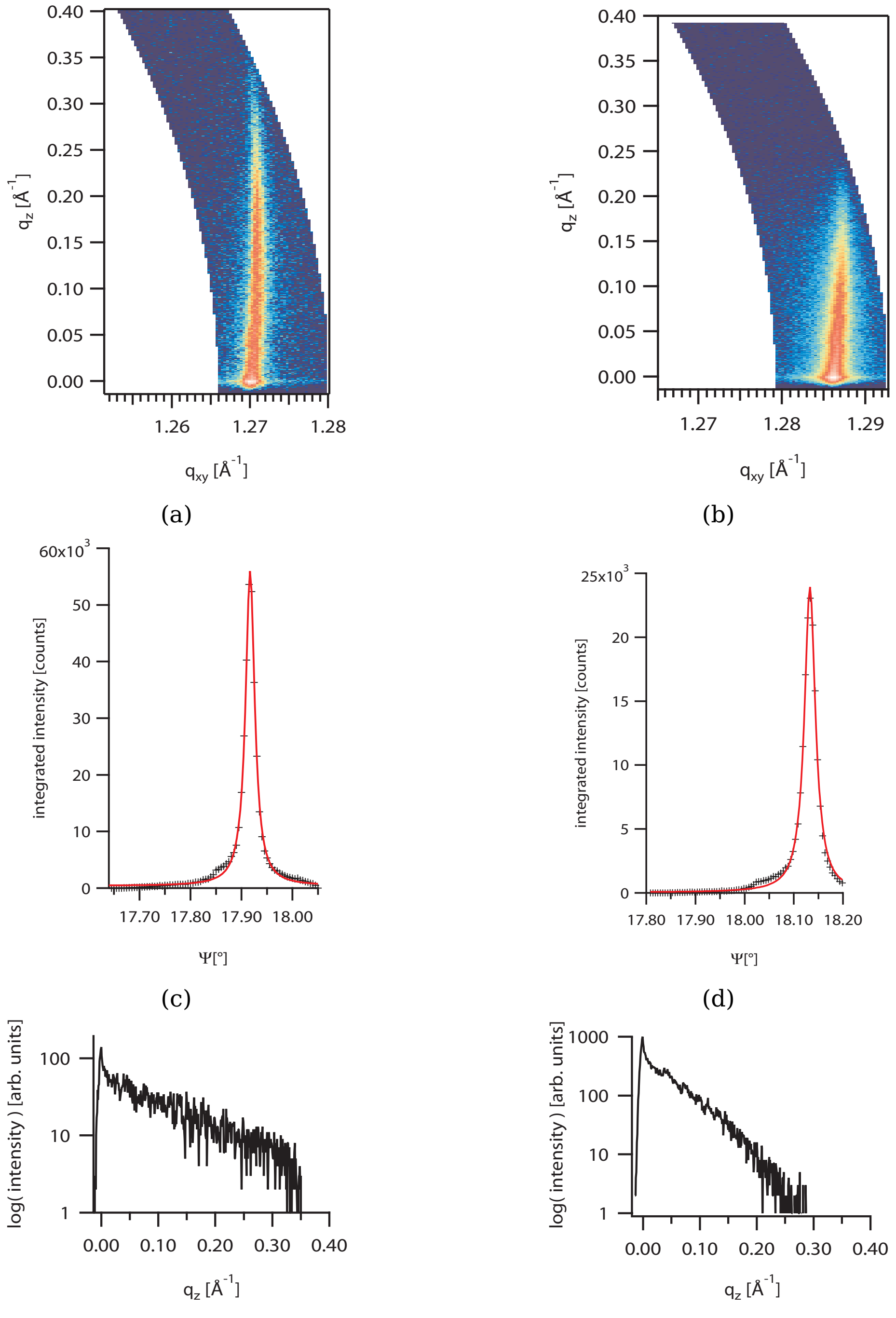

(a) (b)

(c) (d)

(e) (f)

Figure 5.2.: High resolution reciprocal space maps of (a) FL10 and (b) FL17 diffraction peaks after correction of q_z distortion. Intensity profiles integrated along q_z show good conformance with fits of Lorenzian line shape (red lines) for (c) FL10 and (d) FL17. The deduced full width at half maximum (FWHM) allows an estimate on the crystallite size. The expansion of the Bragg sheet into q_z is shown for (e) FL10 and (f) FL17.

neighbour spacing between lipid chains. This scenario is given for a hexagonal unit cell with perpendicular lipid chain orientation with respect to the surface (Als-Nielsen et al., 1994), i.e., a closest packed crystalline phase without molecular tilt. The position of the lateral scattering component q_{xy} yields a scattering plane distance $d^{plane} = 2\pi/q_{xy}$ of $d^{plane}_{FL10} = 4.943\,\text{Å} \pm 0.008\,\text{Å}$ and $d^{plane}_{FL17} = 4.882\,\text{Å} \pm 0.008\,\text{Å}$ that calculates an intermolecular chain to chain distance for hexagonal packing of $d^{mol}_{FL10} = 5.708\,\text{Å} \pm 0.009\,\text{Å}$ and $d^{mol}_{FL17} = 5.637\,\text{Å} \pm 0.009\,\text{Å}$. The results found agree well with values reported from crystallography of fluorinated lipids (Bunn and Howells, 1954) and are a good estimate of the theoretical intermolecular cut–off dipole distance Δ introduced in Equation 4.10. High-resolution GIXD furthermore allows determination of the correlation length L of scatterers and thus the size of fluorinated lipid crystallites. Figure 5.2(c–d) show q_z integrated intensity profiles (black data points) of the respective FL10 and FL17 Bragg rods along Ψ in angular units. Both profiles were fitted (red lines) in good conformance by a Lorenzian line shape of width $W_{FL10} = 0.021° \pm 0.002°$ and $W_{FL17} = 0.024° \pm 0.002°$. Quantitatively using the Scherrer formula,

$$W(\Delta\Psi) = 0.93\lambda/L\cos(2\Psi), \tag{5.6}$$

a crystallite size of around $L_{FL17} = 0.32\,\mu\text{m} \pm 0.03\,\mu\text{m}$ was found. In Equation 5.6 the numerical prefactor of 0.93 is particle shape dependent and can vary between different approximation methods (Patterson, 1939). This diminishes the accuracy of the presented result. Nonetheless the result is remarkable, since it demonstrates that the fluorinated lipid chains are highly correlated over macroscopic dimensions. For FL17 molecules the correlation length L approximates to the same size as it was found for its domain diameter d_{FL17} by fluorescence microscopy (Section 5.5). This result suggests that the complete domain consists of a single fluorolipid crystallite, a result that could only be obtained due to the high instrumental resolution ($\Delta_{Inst} = 0.002°$) provided by the analyzer crystal setup. For instance, by use of a Soller setup, the measured width $W(\Delta\Psi)$ would be completely affected by the instrumental resolution of approximately $\Delta_{Inst} \approx 0.06°$ that broadens the real width (W_{real}) of the Bragg peak as,

$$W(\Delta\Psi) = \sqrt{(W_{real})^2 + (\Delta_{Inst})^2}. \tag{5.7}$$

At the same time, it is shown that larger FL10 domains arrange in similar crystallite structures. The correlation length for FL10 domains was approximated as $L_{FL10} = 0.41\,\mu\text{m} \pm 0.04\,\mu\text{m}$ and hence large FL10 domains are thought to accumulate from multiple small crystallites. The high correlation length in lateral *xy*-direction has also an impact on the vertical scattering length q_z. Since the linear molecules align in perfect upright orientation, i.e., perpendicular to the surface, the scattering form factor will be a flat oblate ellipsoid that overlaps with the complete length h of the molecules in reciprocal space (Kjaer, 1994). That means, the longer the

Table 5.1.: GIXD scattering vector components q_{xy} and q_z for fluorinated lipid molecules FL10, FL13 and FL17. The calculated diffraction plane distance d^{plane} and intermolecular chain-chain distance d^{mol} for hexagonal packing, and the Bragg rod width W with approximated correlation length L of fluorinated lipid crystallites.

	unit	FL10	FL13	FL17	FL10Man
q_{xy}	$Å^{-1}$	1.271 ± 0.002	1.28 ± 0.01	1.287 ± 0.002	1.27 ± 0.01
q_z	$Å^{-1}$	0.00 ± 0.05	0.00 ± 0.05	0.00 ± 0.05	0.00 ± 0.05
d^{plane}	Å	4.94 ± 0.01	4.94 ± 0.04	4.88 ± 0.01	4.96 ± 0.04
d^{mol}	Å	5.708 ± 0.009	5.70 ± 0.05	5.637 ± 0.009	5.73 ± 0.05
W	°	0.021 ± 0.002		0.027 ± 0.002	
L	µm	0.41 ± 0.04		0.32 ± 0.03	

molecule, the narrower and more intense becomes the Bragg rod width $2\pi/h$ in q_z-direction. Figure 5.2 (e-f) shows the Bragg rod profile along q_z at the lateral peak position $1.271\,Å^{-1}$ for FL10 and $1.287\,Å^{-1}$ for FL17. At $q_z = 0$ the Bragg rod is truncated by the total reflection of the water subphase. In direct connection, a sharp Vineyard-Yoneda peak (Vineyard, 1982) appears, arising from the interference of upwards diffracted X-rays and those that were reflected back upwards again after reflection at the air–water interface. The breadth of the Bragg rod clearly extends further into q_z-space for FL10 molecules. Since surface roughness and exact molecular form factors drastically influence the diffuse scattering signal (Als-Nielsen and McMorrow, 2001), a more precise in-plane X-ray reflectivity measurement method was applied to deduce the molecular length of fluorinated lipids. In the following Section 5.2, the monolayer thickness h is deduced from specular Θ–2Θ scans at the air-solid interface. An overview of the most important parameters extracted from high-resolution GIXD experiments is listed in Table 5.1.

5.2. Specular X-ray Reflectivity Measurements

The molecular length of fluorinated lipids was resolved by specular Θ–2Θ X-ray reflectivity measurements at the air–solid interface. Specular X-ray reflectivity measures the intensity I_r of a reflected beam with a point detector in the plane of incidence ($\Psi = 0$) at specular position. Structural information of the sample is deduced from the dependency of Fresnel reflectivity $R_f(q_z) = I_r(q_z)/I_0$ on the vertical momentum transfer q_z of scattered X-rays. Under specular condition, the momentum

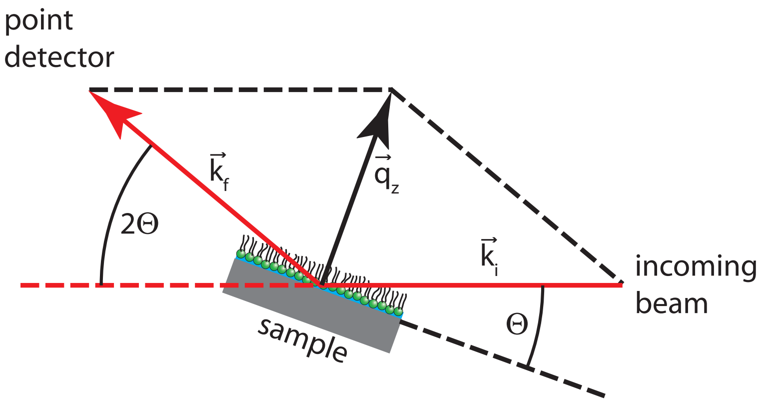

(a)

Figure 5.3.: Sketch of the specular Θ–2Θ X-ray reflectivity scattering geometry.

transfer $\vec{q}$ of X-rays is only given in z-direction:

$$\vec{k_f} - \vec{k_i} = \vec{q} = q_z. \tag{5.8}$$

As the scattering process is regarded mainly as an elastic process ($|k_f| = |k_i|$), the magnitude of the reciprocal scattering vector q_z is

$$q_z = 2k_i \sin\Theta. \tag{5.9}$$

The incident wave vector magnitude $\vec{k_i} = 2\pi/\lambda$ was refined to a monochromatic wavelength $\lambda = 1.55\,\text{Å}$ (see Section 2.8). Figure 5.3 presents a schematic overview of the specular scattering geometry. An X-ray beam that impinges on a flat surface is partially reflected and transmitted across the interface. The intensity of the reflected beam $R_f = |r|^2$ is well described by the Fresnel reflection coefficients r (Hecht, 2001). The polarization state for X-rays needs in good approximation not to be considered (Parratt, 1954) and thus $r = r_{\|} = r_{\perp}$ equals for parallel ($\|$) and perpendicular ($\perp$) polarization. The short wavelength λ of X-rays and their high scattering cross section on electrons makes X-ray scattering techniques sensitive to surface fluctuations on an atomic level. This requires that topological surface roughness or gradients of electron densities must be considered in data evaluation. For roughness fluctuations resulting from a Gaussian distribution of width σ, the interface reflection coefficient between two layers (j and $j+1$) can be modified by a damping factor according to Croce and Névot (1975):

$$r_{j(j+1)} = \frac{k_j - k_{j+1}}{k_j + k_{j+1}} \exp(-2k_j k_{j+1} \sigma^2_{j(j+1)}). \tag{5.10}$$

Stratified systems cause multiple reflections between the layers j, where formulas for Fresnel reflectivity must be applied for each interface reflection. An intrinsically mathematical way to avoid explicit consideration of each back reflection was first introduced by Abelès (1950). Model-based fitting routines use this formalism to calculate reflectivity curves with pre-estimated model parameters. The estimated model requires knowledge on layer structure and refractive indices of each layer. Subsequently, a reflectivity curve is calculated and compared to the measured data. By variation of the model parameters (interface roughness, layer thickness, electron density), an increased match between model and experiment is found until an acceptable accuracy is reached. For the presented reflectivity curves, this fitting routine was performed using Motofit (Nelson, 2006) on Igor Pro 6.1 (Wavemetrics, Lake Oswego, OR-USA). The spatial resolution of the obtained density profile can be approximated by the sampling theorem $\Delta h \approx \frac{\pi}{q_{max}}$ (Nováková et al., 2006), where q_{max} is the maximum vertical momentum transfer measured of the reflectivity curve. For the presented results this implicates $\Delta h \approx 4.8\,\text{Å}$. However, the performed fitting routine reduces the corresponding errors to $\sim 5\,\%$ of the feature size in q_z, as long as the reflectivity curve shows pronounced fringes and the validity of the fitting model is given.

Figure 5.4 presents the measured (black data points) and best model fitted (red line) reflectivity curve of a FL17 monolayer at the air–silicon interface. The FL17 monolayer was transferred by Langmuir–Blodgett technique (Subsection 2.5.1) at a constant surface pressure of $20\,\mathrm{mN\,m^{-1}}$ onto a hydrophilic silicon wafer. Shorter fluorinated lipids FL13 and FL10man were measured under the same condition and corresponding reflectivity curves and model fits are presented in Section A.4. To model the data, a three slab model for (i) the fluorinated lipid monolayer, (ii) hydrated glycerol head group, and (iii) a silicon dioxide layer was used. The measured truncation edge at the critical angle Θ_c resulted for all model fits in a bulk scattering length density of the silicon substrate close to its literature value of $\rho_{Si} = 20.0 \times 10^{-6}\,\text{Å}^{-2}$ (Daillant and Gibaud, 1999, p. 95). Below the critical angle ($\Theta_c = 0.22°$ for air–silicon at $8\,\mathrm{keV}$) total reflection occurs and the reflected intensity equals $R_f \equiv 1$. The scattering length density (SLD) of the silicon dioxide (SiO_2) layer was constrained to $18.9 \times 10^{-6}\,\text{Å}^{-2}$, since a gradient in oxide concentration is expected. The gradient would reduce the SLD difference towards the Si bulk substrate and result in an underestimated thickness for SiO_2 seen by X-ray reflectivity (Geer et al., 1994). For a constrained SLD, the gradient appears as high roughness value at the SiO_2 interface, that leads to a decay in the SLD profile across the complete width of the silicon dioxide layer (Figure 5.4). All model fitted oxide thicknesses (including measurements from a bare sample) were found between $5\,\text{Å}$ to $7\,\text{Å}$ and fall in acceptable ranges for commercially available silicon wafers. The measured reflectivity curves show Kiessing fringes that allow an estimate on the overall thickness of the transferred monolayer. Position and depth of the first minimum define the thickness of the monolayer and the relative change in SLD compared to the substrate. The main thickness contribution was attributed to the fluorinated lipid chains that revealed a thickness of $20.6\,\text{Å}$ for FL17, $15.8\,\text{Å}$ for

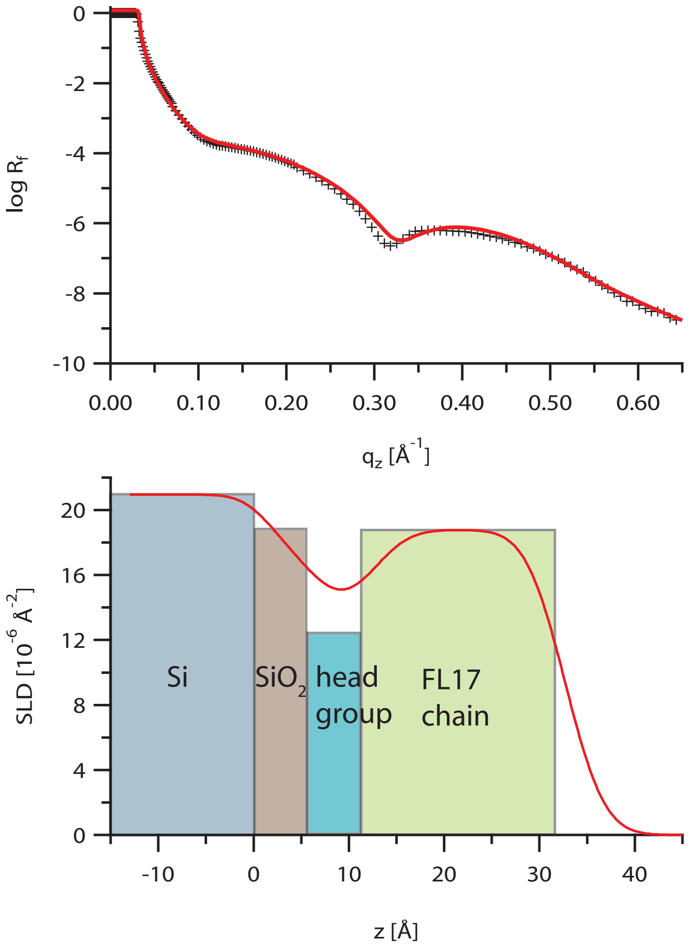

Figure 5.4.: (*Top*) Measured reflectivity curve (black data points) for FL17 monolayer at the air-Si interface and model based fit (red line). (*Bottom*) Scattering length density (SLD) profile of the best fitted model along z-direction. Bars in the background indicate the layer box model.

FL13, and $12.3\,\text{Å}$ for FL10Man. The surface roughness at the air–lipid interface was in the range of $2\,\text{Å}$ to $3\,\text{Å}$ for FL17 and FL13 and was in magnitude comparable to the substrate roughness. Only for FL10Man a doubling of the air–lipid roughness to $5.6\,\text{Å}$ was observed, which can be attributed to the additional mannose moiety at the interface. The additional distortion of the electron density gradient through a hydrated manose inter layer is compensated by the increase of interface roughness in a three slab model. From a structural point of view, the SLD of CF_2 units calculates from the real part of the atomic scattering factor f_1 of fluorine (9.075), and carbon (6.019) (Thompson et al., 2009), and a respective volume of $38\,\text{Å}^3$ (McIntosh et al., 1996) to be $17.9\,\text{Å}^{-2}$. Crystallographic X-ray data of fluorocarbon polymers predict a rigid, helical alignment of fluorocarbon chains (Bunn and Howells, 1954) and the presented high resolution GIXD data (Section 5.1) confirmed the closest packed, parallel ordering of chains. This tight crystalline arrangement even suggests higher values for the SLD of fluorocarbon chains. The presented best fit models yield a SLD of $18.7\,\text{Å}^{-2}$ for FL17, $19.7\,\text{Å}^{-2}$ for FL13, and $19.3\,\text{Å}^{-2}$ for FL10man. A similar range was fitted for unoriented lamellar samples (Oelke, 2008; Kaindl et al., 2010) with small angle X-ray scattering (SAXS). In comparison, Tidswell et al. (1990) found a scattering length of $80\,\%$ of ρ_{Si}, i.e, $16.1\,\text{Å}^{-2}$, for less dense packed perfluorinated alkylsiloxanes. In any case, a good fitting quality was only reached by consideration of an additional surface near the head group layer. Here, the SLD was fitted within a range of $10.0\,\text{Å}^{-2}$ to $13.7\,\text{Å}^{-2}$. This layer was attributed to the hydrated glycerol head group region of the lipids that are responsible for the hydrophilic adsorption of the monolayer onto the silicon substrate. The parameters obtained by the best fit are physically realistic and are displayed in Table 5.2. The obtained monolayer thickness is directly related to the molecular length of the fluorinated molecules, since GIXD experiments revealed a perpendicular orientation of the molecules with respect to the surface. In the following chapter, these results will be used to calculate the intermolecular line tension at the domain boundary for fluorinated lipids within ordinary alkyl–chain lipids.

5.3. Line Tension of Domains

In Section 4.2 it was shown that the line energy F_λ of lipid domains scales with the length l and the curvature of the phase boundary line. In fact, it is a molecular measure for intermolecular repulsion of neighboring molecules. Therefore, it must also scale with the monolayer thickness h, i.e., the length of interacting lipid chains. As presented by Hu et al. (2006), for binary mixtures of dimyristoyl-phosphatidylcholine (DMPC) and dihydrocholesterol (Dchol), the molecular height mismatch Δh of lipids across a monolayer contributes to the line tension λ as:

$$\lambda = \gamma \cdot \Delta h, \tag{5.11}$$

Table 5.2.: Best model fit parameters deduced from specular X-ray reflectivity curves for FL17, FL13, and FL10Man monolayers. The respective layer thickness h, scattering length density SLD, and interface roughness σ for a three slab box model. Parameters indicated by ^{c} were confined during the fit.

layer unit	h Å	SLD $Å^{-2}$	σ Å
FL17	20.6	18.7	3.3
head group	5.6	12.4	3.1
SiO_2	5.4	18.9^c	3.7
Si	-	20.9	2.3
FL13	15.8	19.7	2.4
head group	2.6	13.7	4.3
SiO_2	5.4	18.9^c	4.0
Si	-	20.6	2.0
FL10man	12.3	19.3	5.6
head group	4.5	10.0	7.3
SiO_2	6.8	18.9^c	4.3
Si	-	20.5	2.7

where γ is the surface free energy. For fluorinated lipids incorporated into a DOPC lipid matrix, the line tension can be written as:

$$\begin{aligned} \lambda &= \gamma(h_{\text{DOPC}} - h_{\text{FL}n}) + \Delta\gamma h_{\text{FL}n}, && h_{\text{FL}n} < h_{\text{DOPC}}, \\ \lambda &= \gamma(h_{\text{FL}n} - h_{\text{DOPC}}) + \Delta\gamma h_{\text{DOPC}}, && h_{\text{FL}n} > h_{\text{DOPC}}, \end{aligned} \tag{5.12}$$

where $\Delta\gamma$ refers to the difference in surface free energy between fluorocarbons and hydrocarbons. The surface free energy γ at the chain–air interface has been reported as $\gamma_{HC-air} = 19.3\,\text{mN}\,\text{m}^{-1}$ for a hydrocarbon/air, and $\gamma_{FL-air} = 9.5\,\text{mN}\,\text{m}^{-1}$ for a fluorocarbon/air interface (Chaudhury and Owen, 1993). The difference in hydrocarbon chain to fluorocarbon chain interaction calculates to $\gamma_{HC-FL} = 9.8\,\text{mN}\,\text{m}^{-1}$. The only missing parameter for an estimate of λ is the molecular length of lipids. Here, the X-ray reflectivity results previously presented in Section 5.2 provided the important material parameters to calculate the line tension for fluorinated lipids. Since grazing incidence X-ray experiments (Section 5.1) revealed no molecular tilt against the surface normal, the presented monolayer thickness h in Table 5.2 is directly related to the molecular chain length of fluorinated lipids. For DOPC, I used a literature value of $h_{\text{DOPC}} = 19.8\,\text{Å} \pm 0.2\,\text{Å}$ deduced from head- to head-group spacing of DOPC bilayers (Tristram-Nagle et al., 1998; Nováková et al., 2006). The resulting line tension values at a DOPC-FLn interface are presented in Table 5.3.

Table 5.3.: Calculated values of line tension at the DOPC-FLn interface for FL10, FL13, and FL17.

	unit	FL10	FL13	FL17
λ_{FLn}	pN	26.5	23.2	18.6

5.4. Surface Dipole Potential Measurements

Most lipid molecules carry oriented dipoles or even charged groups that are the origin of electrostatic potentials, the so-called surface potential. These electrostatic effects can be measured with a compensation potential of a vibrating plate electrometer. A macroscopic Kelvin probe gold electrode (diameter $\sim 6\,\mathrm{mm}$) was placed $\sim 1\,\mathrm{mm}$ away from the air-water interface of a metal coated film balance (µSpot mini trough from Kibron Inc., Espoo, Finland) that acts as a counter electrode. In electric contact, the vibrating plate causes a small alternating current flowing across the electrodes, which act as capacitor plates with a dielectric interlayer of air and water. The relative contact potential V of an interface is measured by applying a compensating DC potential to null the AC contact potential. When a lipid monolayer is interposed at the air-water interface, the absolute change in surface potential can be measured by $\Delta V = V_{monolayer} - V_{water}$. In this thesis, the surface potential change ΔV was stable within an error of $\pm 7\,\mathrm{mV}$. The surface potentials of a pure DOPC (black line) and FL13 (red line) were recorded during slow compression isotherms of the monolayers. The respective surface potentials and pressure-area isotherms (dashed lines) are plotted in Figure 5.5. The effective molecular dipole density difference $\Delta\mu$ was derived from the difference in surface potential ΔV, at a lateral surface pressure of $\Pi = 20\,\mathrm{mN\,m^{-1}}$. This surface pressure was employed during domain formation and LS monolayer transfer. For both molecules, ΔV values were derived at the corresponding molecular areas and are indicated by a circle in Figure 5.5. They yield $\Delta V = -553\,\mathrm{mV} \pm 7\,\mathrm{mV}$ for FL13 and $\Delta V = 338\,\mathrm{mV} \pm 7\,\mathrm{mV}$ for DOPC. The dipole potentials of pure FLn monolayers at $\Pi = 20\,\mathrm{mN\,m^{-1}}$ were found to be almost independent of chain length. To calculate the dipole moment μ projected to the direction normal to the surface, ΔV can be described by the Helmholz equation,

$$\Delta V = \frac{1}{\sqrt{2\pi\epsilon_{\text{eff}}}}\frac{\mu}{\epsilon_0}. \tag{5.13}$$

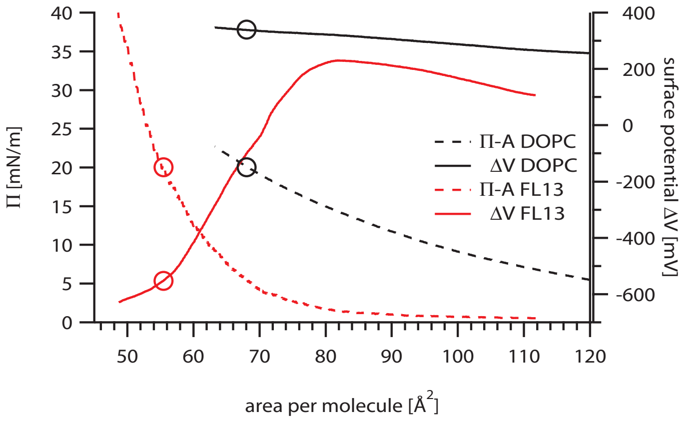

Figure 5.5.: Surface potential measurements (solid line) with respective Π-area plots (dashed lines) of DOPC (black) and FL13 (red) Langmuir compression isotherms. The conditions for a lateral surface pressure $\Pi = 20\,\mathrm{mN\,m^{-1}}$ are indicated by circles.

According to Equation 4.11, μ is the molecular dipole density, i.e., the dipole moment p per molecular area A_{mol}, and ϵ_{eff} is the effective dielectric constant felt by the lipid dipoles near the air-water interface. The quantitative interpretation of ϵ_{eff} is problematic (Möhwald, 1995, p. 168), since the dielectric constant increases across the interface from $\epsilon_A = 1$ for air to $\epsilon_W = 80$ for water. The monolayer at the asymmetric air-water interface can be interpreted as a dipolar sheet. "Real" dipoles at the lipid chain terminus create "image dipoles" in the subphase. The interaction energy between two real dipoles located just above the water interface is then proportional to $\epsilon_{\text{eff}} = \epsilon_W/(\epsilon_A(\epsilon_W + \epsilon_A))$ (Andelman et al., 1987). Dependent on the location of the dipoles within the molecule, the effective dielectric constant ϵ_{eff} varies. A general approach models the lipid monolayer as a series of three capacitors with contributing terms from (Brockman, 1994): (i) electrostatic contributions from a dipolar head group, (ii) influence of polarized water molecules enclosing the head group, and (iii) dipolar contributions from asymmetric chain terminal groups, i.e. CH_3 and CF_3. In this thesis, the fluorinated lipids are constituted of neutral glycerol backbones and a chain terminal CF_3 group oriented normal to the surface (Section 5.1). For all intermediate lipid chain regions, i.e. CH_2 and CF_2, the net molecular dipole moment does not contribute significantly to ΔV, since the successive *C-H* and *C-F* bonds lie perpendicular to the surface and compensate each other (Brockman, 1994; Mingins et al., 1992; Schneider et al., 2005). Thus, the major contribution of molecular dipole moment for fluorinated lipids arises from the electron accepting CF_3-terminal group. In fact, DOPC has a electron-donating CH_3-terminal group (Brockman, 1994) and has a dipole potential of opposite sign. Considering that all major dipolar contributions are located at the chain terminal air-facing side

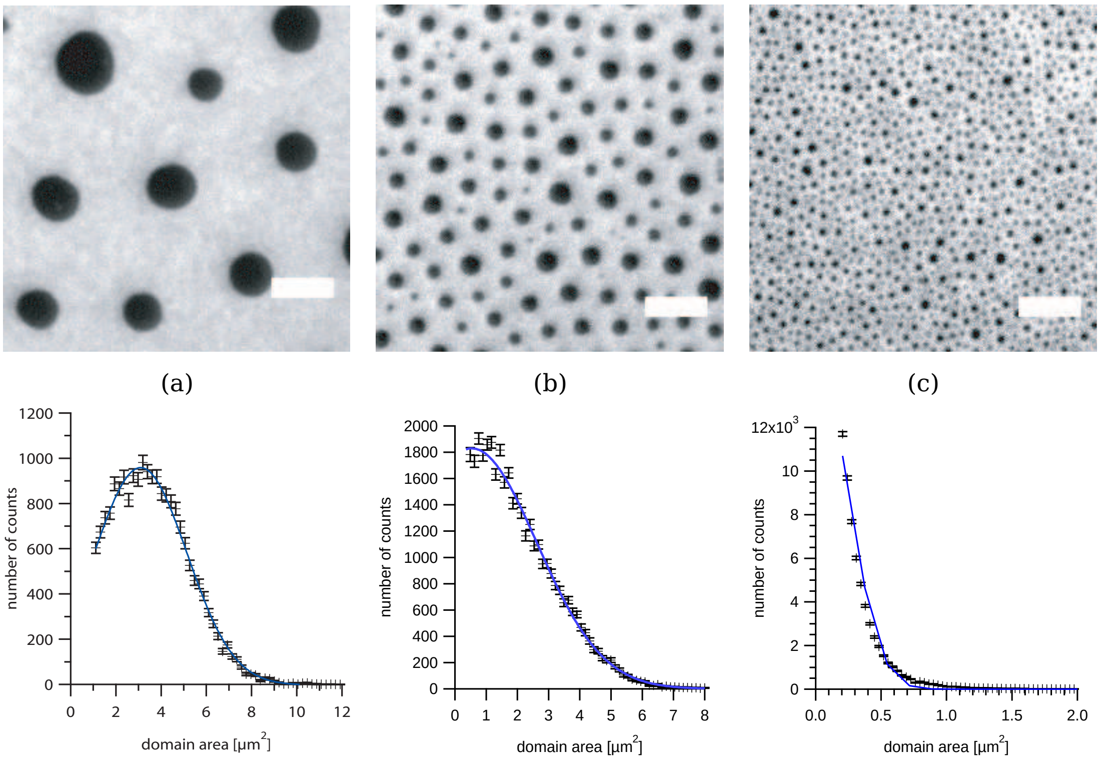

(a) (b) (c)

(d) (e) (f)

Figure 5.6.: Fluorescence images of $33\,\mathrm{mol\%}$ (a) FL10, (b) FL13, and (c) FL17 domains (black) in a $67\,\mathrm{mol\%}$ fluorophore-labeled DOPC matrix (bright). All scale bars correspond to $5\,\mathrm{\mu m}$. Panels (d-f) show histograms of the corresponding domain size distributions. A Gaussian fit is shown as blue line.

the effective permittivity for dipoles close to the water surface calculates as, ϵ_{eff} = 80/(1(80+1)). For fluorinated lipids and DOPC, the permittivity is rather low, which explains the high surface potential difference $\Delta V = -891\,\mathrm{mV} \pm 10\,\mathrm{mV}$. This yields a molecular electrostatic force of $\mu^2/4\pi\epsilon_0 = 3.4\,\mathrm{pN}$ for fluorinated domains.

5.5. Influence of Chain Length

From previous discussions it is evident that the line tension λ and the electrostatic force $\mu^2/4\pi\epsilon_0$ directly influence the size- distribution of domains. In this thesis, fluorinated lipids with variable chain length $h_{\mathrm{FL}n}$ were mixed into a DOPC matrix with unaltered length h_{DOPC} to modify the line tension λ of domains. The number of fluorinated carbons per chain was changed between $n = 10, 13$ and 17, whereas DOPC possesses a fixed number of 18 hydrocarbons per chain. All domains presented in this thesis were formed at a lateral surface pressure $\Pi = 20\,\mathrm{mN\,m^{-1}}$,

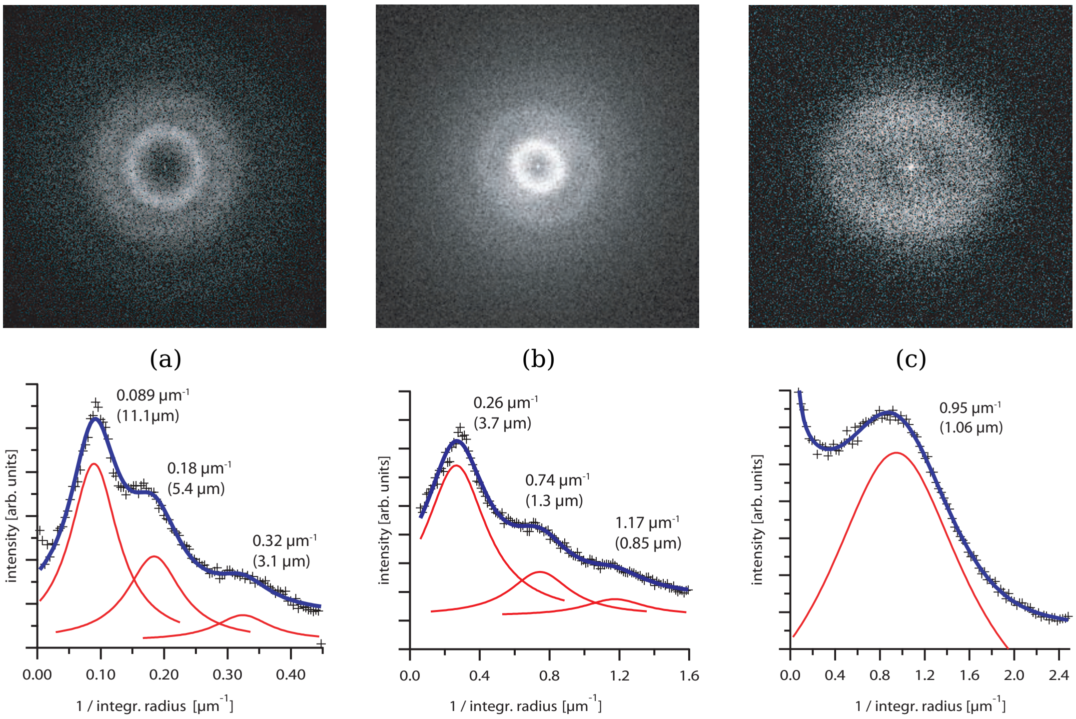

(a) (b) (c)

(d) (e) (f)

Figure 5.7.: 2-dimensional spectral density of more than 5000 domains for $33\,\mathrm{mol\%}$ mixture of (a) FL10, (b) FL13, and (c) FL17 in DOPC. Graphs (d-f) show radial integrations of the corresponding spectral density and overall fit curve (blue) for multiple Gaussian peaks (red lines with $-10\,\%$ offset).

where the molecular dipole density of pure FLn monolayers were found to be almost independent of chain length (Section 5.4). Figure 5.6 shows small cut–outs from fluorescence images of $33\,\mathrm{mol\%}$ (a) FL10, (b) FL13, and (c) FL17 domains (black) within $67\,\mathrm{mol\%}$ DOPC lipids that were doped with fluorescence marker molecules (bright). All monolayers containing FLn molecules show circular domains which are uniformly distributed over macroscopic dimensions, i.e., over several cm^2. The size of the domains clearly depends on the length of the fluorocarbon chains. Histograms of the domain size distribution (Figure 5.6 (d-f)) show a narrow Gaussian distribution (blue line). With increasing chain length, the mean domain area decreases from $\langle A_{\mathrm{FL10}} \rangle = 3.1\,\mathrm{\mu m}^2 \pm 0.1\,\mathrm{\mu m}^2$ for FL10, to $\langle A_{\mathrm{FL13}} \rangle = 0.6\,\mathrm{\mu m}^2 \pm 0.1\,\mathrm{\mu m}^2$ for FL13. A precise determination of the average FL17 domain size was not possible with image analysis, since the resolved domain size distribution (Figure 5.6f) did not include the absolute maximum position that is needed for a peak fit. The average size of domains is expected to lie below $\langle A_{\mathrm{FL17}} \rangle \leq 0.2\,\mathrm{\mu m}^2$ which is the size of a 4×4 pixel area used as minimum threshold size for the image particle detection

Figure 5.8.: Shape distortions of FL10 domains with typical diameters larger than $e^{\frac{1}{3}}R_{eq}$. All scale bars correspond to $5\,\mu\text{m}$.

routine. Since the average size of FL17 domains goes below the optical resolution of fluorescence microscopy, high–resolution GIXD measurements with an analyzer crystal setup were carried out (Section 5.1).

To elucidate the predominant spatial length scales between domains, the inter–domain correlations of more than 5000 domains were quantitatively evaluated. At first, the spectral density $\theta(k,l)$ was calculated as square of the magnitude of the two–dimensional Fourier transform in space,

$$\theta(k,l) = \left| \frac{1}{2\pi} \int_{-\infty}^{\infty} f(x,y) \exp^{-i(kx+ly)} \, dxdy \right|^2 = \frac{F(k,l)F^*(k,l)}{4\pi^2}. \tag{5.14}$$

where k and l denote the reciprocal wave vectors and $F(k,l)$ the continuous Fourier transform and its complex conjugate $F^*(k,l)$. The spectral density for FL10 and FL13 domains are presented in Figure 5.7(a–b), where three concentric rings are visible. The spectral density for FL17 (Figure 5.7c) shows only one broad halo. Radial integration (black data points) and subsequent Gaussian multi peak fitting (red lines with $-10\,\%$ offset) resulted in the characteristic length scales as presented in Figure 5.7 (d–f). The overall fit of the spectral density is indicated as a blue line. For all three graphs, the most intense peak is attributed to the inter–domain distance $a_{\text{FL}n}$. FL10 yields a lattice constant of $a_{\text{FL10}} = 11.1\,\mu\text{m} \pm 0.1\,\mu\text{m}$, FL13 of $a_{\text{FL13}} = 3.77\,\mu\text{m} \pm 0.03\,\mu\text{m}$, and FL17 of $a_{\text{FL17}} = 1.1\,\mu\text{m} \pm 0.1\,\mu\text{m}$.

Radial integration of the spectral density showed two additional maxima for FL10 and FL13. They were attributed to different populations of domain diameters. For FL10, maxima were fitted for $d_1 = 5.4\,\mu\text{m} \pm 0.1\,\mu\text{m}$ and $d_2 = 3.1\,\mu\text{m} \pm 0.1\,\mu\text{m}$. A closer look on domains with diameters around d_1 revealed shape fluctuations to higher harmonic orders. Figure 5.8 shows a selection of such large FL10 domains. As discussed in Section 4.6, large domains can stabilize in a broad size distribution which undergo shape transition to higher order for $R \geq e^{\frac{1}{3}R_{eq}}$. This means that the equilibrium radius is smaller than $R_{eq} < \frac{d_1}{2e^{1/3}} = 1.93\,\mu\text{m} \pm 0.04\,\mu\text{m}$. The same discussion holds for FL13 domains, where the spectral density showed maxima around $d_1 = 1.34\,\mu\text{m} \pm 0.02\,\mu\text{m}$ and $d_2 = 0.8\,\mu\text{m} \pm 0.3\,\mu\text{m}$. This limits the equilibrium radius below $R_{eq} < \frac{d_1}{2e^{1/3}} = \ 0.48\,\mu\text{m} \pm 0.01\,\mu\text{m}$.

Inverse Fourier transformation of the spectral density yields the autocorrelation pictures of domains in real space. They are presented in Figure 5.9(a–c) and show

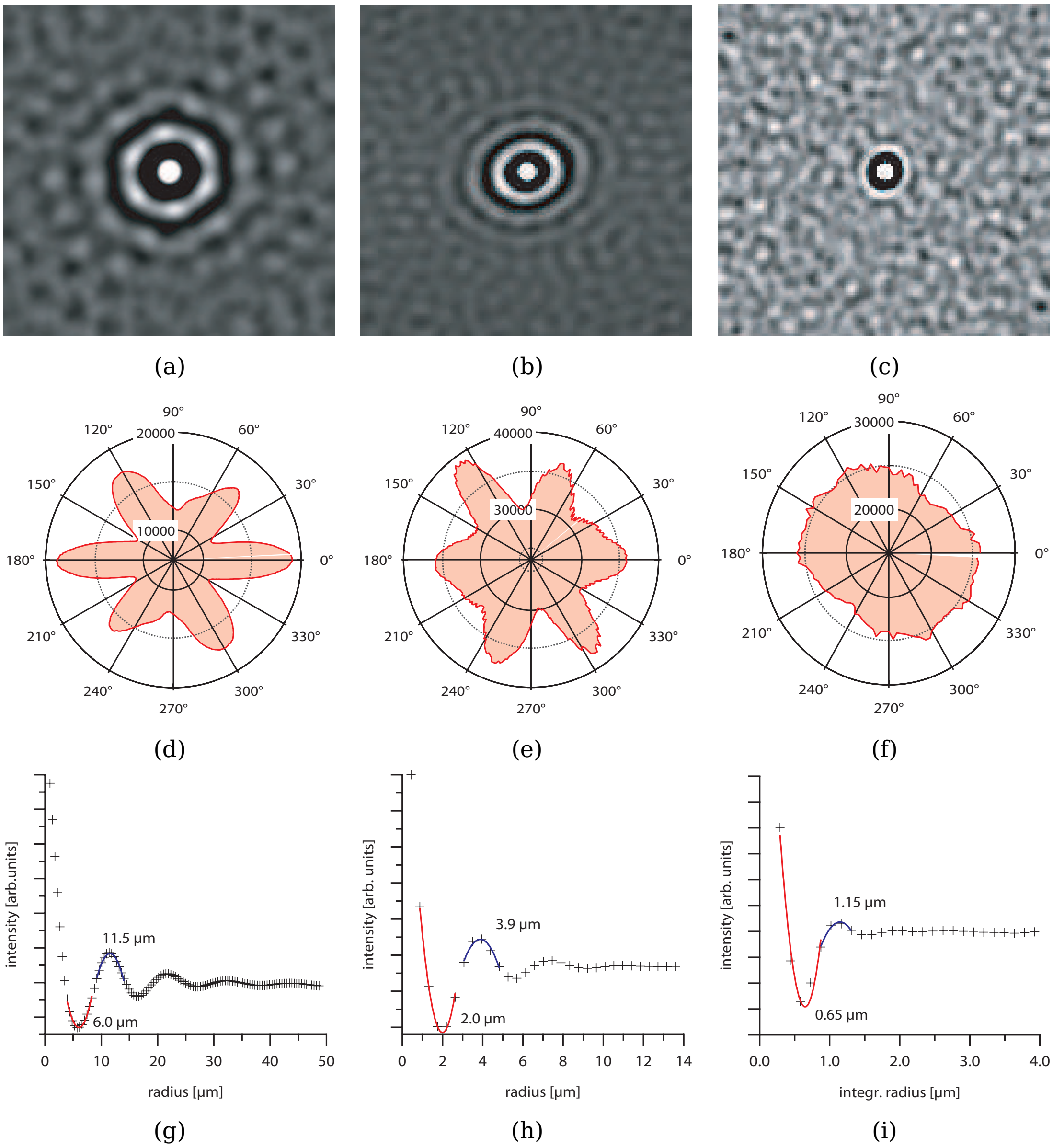

Figure 5.9.: Autocorrelation images of 33 mol% (a) FL10, (b) FL13, and (c) FL17 domains in a 67 mol% DOPC matrix. Graphs (d-f) show intensities at the first maximum contour line to highlight the number of symmetry. Graphs (g-i) show radial integrated intensities (black curve) and parabolic fits of the first minimum (red) and maximum positions (blue).

.

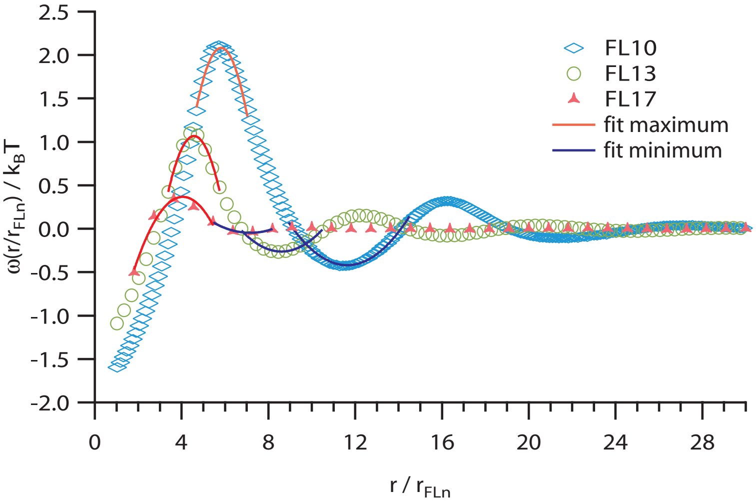

Figure 5.10.: Potentials of mean force calculated for FL10, FL13, and FL17.

a strong central peak which replicates the self consistency of a picture. A ring with maximum intensity around the center indicates spatial positions where self–similarity occurs. All three pictures show at least one minimum (black ring) and maximum (bright ring) where domains are depleted or respectively enriched. To highlight to azimuthal correlation of domains, the intensity of the first maximum position is shown along a $360°$ line profile in Figure 5.9(d–f). FL10 and FL13 domains display a slightly distorted 6-fold symmetry. The lattice unit vectors a_1 and a_2 span approximately over $60°$, a feature that is striking for a hexagonal arrangement of domains. For FL17 domains, only one pronounced minimum was observed which indicates a missing long-range correlation of domains. To quantitatively evaluate the strength of inter-domain correlations the radial distribution function $g(r)$,

$$g(r) = \frac{dN(r+\Delta r)}{dA(r+\Delta r)} \frac{N}{A}, \tag{5.15}$$

was derived. Similar to the discrete two-dimensional sum in Equation 4.20, this function modulates the interaction strength of domains arranged in laterally confined structures. (Figure 5.9 (g–i)) presents the radial density distribution $g(r)$ of domains derived from radial integrations around the central peak of the respective autocorrelation images. FL10 domains revealed a high lateral correlation of domains with maxima up to the $4th$ neighbor position (Figure 5.9g). With increasing domain distance, the long range correlation diminishes and $g(r)$ levels to the average number density of domains (Equation 4.25). The previously reported lattice constant a of $11.5\,\mu\text{m}$ for FL10, $3.9\,\mu\text{m}$ for FL13, and $1.1\,\mu\text{m}$ for FL17 was confirmed for all fluorinated lipids. The pronounced lateral confinement of FL10 domains suggested a comparison with a system of two-dimensional colloidal crystallization. Within the framework of the inverse work theorem, $g(r)$ can be related to the so–called potential of mean force $\omega(r)$ (Quesada-Pérez et al., 2002):

$$-\frac{\omega(r)}{k_B T} \propto ln\left[g(r)\right]. \tag{5.16}$$

Figure 5.10 presents the calculated potential of mean force $\omega(r/r_{\mathrm{FL}n})$ for $33\,\mathrm{mol\%}$ FL10, FL13, and FL17 domains. Note that the distance between domains is normalized for the respective domain radius $r_{\mathrm{FL}n}$. At the first maximum position of $\omega(r/r_{\mathrm{FL}n})$, i.e., where domains are depleted, a repulsive potential of mean force was fitted with a harmonic spring constant of $k^{\mathrm{max}}_{\mathrm{FL10}} = -0.54$, $k^{\mathrm{max}}_{\mathrm{FL13}} = -0.45$, and $k^{\mathrm{max}}_{\mathrm{FL17}} = -0.16$. With decreasing long range correlation of domains, a decrease in $k^{\mathrm{max}}_{\mathrm{FL}n}$ was observed. The confinement of the nearest domain position revealed a harmonic spring constant of $k^{\mathrm{min}}_{\mathrm{FL10}} = 0.067$, $k^{\mathrm{min}}_{\mathrm{FL13}} = 0.071$, and $k^{\mathrm{min}}_{\mathrm{FL17}} = 0.04$. Since the long range correlation reaches up to distances that are several times larger than the domain size, the presented potential of mean force includes many-body interactions and must be regarded as an effective interaction potential of domains. All obtained structure parameters of FL10, FL13, and FL17 domains are summarized in Table 5.4.

Table 5.4.: Experimentally found values for the average domain radius area$_{av}$, the calculated domain radius R_{area}, the inter-domain distance a, and the domain characteristic length scales d_1, d_2 with an expected maximum equilibrium radius R_max for FL10, FL13, and FL17 domains. $k^{\mathrm{max}}_{\mathrm{FL}n}$ and $k^{\mathrm{min}}_{\mathrm{FL}n}$ denote spring constants from the first maximum and minimum position of the potential of mean force.

	unit	FL10	FL13	FL17
$\langle A_{\mathrm{FL}n}\rangle$	µm^2	3.1 ± 0.1	0.6 ± 0.1	< 0.2
R_{area}	µm	0.99 ± 0.02	0.43 ± 0.04	< 0.25
$a_{\mathrm{FL}n}$	µm	11.1 ± 0.1	3.77 ± 0.03	1.1 ± 0.1
d_1	µm	5.4 ± 0.1	1.34 ± 0.02	-
d_2	µm	3.1 ± 0.1	0.8 ± 0.3	-
R_{max}	µm	$< 1.93 \pm 0.04$	$< 0.48 \pm 0.01$	-
$k^{\mathrm{max}}_{\mathrm{FL}n}$		-0.54	-0.45	-0.16
$k^{\mathrm{min}}_{\mathrm{FL}n}$		0.067	0.071	0.04

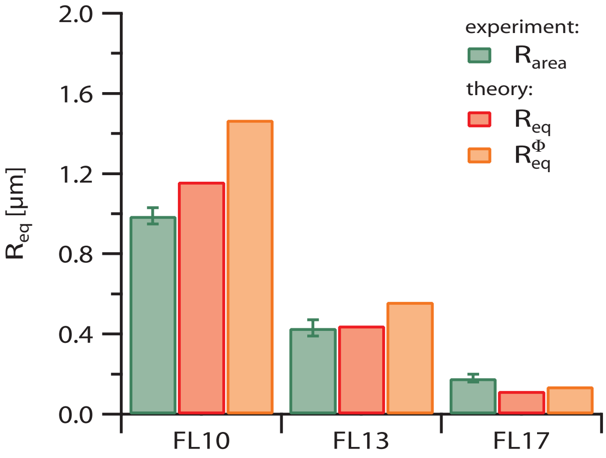

Figure 5.11.: Comparison between the experimental equilibrium radius R_{area}, the theoretical equilibrium radius R_{eq} of a single domain, and the equilibrium radius R_{eq}^{Φ} for laterally correlated domains of fluorinated lipids with different chain lengths.

.

5.6. Comparison to Theoretical Model

The theoretical equilibrium radius of domains is derived in Chapter 4 within the theoretical framework of the equivalent dipole model. Here, it can be quantitatively calculated (Equation 4.24) due to the precise determination of all molecular parameters of fluorinated lipid domains. For the calculation of the electrostatic energy F_{el} in Equation 4.10, a molecular cut-off parameter Δ was introduced. Δ can be estimated by the smallest molecular inter-chain distance d^{mol} of lipids. The obtained results from GIXD measurements are presented in Table 5.1. A quantitative estimate of the effective line tension F_{λ} surrounding the domains was presented in Table 5.3. There, the length mismatch δh between fluorocarbon- and alky-lipid chains was determined by specular X-ray reflectivity measurements, which allowed for calculation of F_{λ}. Furthermore, the surface dipole potential difference ΔV between fluorinated lipids and DOPC monolayers was measured in Section 5.4 and resulted in a molecular electrostatic repulsion force of $\mu^2/4\pi\epsilon_0 = 3.4\,\mathrm{pN}$. Entering these parameters into Equation 4.15 yields the theoretical equilibrium domain radius R_{eq} for a single isolated domain. For $33\,\mathrm{mol\%}$ fluorinated lipid domains in DOPC R_{eq} calculates to $1.16\,\mathrm{\mu m}$ for FL10, to $0.44\,\mathrm{\mu m}$ for FL13, and $0.12\,\mathrm{\mu m}$ for FL17. Figure 5.11 shows a comparison between the experimental deduced radius R_{area} (Table 5.4) and the theoretically calculated values R_{eq}. It demonstrates excellent agreement between R_{area} and R_{eq} for both the decreasing tendency of R_{eq} with increasing fluorocarbon chain length of the molecules and the absolute values of R_{eq}. Furthermore, the influence of inter-domain potential on the theoretical size of R_{eq}

was discussed in Section 4.7. For diluted systems, the interaction energy of domains causes an increase of the equilibrium radius by a factor of $e^{1.24\Phi^{3/2}}$ (Equation 4.24), where Φ is the area fraction of domains. A comparison of R_{eq}^{Φ} in Figure 5.11 with the experimentally found R_{area} shows still good agreement for FL13 and FL17 domains, but overestimates the size of FL10 domains considerably. For the calculation of R_{eq}^{Φ}, the material parameter $m = (4\pi\epsilon_0\lambda)/(\mu^2)$ enters exponentially. This implies that the calculation of R_{eq}^{Φ} for FL10 either overestimates the surface free energy γ (Equation 5.11) or underrates the dipole density μ. μ enters reciprocal to m and revealed already high values for fluorinated lipids. Since all molecular structure parameters were precisely measured, a further refinement of γ for single domains is suggested. The overall tendency in of the equilibrium radius R_{eq} in Figure 5.11 and the good agreement with experimental values enable a close prediction R_{area} for other fluorinated lipids.

Table 5.5.: Theoretical values for the equilibrium radius of isolated R_{eq}, and of interacting R_{eq}^{Φ} domains at an area fraction $\Phi = 0.33$ of domains.

	unit	FL10	FL13	FL17
R_{eq}	µm	1.16	0.44	0.12
R_{eq}^{Φ}	µm	1.47	0.56	0.14

5.7. Functional Lipid Domains

An objective of this thesis is the use of supported membranes with embedded domains as a model system for lipid rafts in plasma membranes. Therefore, fluorinated lipids with modified head group functionality were synthesized. In the following, the domain formation of two types of functional fluorinated lipids is discussed.

5.7.1. Direct Carbohydrate Coupling

In order to regulate the adhesion behavior of cells on carbohydrate exposing domains, a simple α-D-mannose monosaccharide was directly coupled to the head group of FL10Man lipids. Experiments of the adhesion behavior of macrophages on FL10Man domains are further discussed in Section 6.3. In the following the lateral confinement of FL10Man domains is discussed. Figure 5.12a presents fluorescence pictures of of $33\,\mathrm{mol\%}$ FL10Man lipids mixed within $67\,\mathrm{mol\%}$ DOPC lipids at a lateral surface pressure of $20\,\mathrm{mN\,m^{-1}}$. In comparison to FL10 lipids without head group modification (Figure 5.6a), the average domain area of FL10Man decreases by a factor of 2.4 to $R_{\mathrm{area}} = 1.30\,\mathrm{\mu m^2} \pm 0.02\,\mathrm{\mu m^2}$. This yields an average domain

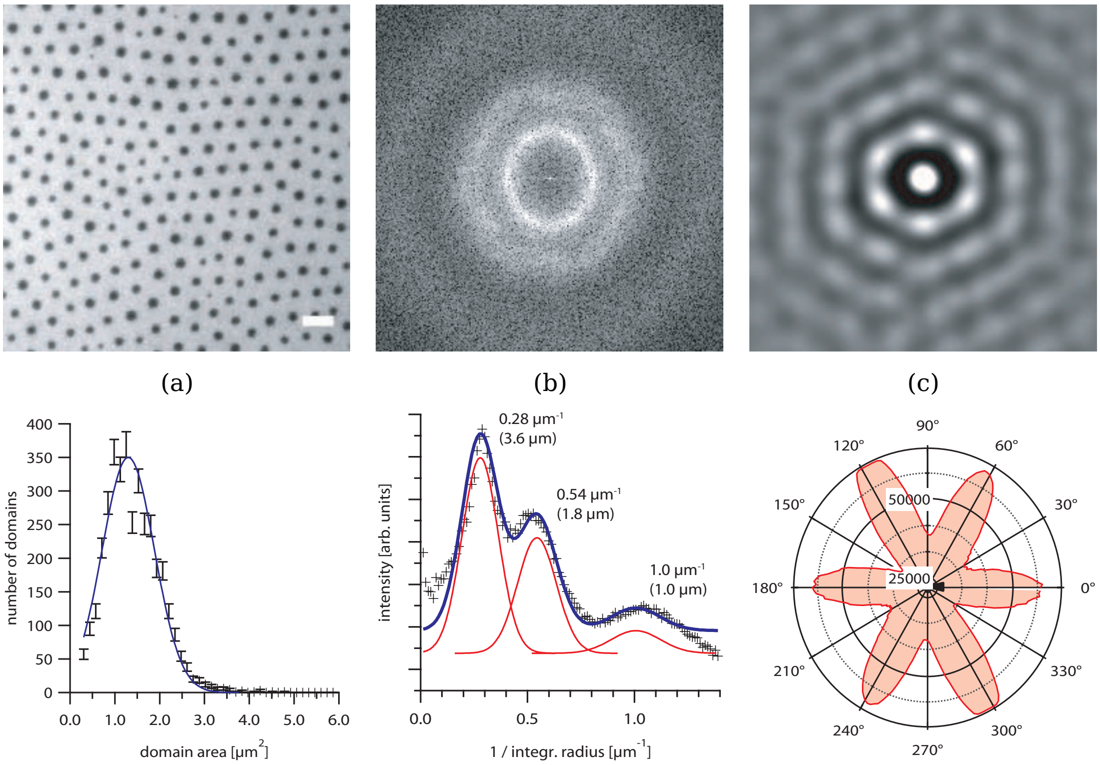

(a) (b) (c)

(d) (e) (f)

Figure 5.12.: (a) Fluorescence image of $33\,\mathrm{mol\%}$ FL10Man domains, (b) spectral density, (c) autocorrelation, (d) domain area histogram, (e) multi Gaussian fit on radial spectral density, and (f) polar intensity plot of nearest neighbor radius. The scale bar is $5\,\mathrm{\mu m}$.

.

Table 5.6.: Experimentally found values for the average domain radius area$_{av}$, the calculated domain radius R_{area}, the inter-domain distance a, and the domain characteristic length scales d_1, d_2 with an expected maximum equilibrium radius R_max for FL10Man domains. $k^{\max}_{\mathrm{FL}n}$ and $k^{\min}_{\mathrm{FL}n}$ denote spring constants from the first maximum and minimum position of the potential of mean force.

	unit	FL10Man
$\langle A_{\mathrm{FL10Man}} \rangle$	µm^2	1.30 ± 0.02
R_{area}	µm	0.64 ± 0.05
a	µm	3.60 ± 0.05
d_1	µm	1.85 ± 0.03
d_2	µm	1.0 ± 0.1
R_{max}	µm	< 0.66
$k^{\max}_{\mathrm{FL10Man}}$		-4.3 ± 0.6
$k^{\min}_{\mathrm{FL10Man}}$		0.38 ± 0.01

radius of $R_{area} = 0.64 \pm 0.05$. Figure 5.12d presents the corresponding histogram of the domain size distribution with a Gaussian fit (blue line). The spectral density and its radial integration (Figure 5.12(b, e)) revealed three distinct length scales for the inter-domain distance $a = 3.60\,\mu\mathrm{m} \pm 0.05\,\mu\mathrm{m}$ and at $d_1 = 1.85\,\mu\mathrm{m} \pm 0.03\,\mu\mathrm{m}$ and $d_2 = 1.0\,\mu\mathrm{m} \pm 0.1\,\mu\mathrm{m}$. The good spatial confinement of domains is also visible in autocorrelation images with distinct intensity maxima (Figure 5.12c). The radial intensity profile line of the around the first neighbor domain distance is presented in Figure 5.12f and shows a clear 6-fold azimuthal symmetry for FL10Man domains. Striking for FL10Man domains is the long ranging inter-domain correlation of domains which shows pronounced maxima for $g(r)$ up to the 6*th* neighbor position. Using the inverse work theorem (Equation 5.16) for the normalized radial density distribution $g(r)$ yields the effective potential of mean force for domains (Figure 5.13). A parabolic fit on the first maximum and minimum position yielded a spring constant of $k^{\max}_{\mathrm{FL10Man}} = -4.3 \pm 0.6$ and $k^{\min}_{\mathrm{FL10Man}} = 0.38 \pm 0.01$. The results clearly state, that the lateral confinement of mannosylated domains became stronger compared to head group unmodified FL10 lipids, which can be characterized by a larger spring constant. Although X-ray experiments revealed no changes in the molecular orientation (Section 5.1), a distinct influence of the mannose head group was observed due to the reduced size of FL10Man domains.

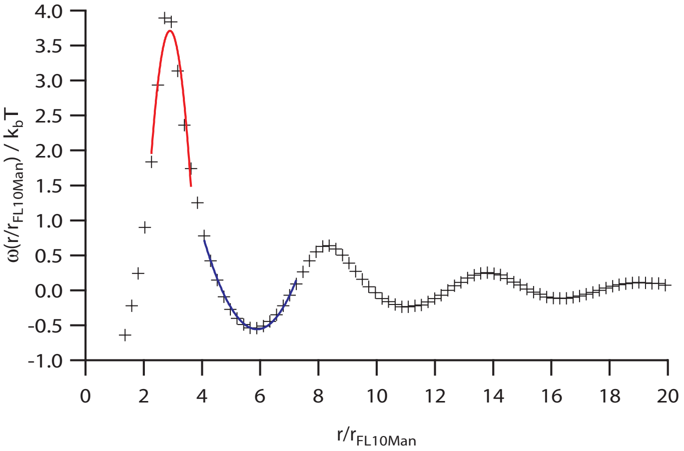

Figure 5.13.: Potentials of mean force calculated for FL10Man.

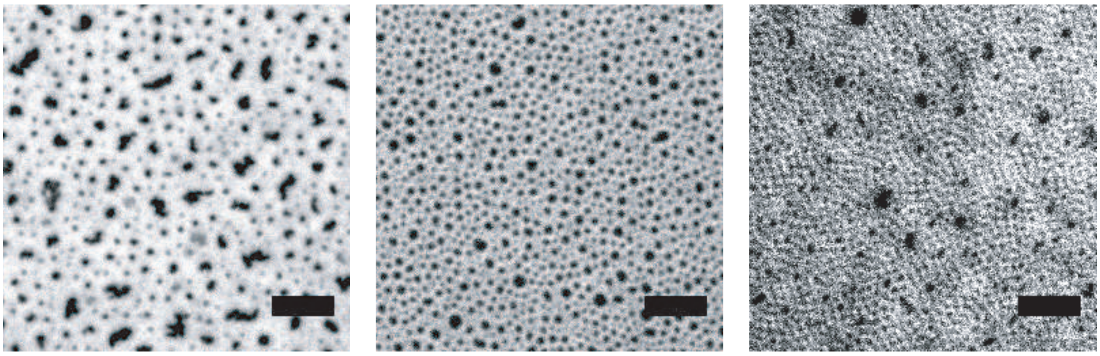

(a) (b) (c)

Figure 5.14.: Fluorescence images of $33\,\mathrm{mol\%}$ (a) hFL17, (b) acFL17, and (c) btnFL17 domains in $67\,\mathrm{mol\%}$ DOPC at $20\,\mathrm{mN\,m^{-1}}$. All scale bars are $5\,\mathrm{\mu m}$.

.

5.7.2. Variable Ligand Coupling

To study the specific cell response on membranes displaying laterally confined domains of membrane-associated proteins, fluorinated lipids were provided with a more variable coupling group. Therefore, fluorocarbon chains were connected via a beta glutamic acid backbone (hFL17) exposing a free amine group for further head group modifications. Compared to FL17 molecules, hFL17 adapts to natural natural lipids via its carbonyl side groups. Figure 5.14a shows epifluorescence pictures of $33\,\mathrm{mol\%}$ hFL17 domains within $67\,\mathrm{mol\%}$ DOPC lipids. The domains were polydispersive and larger domains highly irregular in shape. The previous discussions explained this effect by dominating electrostatic contributions or a reduced line tension. Frequent originators of such processes are contaminations that enrich at the phase boundary lines. Even small traces of impurities or residues of imperfect synthesis may cause these results. However, compression isotherms (Section 3.2) showed similar slopes as FL10 molecules and did not reveal significant signs of contaminations. To exclude interactions of amines for this effect, hFL17 molecules were acetylated at their amine groups and were further purified to acFL17 molecules by Christian Gege (University of Heidelberg, Germany). The epifluoresence picture of $33\,\mathrm{mol\%}$ acFL17 lipids within a DOPC matrix is shown in Figure 5.14b. The domains still show a broader sized distribution distribution than FL17 with larger mean size of $0.32\,\mathrm{\mu m}^2 \pm 0.01\,\mathrm{\mu m}^2$, but elongated and branched domain structures as seen for hFL17 were almost fully suppressed. These results allowed for an extension of the spacer molecule by an aminohexanoic acid spacer terminated with a biotin molecule (btnFL17). The spacer molecule provides more free moving space for coupled target molecules, whereas the biotin tag facilitates a variable and strong coupling of target molecules. This may provide a better steric access for binding sites on ligand molecules. Figure 5.14c shows the fluorescence picture of $33\,\mathrm{mol\%}$ btnFL17 lipids within a $67\,\mathrm{mol\%}$ DOPC and traces of TexasRed®-DHPE. A regular pattern of small dark domains was identified, although fluorescent tracer lipids were not homogeneously distributed. This limits a clear assignment of domains to the optical resolution of the microscope.

5.7.3. Mixing Behaviour of Functional Lipids

The presented ligand coupling strategy uses a biochemical well-proven biotin-avidin linker bridge (McMahon, 2008) as flexible molecular building blocks. That is, biotinylated anchor lipids (btnFL17) were incorporated into supported membranes and further functionalized with biotinylated ligand molecules. Neutravidin acted as As molecular linker, which provided a pair of biotin binding pockets on two opposing sides of the molecule. Details on the preparation protocol can be found in Section 2.12. Since the cross sectional area of Neutravidin is approximately 60 times larger than that of a single lipid molecule ($\approx 60\,\mathrm{\AA}^2$), concentrations of $5\,\mathrm{mol\%}$ biotinylated btnFL17 anchor molecules within lipid membranes guarantee a complete surface coverage of biotin-avdin linker bridges. This condition was preferred for cell experiments. A lower molar concentrations of btnFL17 lipids resulted in membranes of homogeneous dispersed ligand molecules, that are further discussed in Section 7.2. All pictures of Figure 5.15 show mixtures of $33\,\mathrm{mol\%}$ fluorinated lipids within $67\,\mathrm{mol\%}$ DOPC lipids. The fluorinated lipids are composed of $5\,\mathrm{mol\%}$ btnFL17 and $95\,\mathrm{mol\%}$ of FL10 (M5btnFL10), FL13 (M5btnFL13), and FL17 (M5btnFL17) lipids and are shown in Figure 5.15(a-c). It should be noted that no additional fluorescence tracer lipid was added, but btnFL17 enriched areas were visualized by coupling of TexasRed labeled Neutravidin. Therefore, domains appear inverted in brightness to formerly presented images. A dark area fraction of around $30\,\%$ in Figure 5.15a suggests, that FL10 phase separates from biotinylated

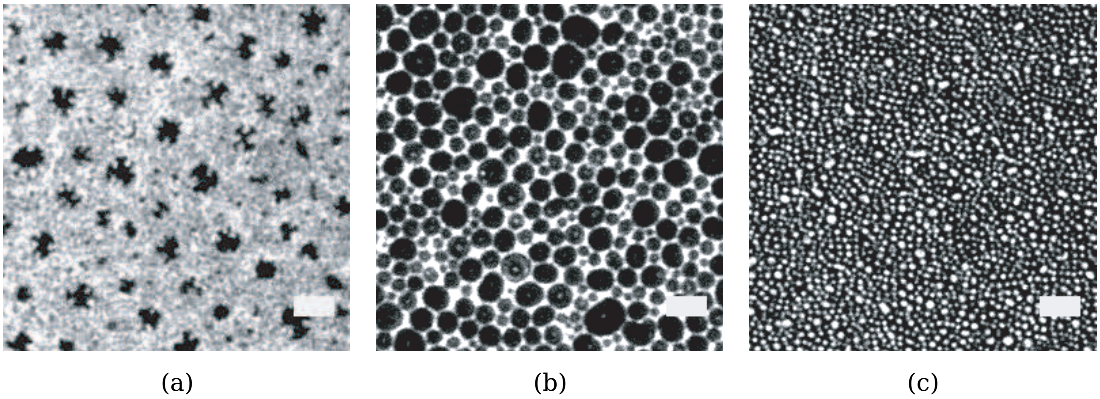

(a) (b) (c)

Figure 5.15.: Fluorescence images of biotinylated lipids btnFL17 in $31\,\mathrm{mol\%}$ (a) FL10, (b) FL13, and (c) FL17 and $67\,\mathrm{mol\%}$ DOPC. All scale bars are $5\,\mathrm{\mu m}$
.

btnFL17 (bright) and DOPC. A low concentration of btnFL17 in combination with the limiting optical resolution obviates conclusions on btnFL17 substructures within the DOPC matrix. Compared to Figure 5.6a, the jagged FL10 domain boundaries and the speckled fluorescence marker distribution rather suggest an inhomogeneous distribution. The situation changes in Figure 5.15b, where a dark area fraction of around $67\,\%$ can be attributed to DOPC lipids. Here, labeled btnFL17 molecules accumulated with FL13 lipids in inverted domain phases. Deformations of DOPC domains and trapped fluorescent domains cause additional contributions to the total free energy and make further estimates on domain size distributions erroneous. For mixtures with identical lipid chain length, that is btnFL17 in FL17, the same domain patterns as for FL17 binary mixtures were observed (Figure 5.6c). A dark area fraction of around $66\,\%$ matches with the used concentration of DOPC lipids. The average domain size of $0.2\,\mathrm{\mu m}^2$ agrees with previous results of FL17. In summary, the mixture M5btnFL17 was chosen as an appropriate model system to study cellular interaction on functional domains.

5.8. Regulation of Domain Density

The number density n (Equation 4.24) of functional domains depends on the area fraction Φ (Equation 4.21) of fluorinated lipids within the lipid mixture. In Figure 5.16 (a–c) fluorinated lipid domains of M5btnFL17 (i.e. $5\,\mathrm{mol\%}$:$95\,\mathrm{mol\%}$ btnFL17:FL17) are mixed with different area fractions Φ into a DOPC matrix. The molar content of M5btnFL17 increases from (a) $5\,\mathrm{mol\%}$, (b) $10\,\mathrm{mol\%}$, to (c) $33\,\mathrm{mol\%}$. Here, domains are labeled with Neutravidin-TexasRed and appear bright, whereas the DOPC matrix remains black. The use of an oil immersion objective with higher N.A. and the inverted labeling of domains resulted in an improved resolution for domain size de-

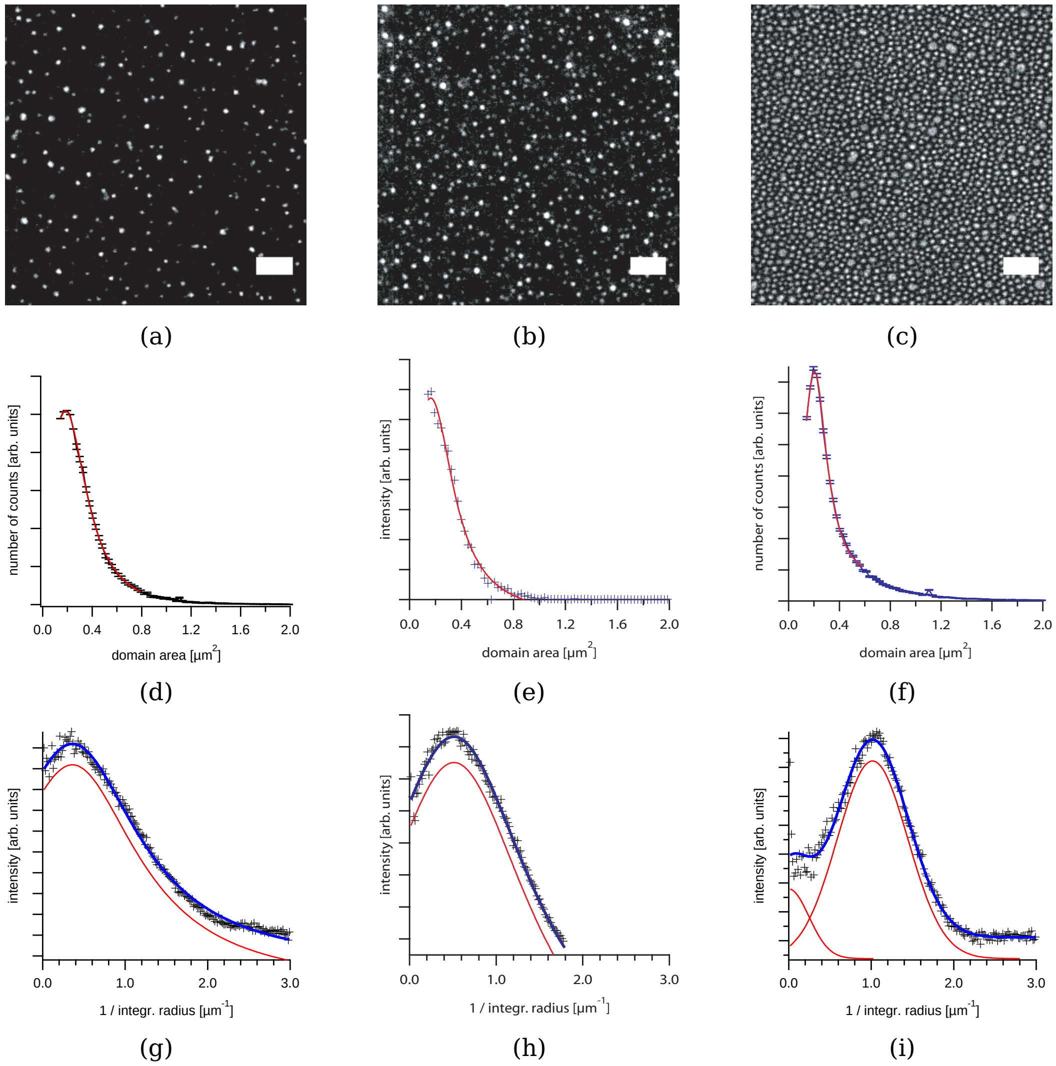

Figure 5.16.: Functional M5btnFL17 lipid domains of (a) 5 mol%, (b) 10 mol%, and (c) 5 mol% within remaining DOPC fraction. Domains are labeled with Neutravidin®-TexasRed® and appear bright. All scale bars are 5 µm. (d–f) Histograms of respective mixtures fitted with Gaussian line shape (red line). Graphs (g–i) show radial integrations of the corresponding spectral density and an overall fit curve (blue) for multiple Gaussian peaks (red lines with −10 % offset.

.

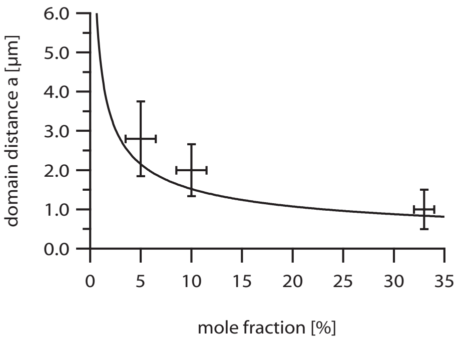

Figure 5.17.: Measured domain distance a for diluted concentrations of M5btnFL17 mixtures compared to theory (solid line).

.

tection. Figure 5.16(d–f) shows histograms of the domain sizes with a Gaussian fit (red line) of the maximum position that reveal a stable average domain area of $0.18\,\mu\mathrm{m}^2 \pm 0.03\,\mu\mathrm{m}^2$. This is consistent with the previously found domain areas around $0.2\,\mu\mathrm{m}^2$ for FL17 and btnFL17. The spectral density distribution for $5\,\mathrm{mol}\%$ and $10\,\mathrm{mol}\%$ M5btn17 domains showed only one halo. In account of its dimension, this peak must be attributed to the inter-domain distance a. Radial integration and subsequent Gaussian fitting (blue line) in Figure 5.16i(g–i) yielded an inter-domain distance $a = 2.8\,\mu\mathrm{m} \pm 0.9\,\mu\mathrm{m}$ for $5\,\mathrm{mol}\%$, $2.0\,\mu\mathrm{m} \pm 0.7\,\mu\mathrm{m}$ for $10\,\mathrm{mol}\%$, and $1.0\,\mu\mathrm{m} \pm 0.5\,\mu\mathrm{m}$ for $33\,\mathrm{mol}\%$ M5btn17 domains. Figure 5.17 presents a plot of the inter-domain distance a plotted for the concentration of fluorinated M5btn17 domains. The error bars for the concentration arise from mixing uncertainties of the fluorinated lipid solutions. As described by Wurlitzer et al. (2002) and McConnell (1986), for diluted systems ($\Phi < 0.35$) the equilibrium domain radius R_{eq} does not depend crucially on its area fraction Φ. This is consistent with the observed domain sizes of M5btnFL17 mixtures that yields a stable equilibrium radius of $R_{area} = 0.24\,\mu\mathrm{m} \pm 0.02\,\mu\mathrm{m}$. The solid line in Figure 5.17 represents the theoretical inter-domain distance a of diluted domain mixtures with a fixed domain radius R_{area}. The obtained results demonstrate that the inter-domain distance a of fluorinated domains can be quantitatively regulated proportional to $1/\phi^2$, where ϕ is the area fraction of domains.

6. Response of Macrophages on Carbohydrate-Domains

This chapter describes the effect of supported membranes displaying mannosylated domains (Subsection 5.7.1) on the cellular response of mouse macrophages. At first, the biological relevance of the selected ligand (mannose) and receptor (macrophage mannose receptor) molecules are explained. To allow for a quantitative data interpretation, the instrumental setup and the subsequent digital data analysis routines are discussed. Results are presented together with representative cell images which enables a conclusive discussion of the observed cell response.

6.1. Biological Role of Ligand–Receptor System

Plasma membranes of cells are postulated to form laterally organized domains, often referred as lipid rafts (Edidin, 2003). Lipid rafts can accumulate and bind a variety of proteins, glycoproteins or glycolipids which are involved in complex cellular functions, such as cell adhesion, signal transduction and endocytic trafficking (Simons and Ikonen, 1997; Hakomori and Igarashi, 1995). The fluorinated lipid domains presented in this study provide an excellent model system for such laterally confined membrane complexes. The multivalent carbohydrate interaction of cells was mimicked by FL10Man micro-domains exposing a directly coupled α-D-mannose monomer (Subsection 5.7.1). The mannose moiety acts as ligand molecule for a subgroup of cellular recognition receptors, called lectines. Lectines are involved in a broad variety of cellular interactions and play an important role in the response of immune cells.

6.1.1. Lectines

Lectins are binding proteins that are involved in the early stage of cell adhesion. They bind to carbohydrate structural epitopes, i.e., the binding site or determinant of the antigen, without modifying them. Lectins are of non–immune origin and agglutinate with high affinity for mannose and complex N–glycans (Nilsson, 2007, p. 2) to glycoconjugates of the extracellular matrix. Their classifications distinguish between biological functions, like

- membrane mediated microbial adhesion or hemmaglutionation,

- intracellular protein trafficking,
- lymphocyte homing and cell–cell recognition
  (e.g. gram–negative bacteria, HIV, H5N1),
- secretion as highly potent exotoxins
  (e.g. plant lectines like ricin, snake venom),

or between the binding affinity, where

- L–type binds to lymph nodes,
- E–type binds to endothelium cells, and
- P–type binds to activated blood platelets,

or between the structural appearance, like

- C–type lectins which depend on divalent ions (like calcium or manganese),
- I–type selectins which are defined by the overall structural similarity to immunoglobulins (Angata et al., 2002), or
- M–type which binds mannose oligosaccharides
  (Endoplasmatic Reticulum associated α–mannosidase like proteins).

Members of the mannose binding receptor family are a unique subgroup within the C–type lectin superfamily that contains multiple C–type lectin-like domains (CTLDs) within a polypeptide backbone. From examination of the human genome sequence, four members are predicted where only the mannose receptor and Endo180/uPARAP have been demonstrated to bind monosaccharides (East and Isacke, 2002). A schematic overview of the mannose receptor domains is presented in Figure 6.1a. All members of this family carry an N-terminal cystein-rich domain, which can act as second lectin domain that binds to sulfated sugars in case of the mannose receptor (e.g. chondroitin sulfate A and B, or Lewis^X antigens (Leteux et al., 2000)), followed by a single fibronectin (FN) type II domain that will bind collagens. The C-terminus consists of a single–pass transmembrane unit ending with short cytoplasmatic domains that can interact with the endocytic signaling cascade of the cell. The mannose receptor is highly expressed on macrophages (therefore formerly termed as "macrophage mannose receptor") and has been assigned the cluster differentiation number CD206. It is a $175\,\mathrm{kDa}$ protein that recognizes saccharide chains terminating in mannose, fuctose or N-acetylglucosamine (Largent et al., 1984; Shepherd et al., 1981) with highest monosaccharides binding affinity for *D*-mannose (Zamze et al., 2002). The mannose receptor has 8 CTLDs, where only domains 4 to 8 display binding affinity as carbohydrate recognition domains (CRDs) and monosaccharide binding was solely identified for CTLD4 (Taylor et al., 1992). CRDs have a distinct protein fold characteristic to bind carbohydrates. Their specific sequence profiles are summarized in the broader group of CTLDs that do not necessarily bind sugars

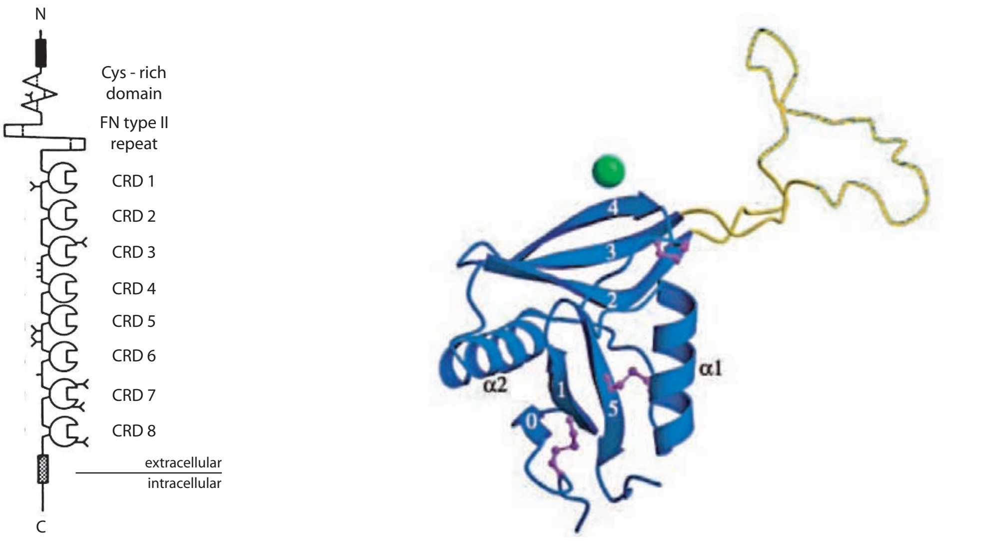

(a) (b)

Figure 6.1.: (a) Structure of the mannose receptor with CRDs labeled from 1–8. Adapted from Taylor et al. (1992). (b) Ribbon diagram of mannose receptor CTLD4 with extended loop (yellow) and Ca^{2+} (green). Adapted from Feinberg et al. (2000).

and are part of the standard annotation in all major protein databases. Figure 6.1b shows the ribbon diagram of the mannose receptor CTLD4 with bound Ca^{2+} as green sphere (Feinberg et al., 2000). It has been demonstrated, that CTLD4 requires 2 Ca^{2+} for sugar binding (Mullin et al., 1994). The crystal structure of the mannose receptor CTLD4 shows an extended loop (yellow) where the second Ca^{2+} binding site is located. This auxiliary site is proposed to act as pH sensor. After the mannose receptor is internalized into the cell's endosome, the low pH environment releases Ca^{2+} and consequently its bound ligand (East and Isacke, 2002).

6.1.2. Macrophages

Macrophages are white blood cells (leukocytes) constitutively present in nearly any tissue of the body. They regulate homeostasis and contribute on essential functions during inflammation and repair. Macrophages differentiate from monocytes and are part of the mononuclear phagocytic system. Their ability to identify and internalize foreign substances (phagocytosis) is part of the earliest evolutionary innate immune strategies. Macrophages migrate via blood and lymph to peripheral sites where they are able to persist as relatively long-living cells. There they adapt to local tissue specific stimuli which results in phenotypic heterogeneity. Macrophages play an important role in the clearance of effete components, such as apoptotic cells or environmental particles, and capture potential antigens to activate T and B lymphocyte as part of the adaptive immunity. To recognize all classes of endogenous and exogenous stimuli, macrophages express a broad range of specific plasma membrane receptors (Gordon, 2002; Sahly et al., 2008; Ofek et al., 1995). In this study, the isolated clonal population J774.A1 from a murine macrophage tumor cell line was used, which shows an up–regulated and functional surface expression of the mannose receptor. According to Fiani et al. (1998), they express an average number of $46\,600$ mannose binding receptors on the surface with an equilibrium binding constant $K_d = 92.9\,\mathrm{nM}$ for a mannose BSA ligand. The mannose receptor is involved in adaptive and innate immune response. As described in Subsection 6.1.1, it binds to carbohydrate moieties for pathogen recognition or membrane-associated adhesion with a high affinity for D-mannose. Increasing evidence suggests the mannose receptor plays a participating role in silent the clearance of inflammatory molecules (Zamze et al., 2002).

6.2. Experimental Detection Methods

Cellular response on external stimuli is difficult to resolve within a three–dimensional tissue. Therefore, simplified *in vitro* systems that allow for a punctual defined stimulation of target cells and a spatial resolved detection of cell response are often preferred. This reduces the complex biological environment to a system of a few target molecules and locally well defined interactions. A powerful approach to mimicking such biological functions on flat sample geometries are solid supported membranes (Tanaka and Sackmann, 2005). They allow for data acquisition with optical microscopy and other elaborate measurement techniques. In this study, several solid supported membrane preparation techniques, presented in Chapter 3, were used to prepare functional FL10Man lipid domains within a flow chamber setup (Section 2.3). The flow chamber allowed for nutrition of cells with matched culture medium, selective cell targeting (FL10Man, CD95L), and unperturbed cellular observation through the use of inverted microscopy techniques. Cellular response was observed by a combination of reflection interference contrast microscopy and confocal fluorescence microscopy, which will be introduced shortly to permit conclusive interpretation of the acquired data.

6.2.1. Reflection Interference Contrast Microscopy

Reflection interference contrast microscopy (RICM) utilizes the interference of polarized light reflected from interfaces of stratified multilayer systems. In cell biology it was first invented by Abercrombie and Ambrose (1958) and Curtis (1964), and further improved in the group of Prof. E. Sackmann (TU Munich, Germany), e.g. Rädler and Sackmann (1993); Zilker et al. (1992); Schilling et al. (2004), for

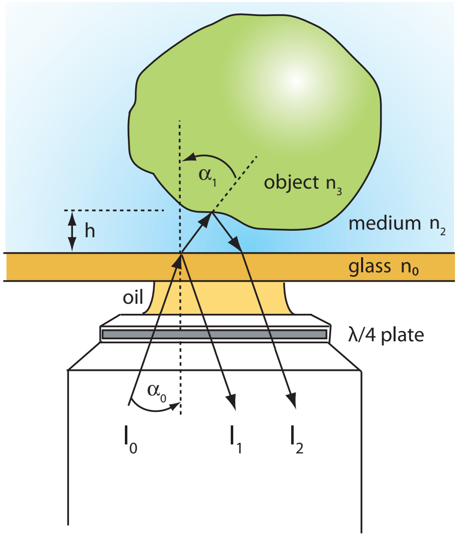

Figure 6.2.: Sketch of a RICM reflection geometry.

membrane spreading and fluctuation studies on various surfaces. RICM is a label free technique that measures the distance h between surface near cell membranes and the sample substrate due to changes in the refractive index. The resolution in lateral direction is similar to common light microscopy techniques ($\sim 0.2\,\mathrm{\mu m}$), whereas the vertical resolution can improve by interferometric effects down to $\sim 4\,\mathrm{nm}$. Figure 6.2 shows a sketch of a typical reflection interference geometry for cells in close proximity to the surface. A description for the used modular RICM setup is given in Section 2.7.

The height information $h(x,y)$ is deduced from the intensity $I(x,y)$ measured at a given lateral position (x,y) for quasi-normal incidence by,

$$I(x,y) = I_1 + I_2 + 2\sqrt{I_1 I_2}\gamma_{12}\cos\left(\frac{4\pi n_2}{\lambda}h(x,y) + \varphi\right)\,, \tag{6.1}$$

where λ is the used wavelength, n_2 the refractive index of the medium, and φ a phase shift usually close to π. I_1 and I_2 are reflected intensities that calculate from the incoming light intensity I_0. γ_{12} denotes the mutual degree of coherence between two points at $\vec{r_1}$ and $\vec{r_2}$. For two completely coherent light rays it is unity and decreases with partial coherence towards zero for completely incoherent light. Around a given point $\vec{r_1}$ one can define a certain coherently illuminated volume before γ_{12} falls below a prescribed value like $1/e$ (Saleh and Teich, 2007, p. 415). The width and shape of this function is described by the points spread function (PSF) of a microscope and can be directly modulated with the aperture diaphragm. The opening size of the aperture regulates the maximal accepted inclination α_0 of illuminating light rays and thus the numerical aperture of illumination I.N.A. $= n_2 \sin\alpha_1$. The coherence in z-direction parallel to the optical axis can be written as (Limozin and

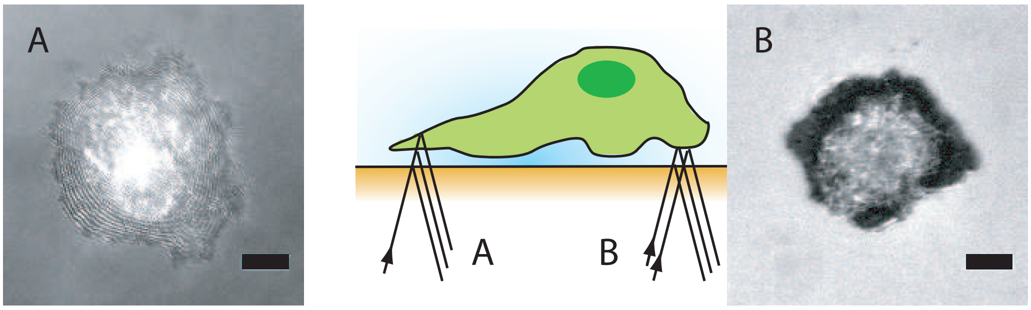

Figure 6.3.: Interference image of an adherent cell recorded with A) closed, and B) open aperture diaphragm regulating the depth of coherence length for illumination. Scale bars are 5 µm

Sengupta, 2009):

$$\gamma_{12} = \frac{\sin\beta}{\beta} e^{i\beta} \tag{6.2}$$
$$\beta = (\frac{4\pi}{\lambda} \frac{h(x,y)}{n_2} \text{I.N.A.}^2).$$

The degree of coherence limits the horizontal resolution Δx either by the I.N.A. for closed aperture (more coherent), or by the Rayleigh criterion of the objective N.A. for an open aperture (rather incoherent) (Limozin and Sengupta, 2009):

$$\frac{0.5\lambda}{I.N.A.} \leq \Delta x \leq \frac{0.61\lambda}{N.A.} \tag{6.3}$$

In other words, for a closed aperture the depth in focus is high and interference fringes of coherent light can be caused by multiple stratified interfaces. Situation A in Figure 6.3 demonstrates this for a flattened pancreatic cancer cell, where overlaying membranes cause interference fringes at the lamelopodiom of the cell. In contrast, situation B shows a cell imaged with open aperture, where interference arises only at the vicinity of the focal plane and deeper regions do not contribute. Here, regions of cell contact appear dark. Interference at the center of the cell can fluctuate, since cell organelles like the nucleus change considerably the intercellular refractive index.

To judge whether tight contact of cells induces constructive or destructive interference, one needs to consider the phase shift φ for a given reflection layer system (Figure 6.4a). A light ray reflected under normal incidence ($\alpha = 0$) at an interface with decreasing refractive index ($n_0 > n_1$) reduces its intensity according to Fresnel's formula (Hecht, 2001),

$$I_1 = I_0 \left|r_{01}\right|^2 = I_0 \left|\frac{n_1 - n_0}{n_1 + n_0}\right|^2 . \tag{6.4}$$

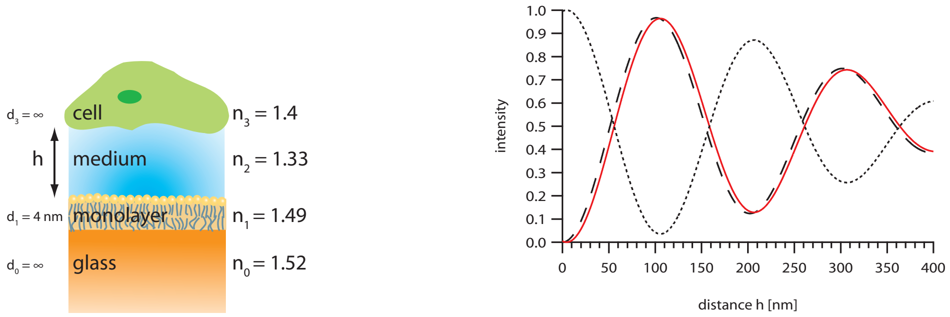

(a) (b)

Figure 6.4.: (a) Layer model and refractive indices for a triple interface system used for the calculation of height profiles. (b) Normalized interference intensity profile of a hovering cell in distance h above the surface (solid). A missing phase jump π at the medium/cell interface (dotted) or a interposed lipid monolayer (dashed) results in modified intensity profiles.

Only the transmitted ray experiences a phase shift of $\varphi = \frac{2\pi}{\lambda} n_1 d_1$. This is the case at the glass lipid interface of the additionally LB deposited monolayer. Since the light ray I_2 passes the monolayer twice, its thickness d_1 enters into the phase shift calculation two times. At an interface with increasing refractive index, e.g. from medium to cell ($n_2 < n_3$), the reflected ray experiences an additional phase shift of $\varphi = \pi$. In Equation 6.1 both enter as constant term φ while the phase shift induced by the medium pathway modulates with h. The intensity of the second ray is calculated by repeated application of Fresnel coefficients at each interface:

$$I_2 = I_0 \left| r_{01} + (1 - r_{01}^2) e^{i\frac{4\pi}{\lambda} n_1 d_1} [r_{12} + r_{23}(1 - r_{12}^2) e^{i\frac{4\pi}{\lambda} n_2 h}] \right|^2 \tag{6.5}$$

Figure 6.4b presents the intensity profile for a hovering cell with distance h above a monolayer functionalized glass substrate (red, solid line). In close contact destructive interference occurs and the adhesion spot appears dark. With increasing distance h, the intensity passes several interference maxima and minima until the lost coherence suppresses further discrimination. The dashed line indicates the same situation for an uncoated glass substrate. Here, the additional lipid monolayer causes only marginal phase shift, although a better contrast,

$$c = \frac{I_{max} - I_{min}}{I_{max} + I_{min}} = \frac{\text{Dif}}{\text{Sum}}, \tag{6.6}$$

can be reached. It should be noted, that all intensity profiles in Figure 6.4b are normalized on the first maximum and minimum position to allow direct comparison of the phase shift. Damping of the intensity occurs due to the loss in coherence. In general, at interfaces with high refractive index gradients, more light is reflected and thus a higher interference intensity is observed. Rädler and Sackmann (1993) used this principal to improve RICM contrast with magnesium fluoride $\mathrm{MgF_2}$ coated substrates. In this study, main focus was set on the surface near ($< 100\,\mathrm{nm}$) cell membrane topography and thus an open aperture blend and a high CCD camera sensitivity provided enough dynamic range to resolve the interference fringes at monolayer coated substrates. The dotted line in Figure 6.4b notionally represents the intensity profile for an object with refractive index smaller than the medium, where no phase shift of π occurs. It demonstrates that the intensity without any object in the medium is maximal at the surface, which provides a good reference situation for the adjustment of the $\lambda/4$ plate. It is noted that a glass substrate with supported membrane and interposed medium causes a different phase shift than the monolayer coated profile in Figure 6.4a. Due to alternating gradients of refractive indices, the first interference minimum is shifted around $40\,\mathrm{nm}$ above the surface (Limozin and Sengupta, 2009).

To measure the absolute cell distance h, reliable knowledge on all refractive indices is needed. In practice, it is easier to measure the difference in intensity $I(x,y)$ towards the next fringe maximum $I_{max} = I_1 I_2 + 2\sqrt{I_1 I_2}$ and minimum $I_{min} = I_1 I_2 - 2\sqrt{I_1 I_2}$ intensity. Using the introduced definitions for *Sum* and *Dif* in Equation 6.6 to rearrange Equation 6.1, the height profile of an adhered cell can be calculated for the corresponding cosine branch by

$$h(x,y) = \frac{\lambda}{4\pi n_2} \arccos \frac{2I(x,y) - \mathrm{Sum}}{\mathrm{Dif}}. \tag{6.7}$$

6.2.2. Image Analysis Routines

To determine quantitative cellular measures from RICM images, e.g. the adhesion area, an image analysis routine was programmed in Java for ImageJ 1.44 (Abramoff et al., 2004) based on ideas presented in Sengupta et al. (2006). The algorithm exploits the fact that the background intensity of an RICM image is more uniform than the interference signal caused by a cell. This is particularly the case for a fluctuating cell membrane that is not tightly bound to the substrate. The membrane fluctuations cause interference intensity patterns with a high standard deviation either over time or towards the neighboring pixel positions.

Cellular adhesion areas were discriminated from the background by a combined algorithm for variance filtering and intensity thresholding. In regions of tight contact, the standard deviation varies only little from the fluctuations of the background signal. At the same time, the intensity signal is considerably lower due to destructive interference. To allow for a semi-automatic application of the digital image analysis routine, RICM images with high contrast and a homogeneous background illumination were needed. This issue was technically moderated by the use of a sensitive CCD camera with high dynamic range and 32–bit color depth, as well as illumination with an open aperture blend as explained in Subsection 6.2.1. In post image processing, a reference value of the background signal was averaged over a

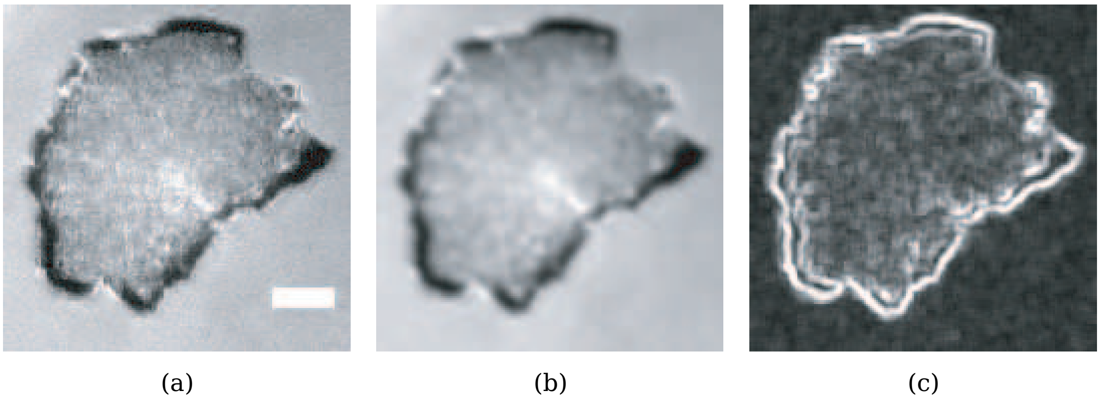
(a) (b) (c)

Figure 6.5.: (a) RICM image of an adherent macrophage with (b) 5×5 binned mean values and (c) standard deviation up to the next nearest neighbor pixel. The scale bars is $5\,\mathrm{\mu m}$.

user–set rectangular selection around the cell. Mean intensity values and standard deviation were averaged over all pixels along the border line. Subsequently, the image analysis algorithm calculated the mean values of all 5×5 pixel matrices of the selection, i.e., from all next nearest neighbor pixels, and the standard deviation, i.e., the spread of these 5×5 matrices. Figure 6.5(a) shows a typical RICM image of an adherent macrophage, (b) its 5×5 pixel binned mean image, and (c) the corresponding standard deviation map. In a first filtering step, all pixels with a spread less than the standard deviation of the background were assigned to the value 0, and others to 1. The situation is shown in Figure 6.6(a), where areas within the adhesion region of the cell are also assigned to the background (0). To correct this misinterpretation, the contour line of the adhesion area was extracted by a simple edge detection routine (Figure 6.6(b)) and all enclosed pixels were assigned to 1. Subsequently, adhesion areas with tight membrane-substrate were subjected to a second filtering step, where all 1 valued pixels that posses lower intensity than the mean background intensity are assigned to 2. The result is denoted as trinary map and is shown in Figure 6.6(c). An additional filtering step used a lower intensity threshold for the adhesion area of cells. Adherent regions with intensities below the mean background intensity minus twice its standard deviation were assigned to 3. This threshold value was chosen arbitrarily, but emerged as a good detection limit for dark adhesion spots within the original RICM image. The final adhesion map is shown in Figure 6.6(d), where the black area (0) denotes the background, and all brighter colors (1,2,3) are assigned to the cellular adhesion area with different levels of cell–membrane contact. The image analysis routine additionaly derived values for the cellular adhesion area A, the contour line perimeter p, and the cellular form factor $c = 4\pi A/p^2$.

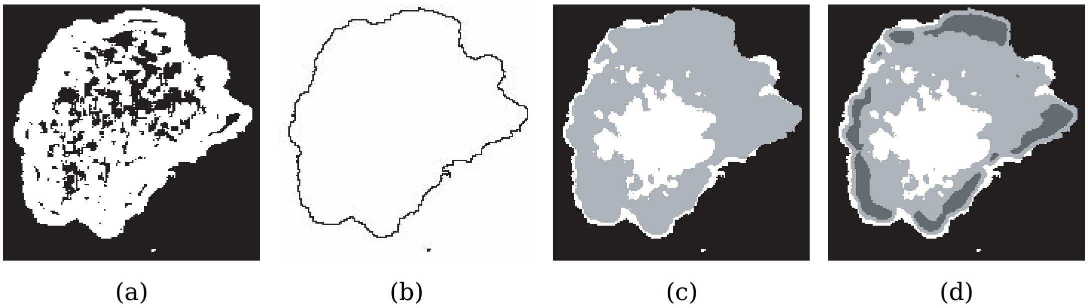
(a) (b) (c) (d)

Figure 6.6.: Intermediate maps of RICM image after (a) standard deviation filtering, (b) edge detection, and (c) background intensity thresholding. (d) Final image discriminates background (black) from different levels of cell adherence.

6.2.3. Three-Dimensional Cell Shape Reconstruction

The adhesion process of cells is not only restricted to the cell contact area, but is also accompanied by cytoskeletal reconstruction of the cell body (Lodish et al., 2001, p. 847). Therefore, three-dimensional cell shapes were reconstructed with a label-free RICM technique and a cytoskeletal staining of the polymerized actin network of cells.

In a first static attempt, RICM was used with a closed aperture blend to reconstruct surface-near membrane undulations and extended cell shapes in z–direction. Figure 6.7(a) shows an erythrocyte lying on the surface and (b) hovering tilted above the surface. In both cases, clear Newton–fringes of constructive and destructive interference are visible. Using Equation 6.7 and a manual assignment of the respective cosine branches resulted in a three-dimensional height reconstruction as shown in Figure 6.7(c–d). As demonstrated, this method is useful for cells or objects with known geometrical shapes. The situation becomes more complicated in the case of adherent cells with unknown shape and enclosed organelles. Figure 6.8a shows an adherent pancreatic cancer cell with distinct lamellopodium and individual filopodia. The center of the cell appears noisy due to disturbances of the refractive index by organelles. Considering a second interference contribution from the overlying cell membrane with an open aperture blend, the thickness increase of the lamellopodium was calculated. Figure 6.8b presents the height profile of the upper cell membrane. The layer model for height reconstruction assumed a cell–substrate distance of $32\,\mathrm{nm}$ (see Section 6.3), a refractive index for the upper and the lower cell membrane of 1.4, a membrane thickness of $4\,\mathrm{nm}$, a cytosolic refractive index of 1.4, and a refractive index for the surrounding medium of 1.33. The profile was reconstructed along the red line sketched in Figure 6.8a. The inclination of the upper lamellopodium membrane was fitted to $4.0°$. A complete reconstruction of the cell surface can be relevant to calculating force fields under hydrodynamic flow.

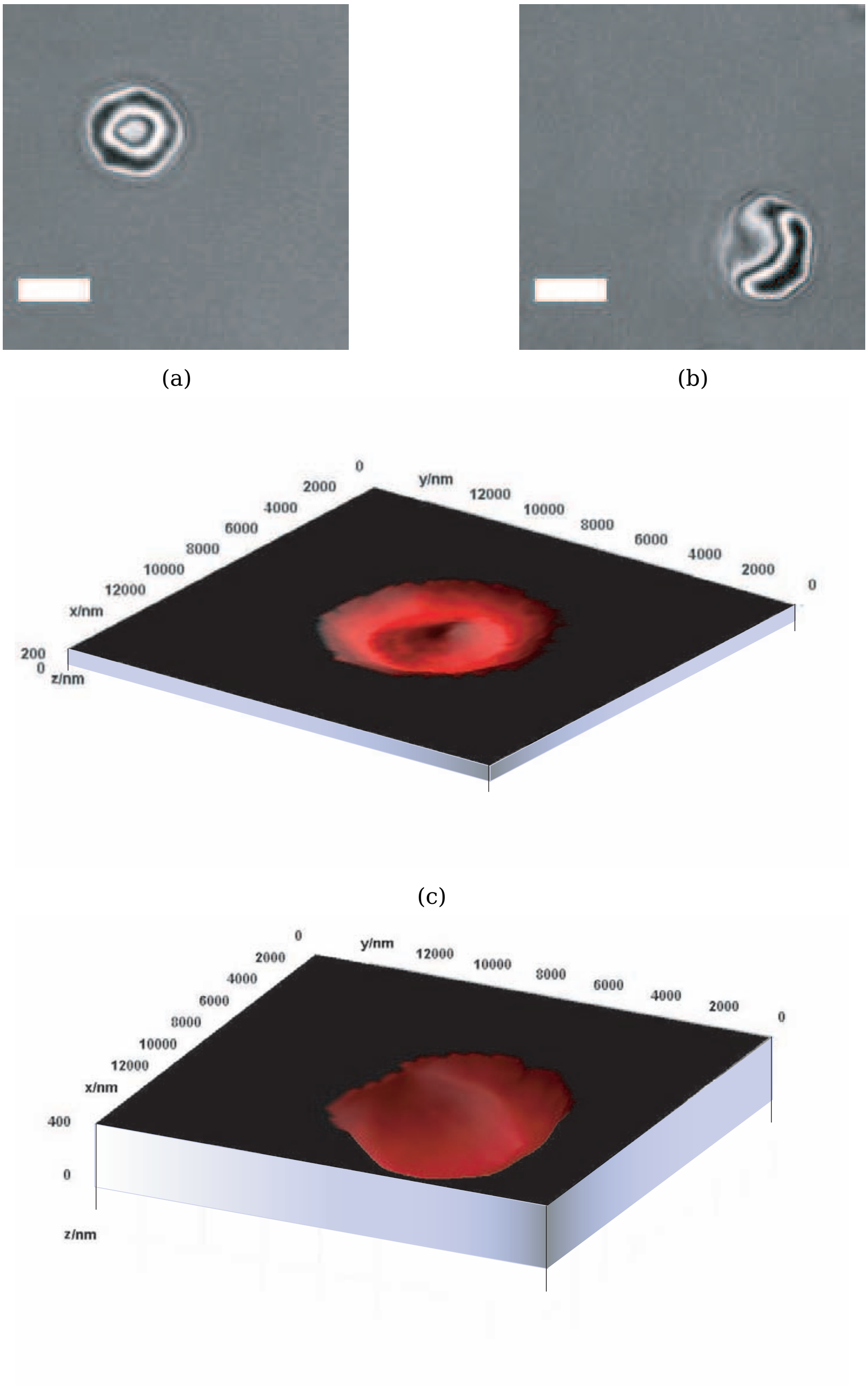

(a)

(b)

(c)

(d)

Figure 6.7.: (a) RICM images of an erythrocyte lying on the surface and (b) hovering tilted above the surface. (c–d) Respective three-dimensional shape reconstructions shown from below. All scale bars are 5 µm.

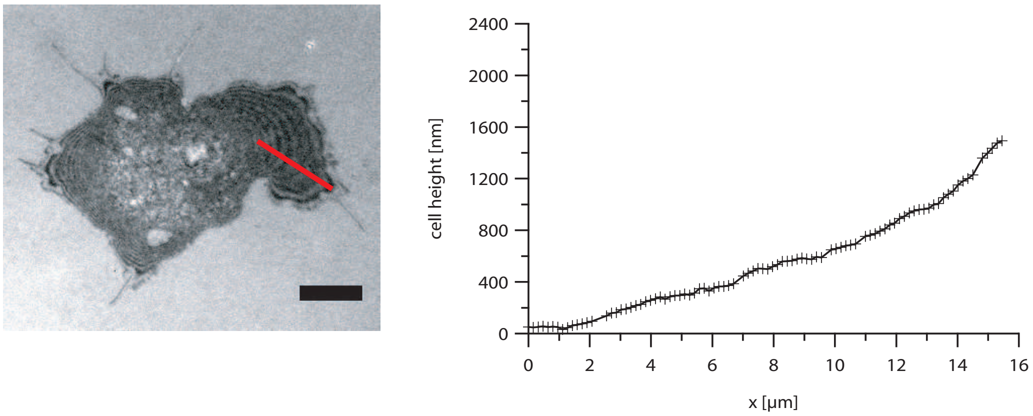

(a) (b)

Figure 6.8.: (a) RICM image of an adherent pancreatic cancer cell and (b) its height profile reconstruction along the red line. The scale bars is $10\,\mu\mathrm{m}$.

Nonetheless, the limited profile reconstructions to areas which are unperturbed from light scattering of cell organelles emerged as serious drawback of the RICM technique.

Furthermore, adherent cells on supported membranes were explored by confocal microscopy and subsequently the three-dimensional shape reconstruction. Adherent cells were fixed and stained for actin which is a major structure protein of the cytoskeleton. Actin is involved in cell adhesion and motility processes and accumulates in network structures above focal adhesion spots. Visualization and reconstruction of the complete cell volume was enabled by extended image scans in z–direction. The image stacks were recorded with a stack spacing of $250\,\mathrm{nm}$ and $\sim\ 260\,\mathrm{nm}$ lateral resolutions at the Nikon Imaging Center (BIOQUANT, Heidelberg, Germany). Subsequent deconvolution of the fluorescence images eliminated the out–of–focus haze and thereby improved the spatial resolution. The three-dimensional image reconstructions and further image processing were performed with ImageJ 1.44 (Abramoff et al., 2004). Details on the instrumental equipment are given in Section 2.6.

6.3. Cellular Response on FL10Man Domains

In the following, the static and dynamic behavior of adherent macrophages was analyzed by a combination of confocal microscopy and RICM measurements to describe the cellular response of macrophages on mannose displaying membranes.

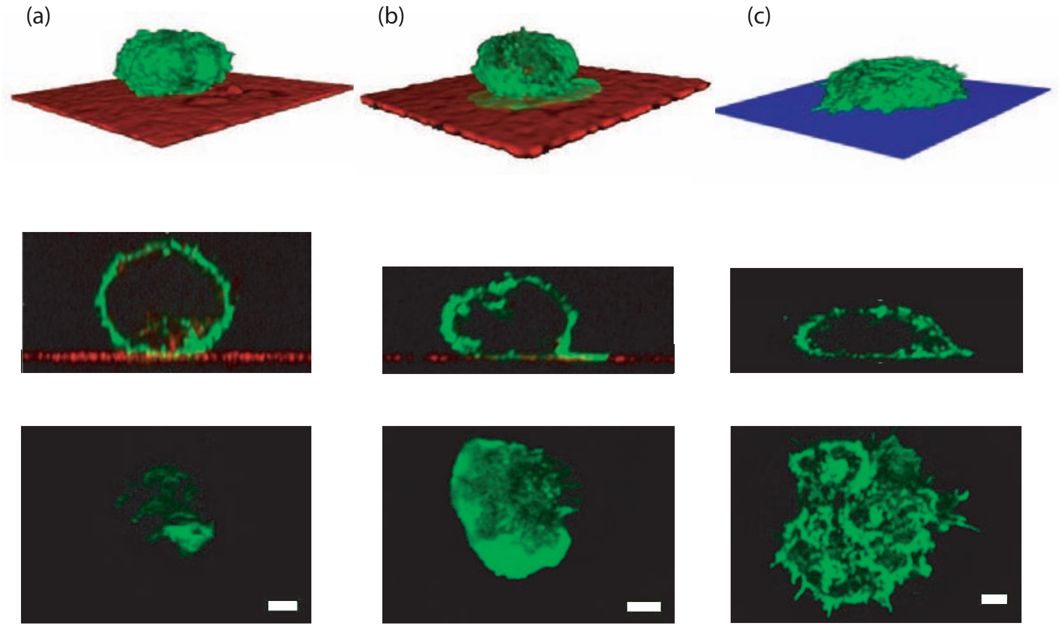

Figure 6.9.: Confocal images of adherent macrophages on (a) pure DOPC (b) $33\,\mathrm{mol\%}$ FL10Man : $67\,\mathrm{mol\%}$ DOPC, and (c) pure FL10Man membranes. All scale bars are $5\,\mathrm{\mu m}$.

6.3.1. Cell Spreading of Macrophages on FL10Man Domains

The adhesion behavior of murine macrophage (J774A.1) on functional α-D-mannose lipid domains was quantified by live cell RICM imaging and three–dimensional shape reconstruction by confocal microscopy. Therefore, cells were incubated for at least $2\,\mathrm{h}$ under controlled temperature ($37\,^{\circ}\mathrm{C}$) and CO_2 ($5\,\%$) conditions on supported membranes. Figure 6.9 presents the three–dimensional reconstruction, the cross sectional side view, and the adhesion plane of macrophages on membranes composed of (a) pure phospholipids (DOPC), (b) domains of $33\,\mathrm{mol\%}$ FL10Man and $67\,\mathrm{mol\%}$ DOPC, and (c) pure FL10Man. Since pure FL10Man could not be doped with TexasRed®–DHPE, the position of the supported membrane is indicated as the blue layer. It should be noted that the number of cells found on the pur DOPC substrates (a) was reduced by more than $90\,\%$ as compared to the number of adherent cells on FL10Man exposing membranes (b) and (c). This is ascribed to a weak, nonspecific binding of macrophages on phospholipid membranes. Nearly all cells were removed by a gentle exchange of cell medium during sample preparation and only those cells adherent to the substrate at monolayer defects remained attached. The fluorescence labeling of the actin cortex with phalloidin (green, Figure 6.9) implies that most cells on DOPC membranes were round and showed only a small contact area. The cell volume was calculated to be $\sim\,4400\,\mathrm{\mu m}^3$ and the adhesion

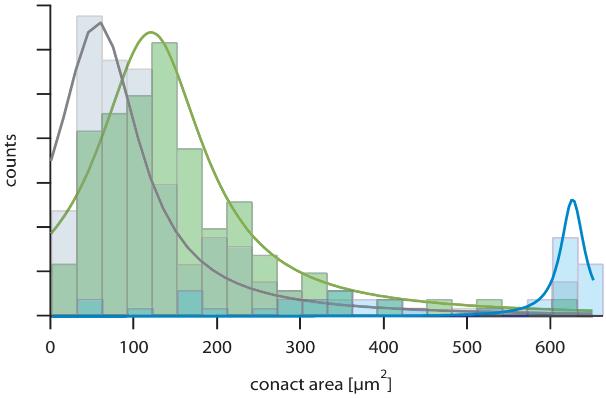

Figure 6.10.: Histograms and Gaussian fits on adhesion area of macrophages spread on membranes displaying only DOPC lipids (black), $33\,\mathrm{mol\%}$ FL10Man domains in a DOPC matrix (green), and only FL10Man lipids (blue).

area was smaller than $A_{\mathrm{DOPC}} = 10\,\mathrm{\mu m}^2$. The histograms of adherent macrophages after $4\,\mathrm{h}$ are presented in Figure 6.10. The average adhesion area of macrophages on DOPC membranes (black) was $60\,\mathrm{\mu m}^2$. In fact, a clear identification of the contact area for macrophages on DOPC by RICM was rather difficult, since the significant height fluctuations of cell surface resulted in a large intensity standard deviation. Thus, the image analysis routine presented in Subsection 6.2.2 could not cope with very small adhesion spots. An apparently stronger and more specific adhesion of macrophages was found on FL10Man membranes. Here, even intensive rinsing could not remove the cells from the membranes. Membranes with $33\,\mathrm{mol\%}$ of incorporated mannosylated domains, caused a distinct spreading of macrophages. The cross sectional view (Figure 6.9 (b)) shows a thin lamelopodiom protruding onto the peripheral substrate membrane, whereas the cell body remains round. The cell volume was calculated to $\sim 5000\,\mathrm{\mu m}^3$, whereas the average adhesion area after $4\,\mathrm{h}$ increased to $120\,\mathrm{\mu m}^2$. The histogram with Gaussian fit (green) around the average adhesion area is presented in Figure 6.10. An enrichment of actin was observed in the lamellopodium, although an accumulation of actin above domain was not identified. Figure 6.9(c) shows the situation for macrophages on pure FL10Man membranes. Cell spreading becomes even more prominent and macrophages start to flatten on the supported membranes. The calculated cell volume of $\sim 4000\,\mathrm{\mu m}^3$ remains within the statistical size deviation of cells below $15\,\%$. On pure mannosylated supported membranes, the contact area increased significantly to $630\,\mathrm{\mu m}^2$ (blue curve in Figure 6.10). Within the plane of adhesion, i.e., directly above the substrate, punctuated actin structures were found. The shape of the spreading area was round and indicated no preferential orientation or polarization of the cell. Albeit, the outline of the contact area revealed many short fluctuating filopodia and suggests enhanced cytosolic cell activity.

Figure 6.11 shows adhesion areas of macrophage on membranes with $33\,\mathrm{mol\%}$ incorporated mannose domains. The RICM images are sorted by the size of the adhesion area which increased with incubation time. During the early stage of cell adhesion, inhomogeneous interference patterns are caused by non–adherent parts of the cell. After formation of a stable adhesion area, the outer lamellopodium region came into close contact with the substrate and developed destructive interference. A dark adhesion region evolved and generated a closed rim of tight cell–substrate contact. The overall shape of the adhesion areas was nearly round with circularity above 0.5.

To study the spatial correlation between FL10Man domains and the initial area of macrophage adhesion, RICM timelaps images of macrophages were recorded during the early stage of cell adhesion. Figure 6.12(a-c) shows the contact area of a macrophage binding onto a $33\,\mathrm{mol\%}$ FL10Man domain substrate at time steps of $1\,\mathrm{min}$, $5\,\mathrm{min}$, and $10\,\mathrm{min}$. The RICM images revealed several discrete spots of tight cell-substrate contact (dark round spots). The time evolution of the adhesion spots even suggested a step-wise spreading of the cell adhesion area onto these adhesion spots. The spacing between the spots was comparable to the inter-domain distance ($a = 3.6\,\mu\mathrm{m}$) of $33\,\mathrm{mol\%}$ FL10Man domains. To clarify the spatial correlation between adhesion spots and FL10Man domains, experiments with TexasRed®-DHPE doped DOPC membranes were performed. Figure 6.12(d) shows RICM images of macrophage adhesion spots overlaid by the outlines of the membrane incorporated FL10Man domains (red lines). The domain outlines were derived from a fluorescence picture taken at the same position instantaneously before and after first cell attachment. Contrary to the expectations, no direct overlap of the adhesion spots with FL10Man domain was observed. First contacts of tight adhesion rather seemed to surround the mannosylated domains.

6.3.2. Recognition of FL10Man Domains by Macrophages

The recognition of FL10Man domains by macrophages during cell spreading was studied with RICM image streams. Cell membrane fluctuations of different adhesion regions were evaluated with a time resolution of $110\,\mathrm{ms}$. Figure 6.13(a) shows recorded height fluctuations of four different macrophage adhesion areas above FL10Man domains and one control spot for the background variations. The recording spots were assigned to a region of (1) tight contact (dark region), (2) ordinary adhesion, and (3) a FL10Man domain which is currently engulfed by the macrophage. For comparison, an adhesion site (4) without underlying FL10Man domain and (5) a spot for background intensity fluctuations were recorded. The respective positions are indicated by arrows in Figure 6.13(b). Extracted domain outlines (red lines)

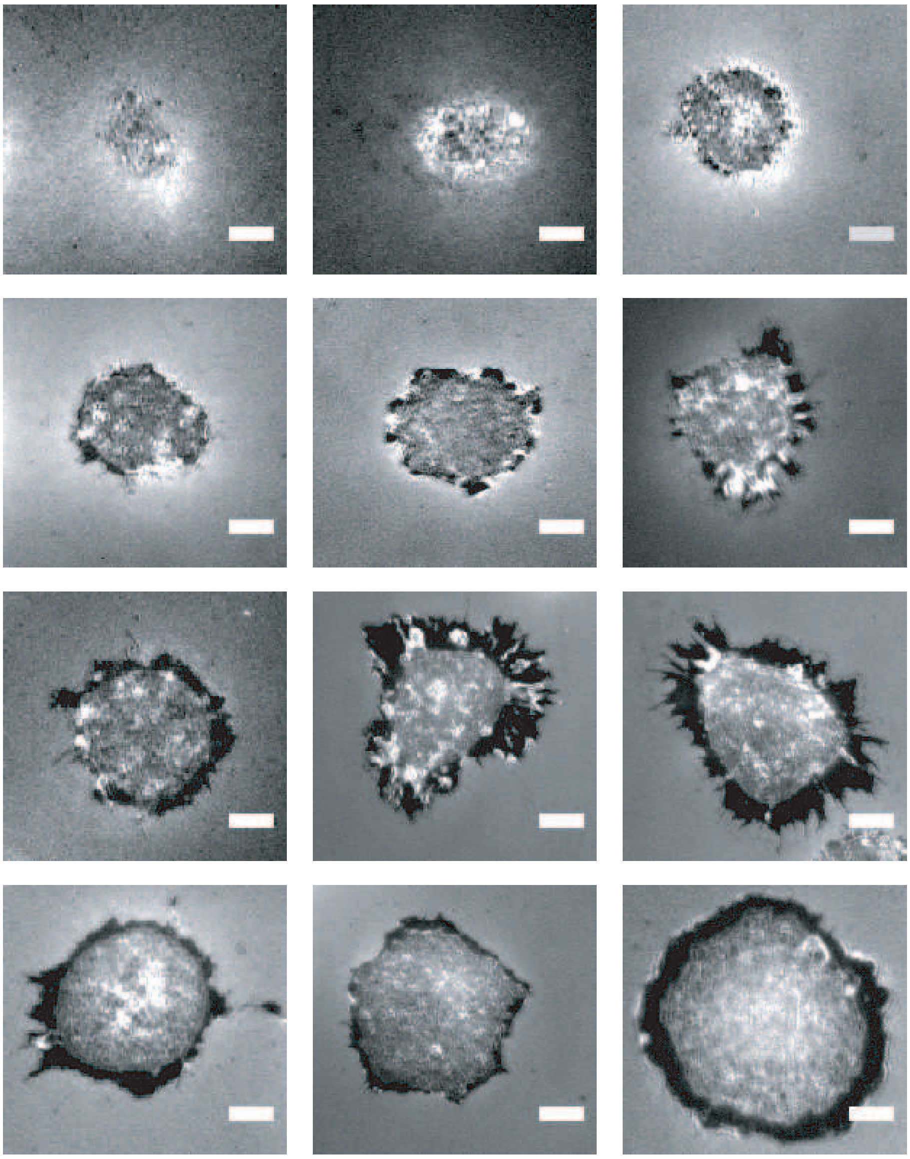

Figure 6.11.: Typical RICM images of adherent macrophages on substrates with 33 mol% FL10Man and 67 mol% DOPC sorted for increasing incubation time of macrophages. All scale bars are 5 µm.

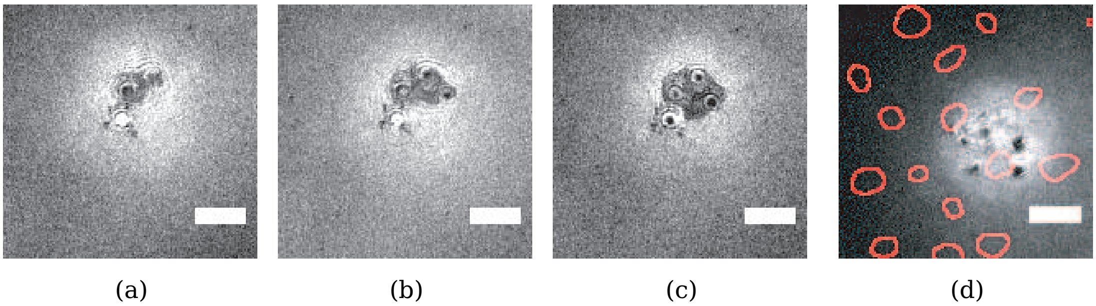
(a) (b) (c) (d)

Figure 6.12.: Macrophage adhesion on $33\,\mathrm{mol\%}$ FL10Man domains by RICM showing discrete dark adhesion spots. Images were recorded (a) $1\,\mathrm{min}$, (b) $5\,\mathrm{min}$, and (c) $10\,\mathrm{min}$ after first cell-substrate contact. (d) Overlay of adhesion spots with contour lines of FL10Man domains (red) extracted from fluorescence microscopy. All scale bars are $5\,\mathrm{\mu m}$.

are overlaid from a fluorescence image taken instantaneously before data acquisition. The presented height profiles were calculated with Equation 6.7 for a 3×3 binned pixel area. The macrophage membrane height fluctuations above spot (1) revealed an average cell substrate distance of $30.3\,\mathrm{nm}$ with a standard deviation of $0.8\,\mathrm{nm}$. Spot (2) showed a slightly enlarged substrate distance of approximately $32.8\,\mathrm{nm}$ with a standard deviation of $1.1\,\mathrm{nm}$. The macrophage adhesion site (3), without an underlying FL10Man domain, revealed a doubled standard deviation of $2.0\,\mathrm{nm}$ and an increased cell-substrate distance of $38.6\,\mathrm{nm}$. These results indicate a specific interaction of the macrophage with the underlying FL10Man-domains with a reduced cell-substrate distance. The observation is supported by spot (4), where the macrophage was spreading over the domain during data acquisition and showed a similar behavior. The calculated cell-substrate distance reduced from an unbound ($40\,\mathrm{nm}$) to a surface near membrane distance $32\,\mathrm{nm}$, where the height fluctuation amplitude became smaller. The cellular membrane fluctuation amplitudes were clearly discriminated from the illumination and camera noise, since spot (5) showed only a small intensity standard deviation of $0.3\,\mathrm{nm}$ for the background.

Since macrophage adhesion sites above FL10Man domains showed a smaller height standard deviation than other adhesion areas, the temporal height standard deviation of the complete adhesion area was calculated. Figure 6.14(a) shows the temporal height fluctuations of the macrophage membrane over a period of $2\,\mathrm{min}$. An overlay of the FL10Man-domain outlines (white) revealed good correlation with regions of low membrane height standard deviations (dark blue). In comparison, the spatial standard deviation map from a single RICM image is shown in Figure 6.13(b). Here, the lateral height standard deviation is calculated according to the RICM image analysis routine explained in Subsection 6.2.2. The combination of lateral vari-

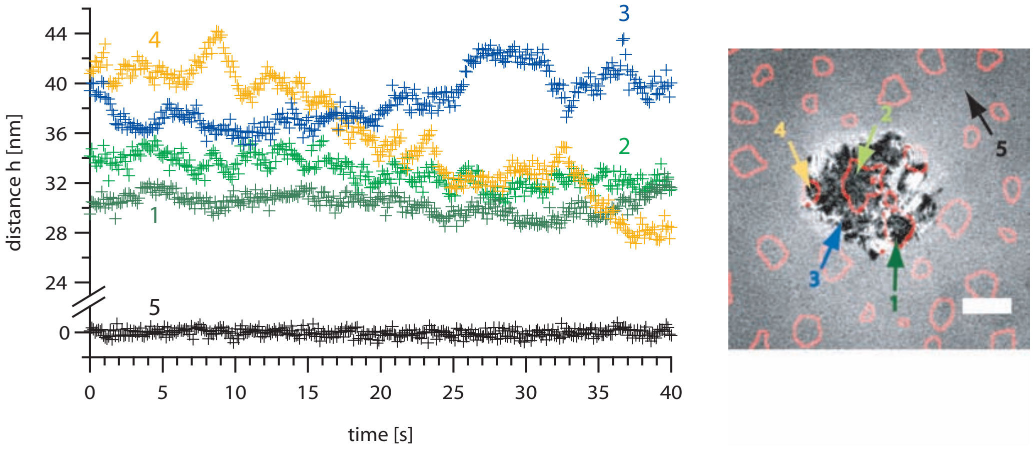

(a) (b)

Figure 6.13.: (a) Membrane height fluctuations of an adherent macrophage on FL10Man-domains showing (1) tight cell-membrane contact, (2) ordinary adhesion, and (3) spreading of the macrophage on a FL10Man domain. (4) Reference spot of macrophage adhesion area without underlying FL10Man-domain and (5) for the background intensity variations. (b) Overview of RICM recording spots with an overlay of FL10Man-domain outlines (red). The scale bars is 5 µm.

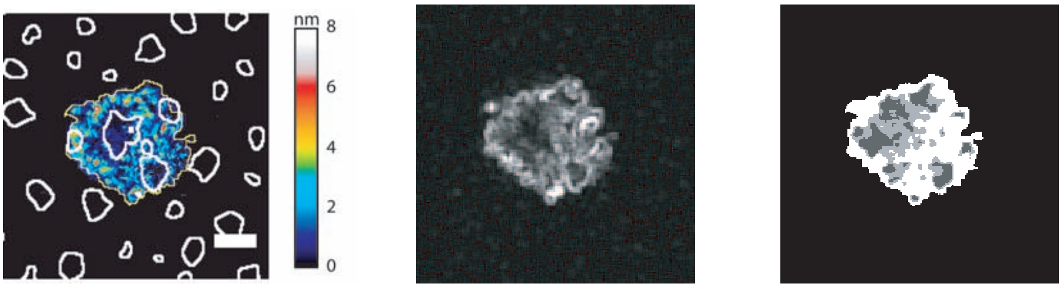

(a) (b) (c)

Figure 6.14.: (a) Temporal height standard deviation shows conformance with underlying FL10Man domains (white outlines). (b) Spatial standard deviation, and (c) adhesion area map of Figure 6.13b. The scale bars is 5 µm.

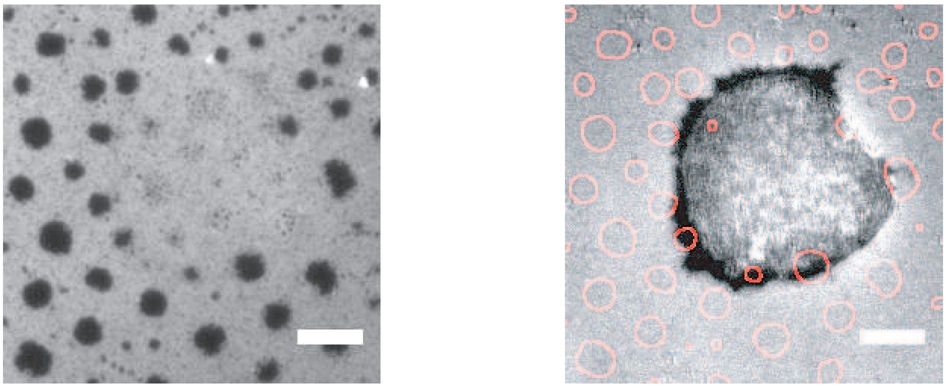
(a) (b)

Figure 6.15.: (a) Fluorescence and (b) RICM image of an macrophage adherent on $33\,\mathrm{mol\%}$ FL10Man domains after $4\,\mathrm{h}$ incubation. Domain outlines are overlayed (red) that show a depletion of domains below the adhesion area. The scale bars are $5\,\mathrm{\mu m}$.

ance filtering and background thresholding results in a cell adhesion map shown in Figure 6.14(c). For spatial variance filtering, no direct correlation between deduced adhesion pattern and FL10Man-domains was observed. This result suggests that a precise detection of cell adhesion areas for tight cell-substrate contact should include temporal variance filtering rather than spatial variance filtering.

As reported in Subsection 6.1.1, the mannose receptor is internalized into the macrophage's endosome after specific carbohydrate binding. To verify the specific recognition of mannose domains by macrophages, the long-term stability of FL10Man domains was checked. Figure 6.15(a) shows a fluorescence image of FL10Man domains below the adhesion area of a macrophage after $4\,\mathrm{h}$ incubation time. The pattern of FL10Man domains (black) shows a depleted region of domains in the center of the image. To compare the spatial correlation of domains with the macrophage adhesion area, FL10Man-domain outlines (red lines) were overlaid in Figure 6.15b with the respective RICM image of the adherent macrophage. It is obvious that domains are depleted only below the macrophage adhesion area, whereas in the peripheral supported membrane the FL10Man domains are unaffected. This suggests that macrophages ingest FL10Man lipids from the underlaying solid supported membrane to perform phagocytotic clearance of exogen molecules. In both observations, the close cell-substrate contact of macrophages above FL10Man domains and the specific recognition and uptake of mannosylated lipids demonstrate that the multivalent carbohydrate interactions of mannosylated domains could specifically activate the cell response of macrophages.

6.3.3. Conclusion

It was demonstrated that fluorinated lipid domains modified with α-D-mannose were able to activate the cell-specific response of murine macrophages (J774A.1). The adhesion behavior of macrophages was studied by a combination of confocal microscopy and microinterferometry (RICM). Macrophages showed significant spreading on the membranes with a high density of mannosylated-domains. A distinct recognition of mannosylated domains by macrophages was identified due to the reduced macrophage-substrate distance of $\sim 31\,\mathrm{nm}$ and the smaller amplitude of height fluctuations on FL10Man-domains. The pronounced cell spreading and a clearance of mannosylated lipids indicated that functional lipid domains can activate the nonopsonic, phagocytotic response (Ofek et al., 1995) of macrophages.

7. Response of Cancer Cells on Apoptosis-Inducing Membranes

In this chapter, the fluorinated lipid domains were modified with an apoptosis-inducing ligand molecule (CD95L) to act as model system for laterally confined signaling complexes in the cell membrane. The cellular response of pancreatic cancer cells was compared between membranes displaying CD95L-modified domains and membranes with homogeneously dispersed CD95L. At first, the biological role of the apoptosis-inducing ligand-receptor pair is described and subsequently the distinct differences of cell response between the CD95L-membrane substrates are elucidated.

7.1. Biological Role of Apoptosis

Apoptosis is an induced form of controlled cell death. Cells which undergo apoptosis enter a defined process of morphological changes that includes chromatin condensation, nuclear fragmentation, cell shrinkage, plasma membrane blebbing, and fragmentation of the cell into smaller apoptotic bodies. Neighboring phagocytosing cells will ingest and clear these bodies. In contrast, uncontrolled cell necrosis implies a disturbed integrity of the plasma membrane which leads to cell swelling and disruption. The cellular debris of necrotic cells causes inflammatory response and can damage the surrounding tissue. Induced apoptosis is an important regulatory process in tissue homeostasis and immune response (Steller, 1995). For instance, apoptosis promotes the sculpting of extremities (Chang et al., 2004) and is utilized as a regulatory mechanism of the immune system to clear virus infected cells (Krammer, 2000) or routes differentiation during development of the central nervous system (Martin-Villalba, 2006). The insufficient control on apoptosis causes malignant properties of cells, such as the uncontrolled growth and proliferation of cancer cells.

7.1.1. The CD95–CD95L Death System

In this study, a human pancreatic cancer cell line (PanD24) was isolated from a male donor. The PanD24 cancer cells were induced for apoptosis via the ’death receptor’ CD95. CD95 (cluster of differentiation 95) is a transmembrane protein also known as FasR, Apo-1, or DR2. The expression of CD95 can be boosted by cytokine or

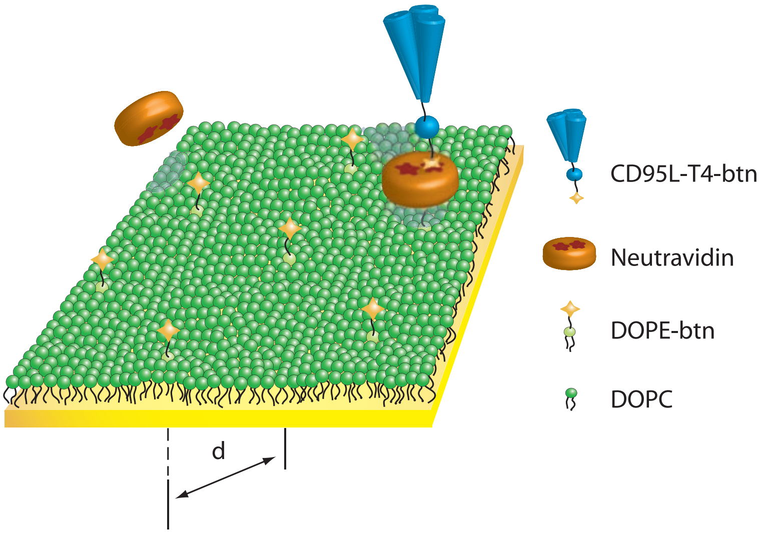

Figure 7.1.: Schematic illustration of solid supported membrane with homogeneously distributed ligand molecules bound via a biotin–Neutravidin bridge.

activation of lymphocytes (Krammer, 2000). In this thesis, the used pancreatic cancer cells showed a high CD95 surface coverage of $\sim 53\,000$ CD95 receptors per cell (Martin-Villalba). CD95 binds its natural ligand CD95L which causes oligomerization of the receptor and consequently triggers apoptosis.

CD95L, also known as FasL or Apo-1L, is an apoptosis inducing member of the tumor necrosis factor (TNF) cytokine family. It is a $40\,\mathrm{kDa}$ transmembrane protein with a highly conserved extracellular binding domain and a cleavage site for a matrix metalloproteinase (Suda et al., 1997). In cleaved conformation, the extracellular binding domain forms soluble homotrimers. Whether membrane bound CD95L is trimeric has not yet been demonstrated (Nagata, 1997). The human soluble homolog (hsCD95L) efficiently induces apoptosis. Bound to its receptor CD95, it induces trimerization of the receptor which stimulates the cytosolic formation of a death inducing signaling complex (DISC). In this study, a stabilized and biotinylated homotrimer (CD95L-T4-btn) from Apogenix GmbH (Heidelberg, Germany) was bound to different supported membranes containing biotinylated lipids (btnFL17, DOPE-btn) as described in Section 2.12. A schematic illustration for a membrane displaying homogeneously dispersed ligand molecules is shown in Figure 7.1.

7.2. Homogeneously Dispersed CD95L in Membranes

The cell response of pancreatic cancer cells (PanD24) was first characterized on substrates with homogeneously distributed CD95L. Therefore, biotinylated DOPE-

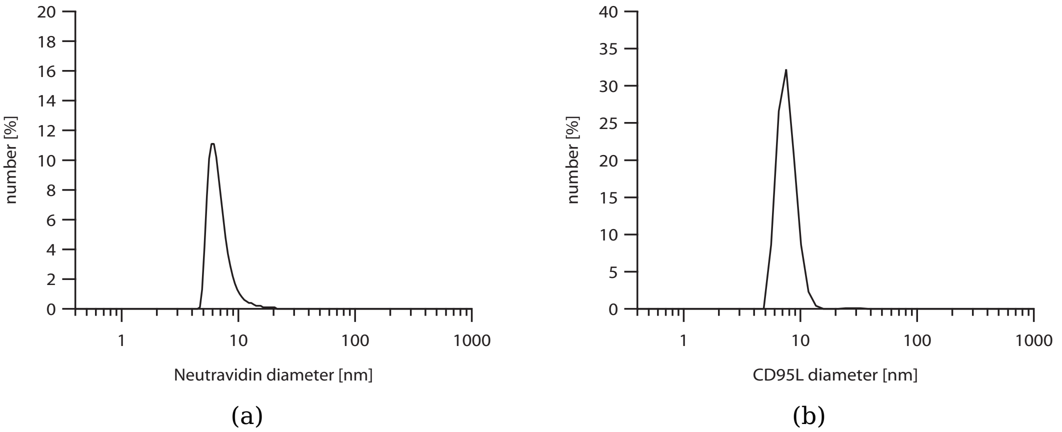

(a) (b)

Figure 7.2.: Size distribution of (a) Neutravidin and (b) CD95L measured by light scattering of the stock solution.

btn lipids were incorporated into solid supported DOPC membranes and acted as anchor sites for Neutravidin–biotin bridged ligand molecules. Figure 7.1 shows a schematic view of such monomerly dispersed CD95L membranes. The lateral density of ligand molecules was regulated via the concentration ρ_{btn} of biotinylated anchor lipids which have an equidistant distribution within the supported membrane. Neutravidin, a deglycosylated derivate of avidin, acts as bridging molecule. It exhibits four equivalent binding sites with an exceptionally high affinity to biotin (McMahon, 2008). The crystal structure of avidin (Pugliese et al., 1993) predicts two pairs of binding pockets. The distance between biotin binding pockets of one pair is $20\,\text{Å}$. The two pairs are located on opposite faces of the protein, which facilitates the simultaneous binding to the biotinylated supported membrane and to an opposing ligand molecule. The dissociation constant ($K_d = 1.3 \times 10^{-15}\,\mathrm{M}$) of Neutravidin is indistinguishable from that of avidin (Hiller et al., 1987) and ensures a stable binding of ligand molecules. The diameter of Neutravidin molecules was determined with a Zetasizer Nano (Malvern Instruments, Herrenberg, Germany) to be $6.9\,\mathrm{nm}$. Figure 7.2a shows the number distribution plotted for the particle diameter for Neutravidin. Preparing supported membranes with the closest packed Neutravidin layer requires at least $1.6\,\mathrm{mol\%}$ DOPE-btn lipid anchors within the remaining DOPC matrix. Higher DOPE-btn concentrations will only affect the binding stoichiometry of the second binding pocket. Fenz et al. (2009) demonstrated that $5\,\mathrm{mol\%}$ DOPE-btn concentration saturates both binding pockets of Neutravidin facing the substrate. In this thesis, all membranes with DOPE-btn concentrations above $2\,\%$ revealed comparable results. Thus, the smallest possible ligand distance of CD95L was attributed to be $6.9\,\mathrm{nm}$. As presented in Figure 7.2b, the average diameter of the biotinylated CD95L-T4-btn ligand was measured to be $\sim 7.7\,\mathrm{nm}$, but estimated to be a round particle. Since CD95L-T4-btn has an elongated shape with a flexible biotin tag attached, the length of the longitudinal protein axis and the lateral protein axis deviate from the average particle diameter. Therefore it was assumed that each CD95L-T4-btn molecule occupies one distal binding pocket of Neutravidin.

In this thesis, supported DOPC membranes with DOPE-btn content of $5\,\mathrm{mol\%}$, $2\,\mathrm{mol\%}$, $1\,\mathrm{mol\%}$, $0.5\,\mathrm{mol\%}$, and $0.1\,\mathrm{mol\%}$ were prepared. After coupling of CD95L-T4-btn, the membranes showed a monomerly dispersed CD95L distance of $<6.9\,\mathrm{nm}$, $7.7\,\mathrm{nm}$, $10.4\,\mathrm{nm}$, and $24.5\,\mathrm{nm}$, respectively. Figure 7.3 presents confocal images of pancreatic cancer cells on CD95L modified substrates. PanD24 cells were stained for actin (green) and DNA (blue) after fixation. Each cell is shown in a three-dimensional shape reconstruction in a tilted, side, and top view. Contrary to their non adherent, suspended cell line behavior in cell culture, PanD24 cells were rapidly adherent within $3\,\mathrm{min}$ on CD95L coated substrates. Reference samples of pure DOPC, and Neutravidin substrates without CD95L coating showed no significant cell binding. The top view in Figure 7.3a shows a prominent cell spreading on $6.9\,\mathrm{nm}$ spaced CD95L substrates with many star-like, short filopodia. The situation changes for PanD24 cells on wider gaped, i.e. $d = 24.5\,\mathrm{nm}$, CD95L substrates (Figure 7.3b). Cells form a large network of long, branched filopodia, whereas the cell body remains rather compact, but extremely flattened. RICM images of the adhesion area revealed a circular cell spreading without preferential direction in cell growth. The overlay in Figure 7.4 indicates the region between adhesion area of the cell body (solid lines) and the outer rim of the filopodia (dashed lines) for PanD24 cells adherent on $6.9\,\mathrm{nm}$ spaced CD95L substrates after $2\,\mathrm{h}$. The average width of the filopodia rim was $4.6\,\mathrm{\mu m}$. Corresponding fluorescence images (Figure 7.4, bottom row) of DNA stained cells showed clearly fragmented cell nuclei, indicating an apoptotic cell stage.

The temporal evolution of PanD24 adhesion areas on membranes with varying ligand densities is presented in Figure 7.5a together with control measurements. All PanD24 cancer cells which were exposed to CD95L initiated cell adhesion. The cancer cells spreading was most prominent on membranes with densely packed ligands ($<6.9\,\mathrm{nm}$). The average adhesion area remained for more than $3\,\mathrm{h}$ larger than $250\,\mathrm{\mu m}^2$, albeit cells already became apoptotic. Cancer cells on CD95L displaying membranes with larger ligand distances ($>10.9\,\mathrm{nm}$) showed adhesion areas below $150\,\mathrm{\mu m}^2$. Adherent PanD24 cells on membranes with low CD95L densities showed a branched network of filopodia, as presented in Figure 7.3b for a spread cancer cell on $24.5\,\mathrm{nm}$ spaced CD95L membranes. A different adhesion behavior revealed cancer cells on $7.7\,\mathrm{nm}$ spaced substrates. Here, the adhesion area also reached $150\,\mathrm{\mu m}^2$, but nearly all cells detached from the surface after around $2\,\mathrm{h}$. This observation was substantiated by the percentage of adherent cells shown in Figure 7.5c. More than $40\,\%$ of cancer cells remained adherent for over $3\,\mathrm{h}$ on the other CD95L-membranes. In contrast, PanD24 cells on membranes with $7.7\,\mathrm{nm}$ spaced CD95L showed a clear

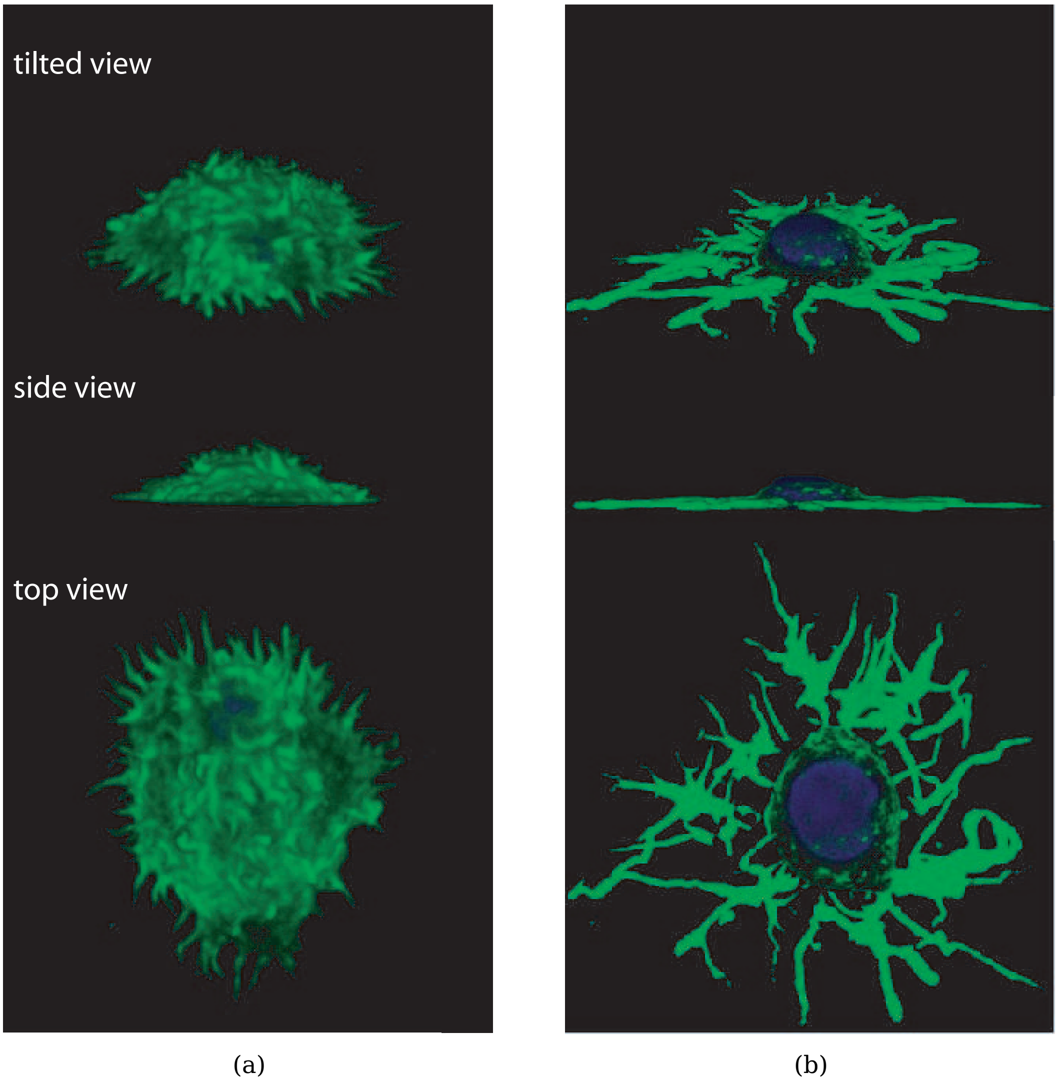

(a) (b)

Figure 7.3.: Confocal images of pancreatic cancer cells on CD95L decorated membranes after three–dimensional shape reconstruction. Cells were stained after $10\,\mathrm{min}$ incubation for actin (green) and DNA (blue). The average CD95L ligand distance on the supported membrane was (a) $6.9\,\mathrm{nm}$, and (b) $24.5\,\mathrm{nm}$.

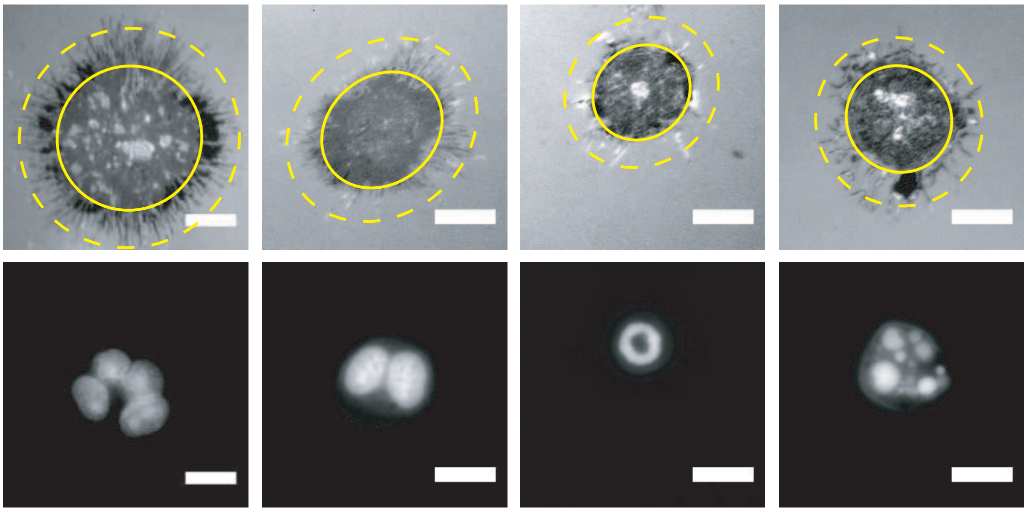

Figure 7.4.: RICM images of pancreatic cancer cells on dense CD95L substrates after 2 h. All scale bars are 10 µm.

decrease in the number of adherent cells. After around 2 h, the number of adherent cells and their respective adhesion area did not discriminate significantly from cells on pure DOPC substrates. On pure DOPC membranes the percentage of adherent cells remained always below 15 % with an average adhesion area below $50\,\mu\mathrm{m}^2$.

The efficiency of bound CD95L to trigger apoptosis was evaluated from the number of cells that became apoptotic after contact with CD95L modified membranes. Therefore, cancer cells were stained for DNA with the fluorescence marker DRAQ5, and the shape of the cell nucleus was analyzed for apoptotic characteristics. Only cells that showed cyclic DNA condensation or fragmented or collapsed cell nuclei were counted as dead. This may have caused a subjective underestimation of the apoptosis rate, but this routine was systematically conducted for all samples presented in this thesis. A different apoptosis marker specific to the early signaling pathway, e.g. caspase 3, may facilitate more accurate apoptosis detection. Figure 7.5c shows the percentage of apoptotic cells for CD95L samples plotted over time. The solid line represents Hill fits, i.e.,

$$H(t) = \text{base} + \frac{\text{maximum} - \text{base}}{1 + \left[\frac{\text{halftime}}{t}\right]^{\text{rate}}}, \tag{7.1}$$

of the measured data points (markers). For cells on pure DOPC membranes, an increase of dead cancer cells is indicated after 3 h, since the cell medium conditions (pH, CO_2 concentration) for the small sample volume became problematic for longer incubation times. As a control for apoptosis, PanD24 cells were subjected to high concentrations ($1\,\mu\mathrm{g\,ml}^{-1}$) of soluble hsCD95L on DOPC membranes. (Kleber et al.,

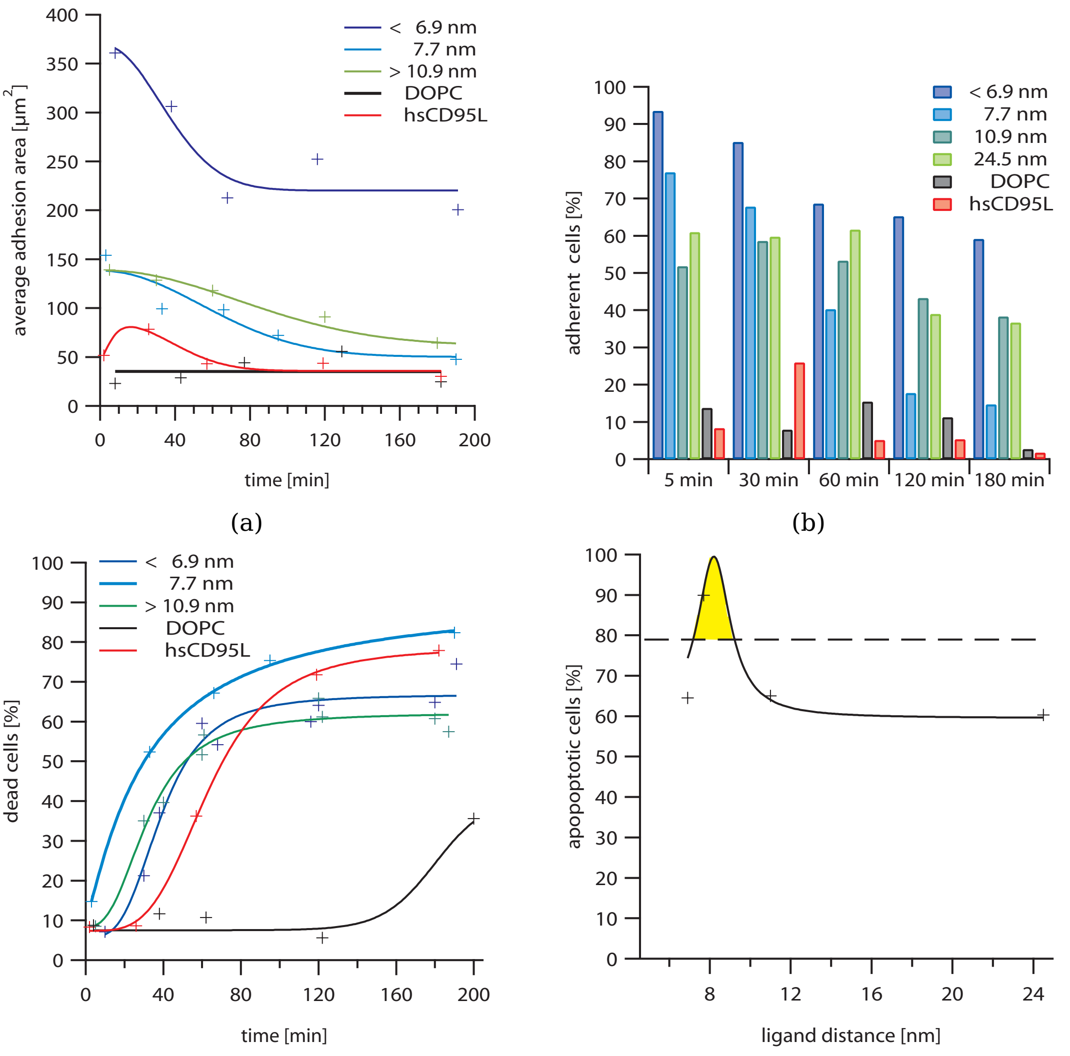

(a) (b)

(c) (d)

Figure 7.5.: Temporal plots of (a) average adhesion area, (b) percentage of adherent cells, (c) percentage of apoptotic cells, and (d) the maximum level of cells that became apoptotic for pancreatic cancer cells on CD95L coated membranes with varying ligand density.

2008) reported that hsCD95L triggers apoptosis in human glioma cells already at low concentrations ($10\,\mathrm{ng\,ml^{-1}}$). In this thesis, $78\,\%$ of PanD24 cells showed apoptosis after $3\,\mathrm{h}$ of incubation with hsCD95L. As shown in Figure 7.5b, these cells also became adherent within the first $30\,\mathrm{min}$, but detached completely from the DOPC membrane after $1\,\mathrm{h}$. The percentage of dead PanD24 cells on membranes with densely packed CD95L ($<6.9\,\mathrm{nm}$) reached a maximum apoptosis level of $65\,\%$. A similar cancer cell response was observed for wider spaced CD95L samples ($>10.9\,\mathrm{nm}$) with a maximum apoptosis level of $\sim 60\,\%$. PanD24 cells on membranes with $7.7\,\mathrm{nm}$ spaced CD95L revealed a different behavior, since the maximal amount of apoptotic cells reached up to $89\,\%$.

In Figure 7.5d the levels of apoptotic cells is plotted against the CD95L spacing. The apoptosis level of soluble hsCD95L is indicated as a dashed line. For hsCD95L, apoptotic cancer cells could form the death inducing signaling complex (DISC) on the complete cell surface, whereas on cells subjected to membrane bound CD95L the DISCs were formed only at the adhesion areas below the cells. A reduced apoptosis level for cells on membrane bound CD95L is therefore assigned to the effectively lower concentration of accessible ligands. To trigger the transduction of the apoptotic signal, oligomerization of CD95 is required (Krammer, 2000). Since trimeric CD95L interacts with three CD95 molecules, but fails to activate apoptosis efficiently, it has been suggested that CD95 activation requires more trimeric CD95L-CD95 complexes (Henkler et al., 2005). The high apoptosis triggering efficiency of $89\,\%$ for PanD24 cancer cells on $7.7\,\mathrm{nm}$ spaced CD95L substrates suggests ideal ligand spacing for CD95 oligomerization. The region of maximal apoptosis triggering is estimated in Figure 7.5d by a Gaussian distribution around the ideal ligand density. In agreement with the particle size of CD95L-T4-btn ($7.7\,\mathrm{nm}$) the optimal ligand spacing for CD95L-CD95 cluster formation lies between $7.2\,\mathrm{nm}$ to $9.2\,\mathrm{nm}$.

7.3. Membranes with CD95L-Domains

The effect of latterly confined CD95L-domains on the response of PanD24 was evaluated on supported membranes displaying functional nano-domains that are presented in Subsection 5.7.3. The domains were composed of $33\,\mathrm{mol\%}$ fluorinated M5btnFL17 lipid mixtures surrounded by $67\,\mathrm{mol\%}$ DOPC lipids and showed an average area of $0.18\,\mathrm{\mu m^2}$, i.e., a mean diameter of $0.48\,\mathrm{\mu m}$, the inter-domain distance a of $1\,\mathrm{\mu m}$, and contained $5\,\%$ of biotinylated btnFL17 lipids. Domains that were modified with CD95L-T4-btn were estimated to have a ligand distance of $\sim 6.9\,\mathrm{nm}$ and carry ~ 3800 CD95L molecules. A fluorescent image of CD95L-domains that are visualized by TexasRed-labeled Neutravidin is presented in Figure 7.6a. PanD24 cells on membranes with CD95L modified domains became immediately adhesive within $3\,\mathrm{min}$. Figure 7.6(b–c) shows RICM images of the adhesion area after $30\,\mathrm{s}$ and $75\,\mathrm{s}$. The ad-

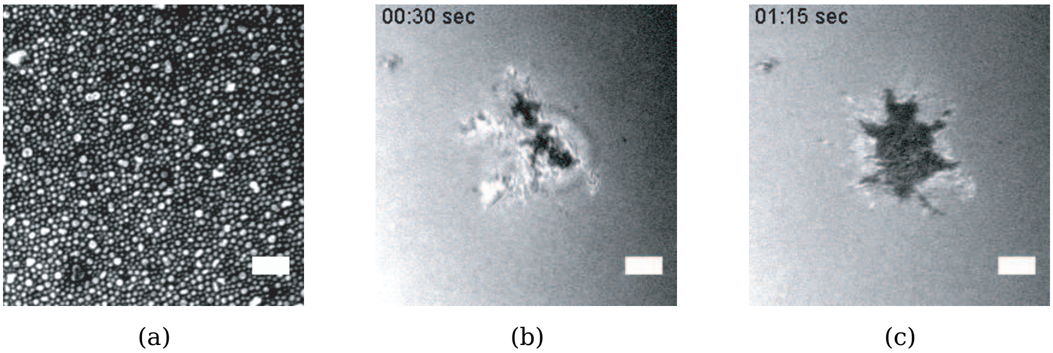

(a) (b) (c)

Figure 7.6.: (a) Fluorescence image of CD95L-domains labeled with Neutravidin-TexasRed. (b) RICM images of adherent PanD24 at the same area after $30\,\mathrm{s}$ and (c) $75\,\mathrm{s}$. Scale bars are $5\,\mu\mathrm{m}$.

Figure 7.7.: RICM images of pancreatic cancer cells on fluorinated domains functionalized with CD95L after $15\,\mathrm{min}$. All scale bars are $10\,\mu\mathrm{m}$.

hesion behavior of PanD24 on membranes exposing CD95L-domain revealed a striking difference from that on homogeneously dispersed CD95L-membranes. Instead of an isotropic, circular spreading of the cell body (Section 7.2), CD95L-domain substrates induce a preferential direction of cell spreading. Within the first few minutes, PanD24 cells form star like fingers and continue to grow in spindle-like shapes. Figure 7.7 presents typical RICM images of PanD24 adhesion areas after $15\,\mathrm{min}$. The adhesion areas of the cancer cells were found to be around $400\,\mu\mathrm{m}^2$ which is comparable to PanD24 cells on membranes with homogeneously distributed CD95L and the same ligand distance ($< 6.9\,\mathrm{nm}$). The shape of the cell body for adherent PanD24 cells on domains became elongated after $\sim 3\,\mathrm{min}$ and cells grew in a spindle-like structure presenting a rim of filopodia around the cell body. The overlaid ellipsoids (solid line) in Figure 7.7 along the contour line of the cell body had main-axis ratios below 0.5, whereas those presented in Figure 7.4 for PanD24 cells on homogeneously distributed CD95L membranes were nearly circular with main-axis ratios close to 1. For more elongated PanD24 cells, the growth direction

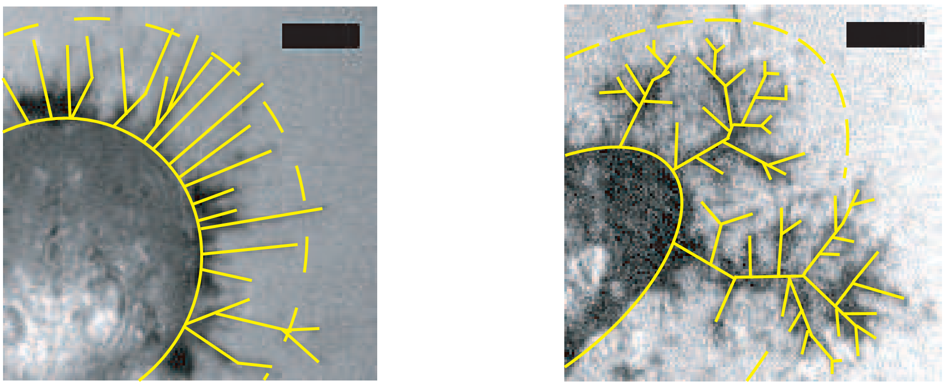
(a) (b)

Figure 7.8.: Zoom in of RICM images showing filopodia of pancreatic cancer cells on membranes with (a) isotropic CD95L distribution, and (b) discrete CD95L-domains after $15\,\mathrm{min}$ cell contact. All scale bars are $5\,\mu\mathrm{m}$.

splits after $\sim 22\,\mu\mathrm{m}$ into Y–shaped directions. Although a detailed study on the apoptotic response of PanD24 on membranes with incorporated domains is still missing, first experiments indicated a similar apoptosis efficiency analog to PanD24 cells on membranes with homogeneously distributed, $6.9\,\mathrm{nm}$ spaced CD95L (Figure 7.5c).

The difference of the adhesion area symmetry for PanD24 cells on domains was further substantiated by the shape of the filopodia around the cell body. Figure 7.8 presents a detailed view of the filopodia rim of pancreatic cancer cells on homogeneous, $6.9\,\mathrm{nm}$ spaced CD95L substrates and on CD95L functionalized domains. The filopodial structure is highlighted with yellow lines. The width of the filopodia from the contour line of the cell body (solid line) to the outer boundary line of the filopodia (dashed line) showed an average width of $6.3\,\mu\mathrm{m}$ for both types of membranes. Filopodia of PanD24 cells on homogeneously dispersed CD95L membranes were aligned parallel to each other and grew perpendicular to the cell boundary line. PanD24 cells on membranes displaying domains revealed a highly branched, fractal-like meshwork of filopodia. Here, the average distance between the branching points was $1.7\,\mu\mathrm{m}$ which is slightly larger than the inter–domain distance a ($1\,\mu\mathrm{m}$) of domains. The observed changes in cell shape and filopodia spreading suggest that supported membranes exposing functional domains can quantitatively control the specific cell response of cancer cells.

7.4. Conclusion

It was demonstrated that laterally confined ligand molecules for apoptosis (CD95L) induce specific cell responses in human, isolated pancreatic cancer cells (PanD24). The cancer cell response was analyzed on membranes displaying CD95L-modified domains, and on membranes with homogeneously dispersed CD95L in variable inter-CD95L distances. It was found that all pancreatic cancer cells exposed to CD95L became adherent, although PanD24 cells usually grow in suspension. PanD24 adhered on neutral DOPC membranes only if exposed to high concentrations ($1\,\mu\mathrm{g\,ml}^{-1}$) of soluble hsCD95L which resulted in apoptosis of $78\,\%$ of the cancer cells. CD95L-membranes with a ligand distance of $7.7\,\mathrm{nm}$ revealed an increased mortality of $89\,\%$, which would be an ideal distance for ligand-receptor (CD95L-CD95) oligomerization. The adhesion behavior of PanD24 changed on membranes with laterally confined domains. Whereas cancer cells on isotropic CD95L-membranes spread with circular cell shape, CD95L-domains induced an elongated, spindle-like cell spreading and Y-shaped branchings of the cell adhesion area. Furthermore, cancer cell filopodia on domain substrates form highly branched, fractal-like meshworks which was not observed for cancer cells on isotropic CD95L-membranes. The obtained results clearly indicate that supported membranes displaying functional, fluorinated lipid domains can control the adhesion behavior of cancer cells and act as confined signaling complexes to induce cancer cell apoptosis.

8. Conclusion

This thesis demonstrated the regulation of specific cell response with strongly correlated, functional domains embedded in solid supported model membranes. Biomimetic membranes were composed of a binary mixture of naturally occurring phospholipids and synthetically fluorinated lipids of variable chain lengths. It was demonstrated that fluorinated lipids form mono-dispersive domains that can be regulated for the domain size and the inter-domain correlation by the length mismatch between fluorocharbon and hydrocarbon chains. Supported membranes displaying laterally confined domains were modified with carbohydrates and protein ligands and could successfully activate specific cell responses of macrophages and cancer cells.

Chapter 4 presented a theoretical description of domain formation for a two-component lipid mixture to explain the experimentally observed narrow size distributions of domains. Under thermodynamic equilibrium conditions, it was shown that domains assimilate for a uniform equilibrium domain size. Within the theoretical framework of an equivalent dipole model, the formation of phase separated domains can be explained by the competing effect of electrostatic long-range forces, repulsive interfacial forces, and a constant background contribution. The lateral confinement of domains into periodic lattice structures induces an increase of the equilibrium radius which depends on the number density, and thus the inter-domain distance a, of fluorinated domains. In fact, pronounced inter-domain correlations observed by experiments can be generalized within the theoretical framework of a two-dimensional colloidal crystallization.

In Chapter 5 the molecular structure of fluorinated lipid domains was extensively characterized. Fluorinated lipids with $n = 10$, 13 and 17 carbons per chain were mixed into a DOPC lipid matrix and revealed mono-dispersive domains of a narrow size distribution, whose mean diameters were $\langle d_{\mathrm{FL10}} \rangle = 1.98\,\mu\mathrm{m}$, $\langle d_{\mathrm{FL13}} \rangle = 0.86\,\mu\mathrm{m}$, and $\langle d_{\mathrm{FL17}} \rangle < 0.50\,\mu\mathrm{m}$, respectively. Since the precise size determination of FL17 domains with fluorescence microscopy techniques was limited due to the optical resolution of the microscope, a high-resolution grazing-incidence X-ray diffraction (GIXD) measurement technique with an analyzer crystal setup was used to resolve the correlation length of fluorinated lipids. The fluorinated lipid chains are aligned perpendicular to the air water-interface and form a hexagonal lattice with the inter-chain distance of $5.64\,\mathrm{Å} \pm 0.01\,\mathrm{Å}$. The lateral scattering length of $0.32\,\mu\mathrm{m} \pm 0.03\,\mu\mathrm{m}$ for FL17 molecules even suggests that FL17 lipids form domains composed of a sin-

gle crystallite. Specular X-ray reflectivity measurements of monolayers transferred onto solid substrates yielded the length of fluorinated chains. The line tension surrounding the domains can be quantitatively calculated using the chain length mismatch between fluorinated and DOPC chains. Moreover, surface potential measurements allowed for the determination of the lateral dipole density projected to the membrane surface. The precise measurements of all the molecular structure parameters enabled calculation of the theoretical equilibrium radius of domains, which demonstrated excellent agreement with experimentally derived values for all fluorinated lipids used in this thesis.
Furthermore, a detailed analysis of the inter-domain correlation by Fourier-transform image analysis routines identified a six-fold hexagonal symmetry of domains. The inter-domain distance a increased with domain size, i.e., it was inversely proportional to the chain length of fluorinated lipids. Autocorrelation images of fluorinated domains yielded the radial distribution function $g(r)$ of domains. This enabled the calculation of the potential of mean force for the nearest neighbor domain positions. The derived spring constants of a harmonic inter-domain potential showed a highly repulsive domain interaction between two adjacent domains, which verifies that domains do not coalesce into bigger domains.

In Chapter 6, supported membranes displaying mannosylated micro-domains were used to evaluate the multivalent carbohydrate recognition by the mannose receptor in mouse macrophages. Cell shape analysis of adherent cells was performed by a combination of confocal fluorescence microscopy and a label free reflection interference contrast microscopy (RICM) technique used for dynamic tracking of cell response. A self-written image analysis routine allowed for a quantitative interpretation of the adhesion area and a reconstruction of the cell membrane topography in the vicinity of the cell-surface contact. Macrophages on mannosylated membranes showed a pronounced cell adhesion with distinct cell flattening and reduced membrane fluctuation amplitude above the domains. The clearance of FL10Man domains under macrophage adhesion areas furthermore confirmed a phagocytic activation of cells by mannose domains.

In Chapter 7, membranes were further modified with a specific ligand molecule (CD95L) to trigger apoptosis of pancreatic cancer cells. Both types of supported membranes displaying CD95L induced cell death within halftimes of $30\,\mathrm{min}$. Comparison of apoptosis rates between soluble hsCD95L and monomerly disperesed CD95L revealed an increased CD95L signal efficiency at an average ligand distance of $7.7\,\mathrm{nm}$. This distance is close to the measured CD95L diameter and is suggested to be an optimal distance for trimeric ligand-receptor interactions. Although the pancreatic cancer cells were cultured as suspended cell line, CD95L-modified membranes caused instantaneous adhesion and a pronounced cell spreading. The lateral confinement of CD95L into domains caused a clear spindle-like elongation of the cell adhesion areas and induced Y-shaped branchings of the cell body. The induced symmetry break of cell adhesion was substantiated by highly branched cancer cell filopodia on CD95L domains.

The obtained results demonstrated the successful design of functional lipid micro- and nano- domains that mimic the multivalent interactions in the cell plasma membrane. Compared to commonly used complex lipid mixtures, the presented molecular tuning strategy included synthetic fluorinated lipids which allow for a precise control of domain size, inter–domain correlation, and specific biological functions. The laterally confined domain patterns incorporated into supported membranes could activate specific cell spreading and cancer apoptosis. Thus, supported membranes exposing functional domains provide a sophisticated cell membrane model to study and control the specific cell response.

9. Outlook

The presented model system of supported membranes displaying fluorinated lipid domains holds much promise for the study of membrane-associated functions of specific target molecules.

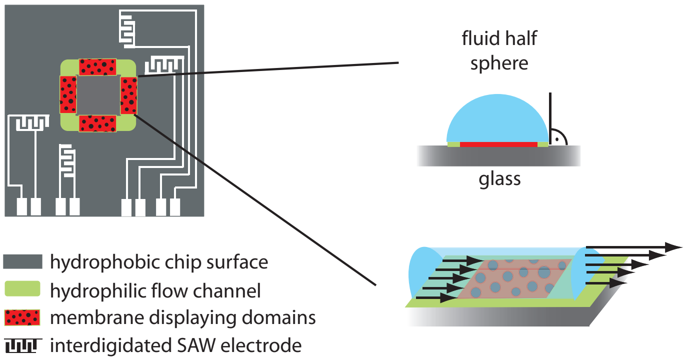

Figure 9.1.: Schematic illustration of a solid supported membrane transferred to a surface acoustic wave driven microfluidic device.

As demonstrated, fluorinated lipid domains embedded in supported membranes can precisely be regulated for domain size and inter-domain distance. Modifying them with specific target molecules enables control of the number and the lateral localization of the target molecules. This information allows for a quantitative calculation of the interaction forces of target molecules or identification of cooperative effects. For instance, the strength of selectin-carbohydrate bonds can significantly enhance under tensile mechanical stress (Thomas, 2008). These so-called catch bonds are known to mediate the tethering and rolling of leukocytes on vascular surfaces (Marshall et al., 2003; Korn and Schwarz, 2006). The use of laterally confined lipid domains modified with a defined number and sequence of carbohydrate epitopes allows for specific regulation of the number of bonds and calculation of the local adhesion strength of cells in hydrodynamic flow.

A promising realization for these dynamic cell experiments needs to combine structured supported membranes with an elaborate microfluidic system. Commonly used parallel-plate flow chambers are dependent on external pumping mechanism. This most often requires large volumes of cell suspension or a large amount of rare and thus expensive biological substances. Recently, Wixforth et al. (2004) presented a planar microfluidic system driven by surface acoustic waves (SAW) which enables investigation of cell behavior under low Reynolds numbers with a small sample volume of only $10\,\mu\mathrm{l}$. The maximum applicable shear rate of $20\,000\,\mathrm{s}^{-1}$ covers the whole physiological and pathological range (Schneider et al., 2008). Figure 9.1 presents a schematic illustration of a microfluidic SAW-setup combined with supported membranes displaying functional domains.

A. Appendix

A.1. Synthesis of Fluorinated Lipids

Synthetic pathway of FL10Man

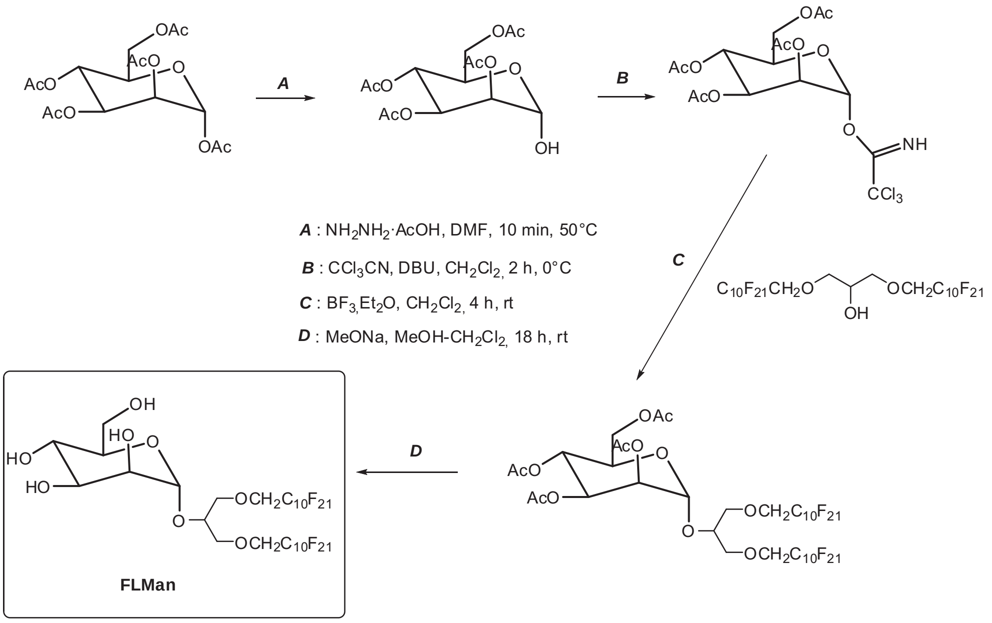

Figure A.1.: Synthetic pathway of FL10Man.

A) A solution of 1,2,3,4,6-penta-O-acetyl-D-mannopyranose ($3.5\,\mathrm{g}$, $9\,\mathrm{mmol}$) and of $NH_2NH_2 \cdot EAcOH(1.07\,\mathrm{g}$, $1.7\,\mathrm{mmol})$ in DMF ($10\,\mathrm{ml}$) was stirred for $10\,\mathrm{min}$ at $50\,°\mathrm{C}$ and after cooling to $20\,°\mathrm{C}$, diluted with $100\,\mathrm{ml}$ of EtOAc. The solution was washed with water, aqueous $NaHCO_3$, aqueous NaCl, dried ($MgSO_4$), and evaporated *in vacuo*.

Yield: $95\,\%$.

^{1}H-NMR($CDCl_3$): 1.95, 2.01, 2.04, 2.11 ($COCH_3$); 4.03–4.07 (1H); 4.20.4.23 (2H); 5.14.5.26 (2H); 5.35 (*d*, 1H, Hα, β);
^{13}CNMR($CDCl_3$): 20.59, 20.63, 20.64, 20.79 ($COCH_3$); 62.74 (C6); 66.43, 67.96, 69,16, 70,59 (C2–5); 92.07 (C1); 169.79, 169.84, 170.05, 170.58 ($COCH_3$).

B) A solution of the oil hemiacetal (500 mg, 1.44 mmol) in dry CH_2Cl_2 (5 ml) stirred under argon, was treated successively with CCl_3CN (2.1 g, $d = 1.44$, 1.5 ml, 14.5 mmol) and 1,8-diazabicyclo[5,4,0]undec-7-ene (DBU; 22 mg, $d = 1.019$, 22 µl, 0.14 mmol) at 0 °C. After being stirred for 2 h at 0 °C, the mixture was directly chromatographed on SiO_2 in 1:1 hexane-EtOAc ($R_f = 0.26$). The product was isolated as a white solid.

Yield 64

^{1}H-NMR ($CDCl_3$): 1.93, 1.96, 2.00, 2.12 (CO$\underline{CH_3}$); 4.05-4.25 (3H); 5.32 (2H); 5.39 (d, 1H, H2); 6.21 (d, 1H, H1); 8.81 (s, 1H, NH);
^{1}3C-NMR ($CDCl_3$): 20.25, 20.41, 20.63, 20.67 (CO$\underline{CH_3}$); 61.75 (C6); 65.10, 67.57, 68.55, 70.96 (C2-5); 90.24 (CCl_3); 94.24 (C1); 159.33 (C=NH); 169.29, 169.36, 169.45, 170.18 ($\underline{C}$OCH3).

C) To a solution of FL10 (86.5 ìmol, 1 eq) and trichloroacetamidate ($M = 491$, 0.042 g, 86.5 µmol, 1 eq) in dry dichoromethane with molecular sieves (AW-300) was added $BF_3 \cdot Et_2O$ (4 µl, 33 µmol, 0.3 eq) at room temperature. After 4 h the solution was neutralized with triethylamine, filtrated and evaporated under reduced pressure.

D) To a solution of fluorolipid acetylated mannose (176 µmol) in dry methanol / dichloromethane (40 ml; 3:1 v:v) was added sodium methoxide (40 mg, 0.74 mmol). After stirring overnight, the solution was neutralized with Amberlite IR120 (H^+), filtered, and absorbed on silica gel. Flash chromatography ($CHCl_3$/methanol/water 85:15:1 to 80:20:2 v/v/v) afforded FLMan as amorphous solid after lyophilization from water/dioxane.

Yield 38 %.

^{1}H-NMR (CD_3OD): 3.4Ű3.7 (11H); 3.84 (t, 4H); 5.21 (*d*, 1H); elemental analysis: $C_{31}H_{20}F_{42}O_8$, th. % C: 28.24, % H: 1.53, exp. % C: 28.62, % H: 1.58.

Synthetic pathway of btnFL17

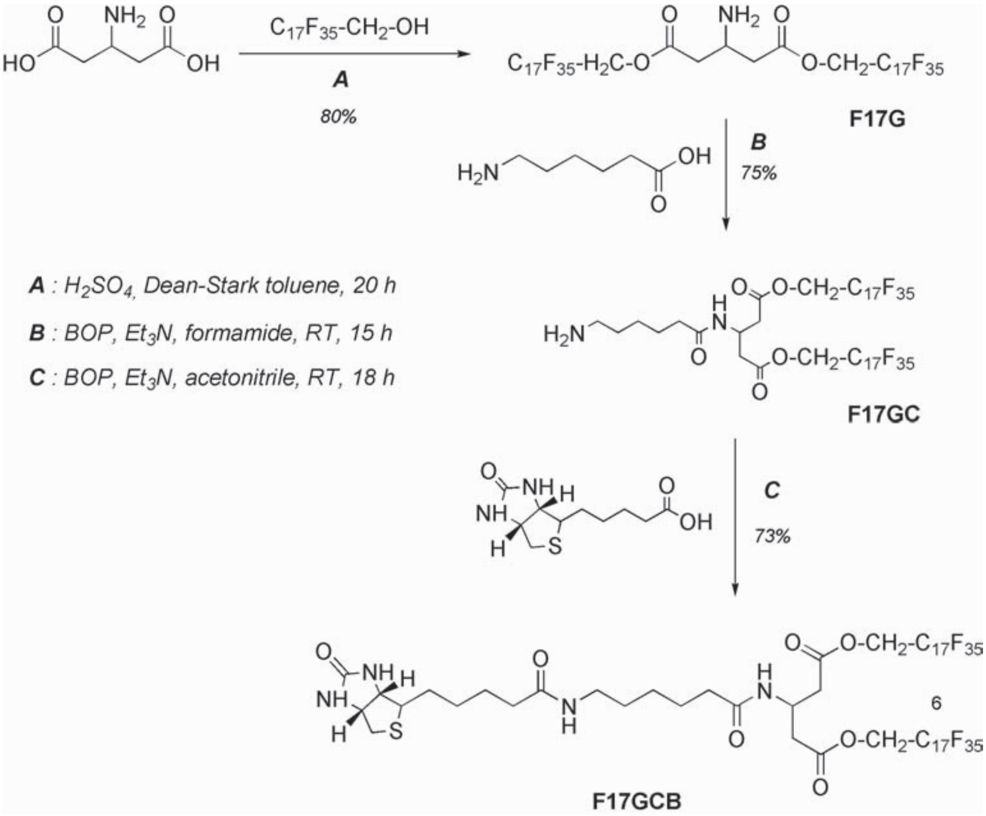

Figure A.2.: Synthetic pathway of btnFL17.

The synthesis of the target biotinylated fluorinated lipid btnFL17 (F-tag-glutamic-caproic-biotin) was performed by a step-by-step strategy similar to peptidic coupling. In the first step (A) the corresponding F-tag glutamic diester F17G was obtained using the Fisher esterification conditions. Then, 6-aminocaproic acid (B) and biotin (C) were coupled to F17G and F17GC, respectively using BOP as peptidic coupling agent. The final product was obtained in a good overall yield.

A.2. Chemical Structure of Lipids

The chemical structures of the unsaturated 1,2-dioleo-*sn*-glycero-3-phophocholine (DOPC) carrying cis-conformation at carbon position number 9 on both alkyl chains, the head group modified 1,2-dioleoyl-*sn*-glycero-3-phosphoethanolamine-N-(cap biotinyl) lipid DOPE-btn, and the used fluorescent tracer lipid 1,2-dihexadecanoyl-*sn*-glycero-3-phosphoethanolamine triethylammonium salt (Texas Red®-DHPE) are presented in Figure A.3.

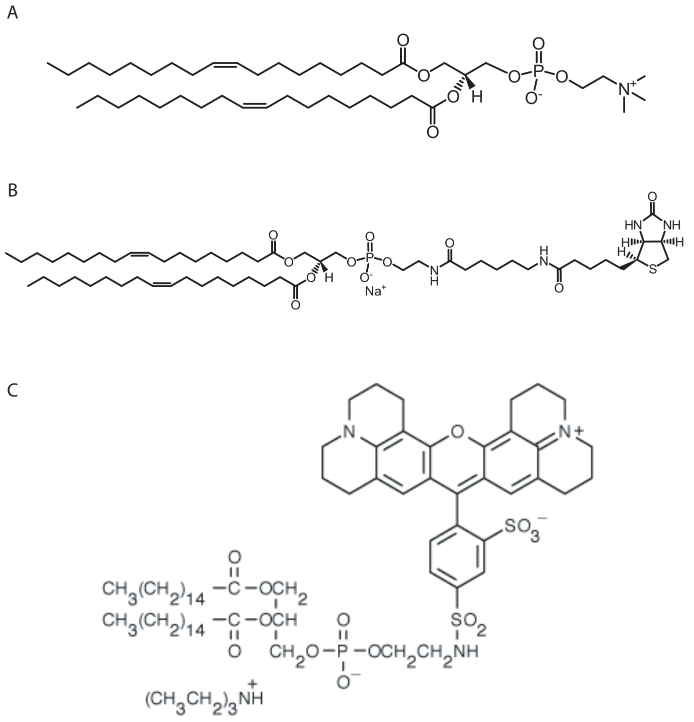

Figure A.3.: Chemical structures of (A) DOPC, (B) DOPE-btn, and (C) the fluorescence marker tagged lipid Texas Red®-DHPE.

A.3. Isotherms of Fluorinated Lipids in Fluorous Solvents

Compression isotherms were recorded at $20\,°\mathrm{C}$. The head group modified acFL17 molecules were dissolved in 1:1 Freon® 113: chloroform and btnFL17 in 1:1 methylperflurobutan : chloroform solution for spreading. Both molecules showed a collapse of the Langmuir film already at low surface pressure $\Pi < 20\,\mathrm{mN\,m^{-1}}$.

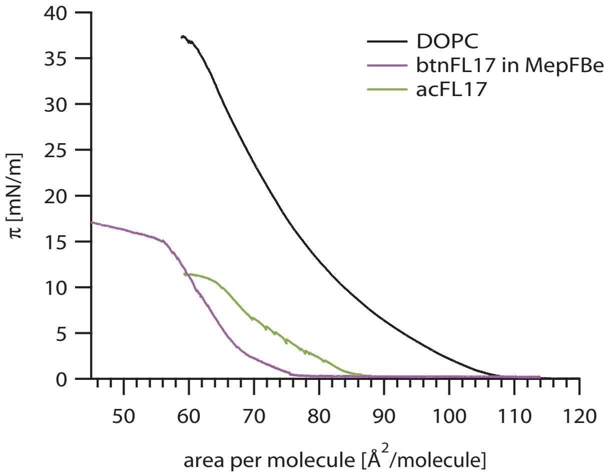

Figure A.4.: Langmuir isotherms of btnFL17, and acFL17 used for spreading area correction.

A.4. Reflectifity curves

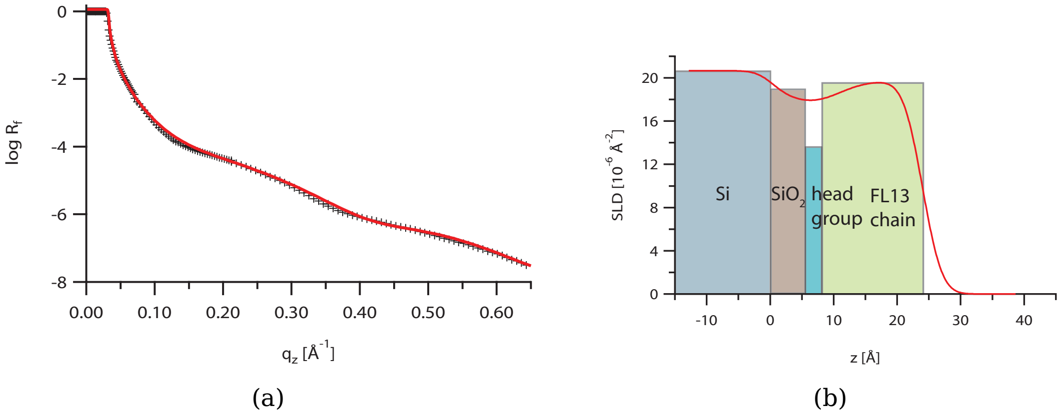

(a)

(b)

Figure A.5.: (a) Measured reflectifity curve (black datapoints) for FL13 monolayer at the air–Si interface and model based fit (red line). (b) Scattering length density (SLD) profile of the best fitted model along z-direction. Bars in the background indicate the layer box model.

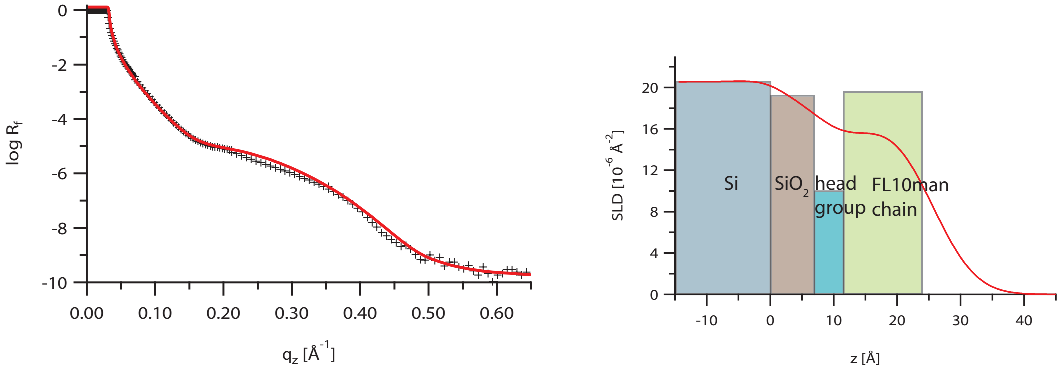

(a) (b)

Figure A.6.: (a) Measured reflectifity curve (black datapoints) for FL10man monolayer at the air–Si interface and model based fit (red line). (b) Scattering length density (SLD) profile of the best fitted model along z-direction. Bars in the background indicate the layer box model.

Abbreviations

POPC	1-palmitoyl-2-oleoyl-*sn*-glycero-3-phosphocholine
DOPC	1,2-dioleoyl-*sn*-glycero-3-phosphocholine
diPhyPC	1,2-diphytanoyl-*sn*-glycero-3-phosphocholine
SOPC	1-stearoyl-2-oleoyl-*sn*-glycero-3-phosphocholine
chol	cholesterol
DOPE-btn	1,2-dioleoyl-*sn*-glycero-3-phosphoethanolamine-N-(cap biotinyl)
TexasRed®-DHPE	1,2-dihexa-decanoyl-*sn*-glycero-3-phosphoethanolamine triethylammonium salt
TRITC	tetramethylrhodamine-5-(and 6)-isothiocyanate
ODTMS	n-octadecyltrimethoxysilane
Freon®113	1,1,2-trichloro-1,2,2-trifluoroethane
TRIS	tris(hydroxymethyl)aminomethane
PBS	phosphate buffered saline
FBS	fetal bovine serum
DMEM	Dulbecco's Modified Eagle's Medium
LB	Langmuir-Blodgett
LS	Langmuir-Schäfer
RICM	reflection interference contrast microscopy
SUV	small unilamellar vesicle
GUV	giant unilamellar vesicle
ITO	indium tin oxide
DKFZ	Deutsches Krebsforschungszentrum
ESRF	European Synchrotron Radiation Facility
SLD	scattering length density
GIXD	grazing incidence X-ray diffraction
SAXS	small angle X-ray scattering
N.A.	numerical aperture
I.N.A.	illuminating numerical aperture
PSF	point spread function
DPD	dissipative particle dynamics
SAW	surface acoustic waves

CRD	carbohydrate recognition domains
CTLDs	C–type lectin–like domains
MR	mannose receptor
FN	fibronectin
Cys	cysteine
BSA	bovine serum albumin
CD95L	cluster of differentiation 95 ligand
TNF	tumor necrosis factor
DISC	death-inducing signaling complex

Bibliography

F. Abelès. La théorie générale des couches minces. *Journal de Physique et le Radium*, 11(7):307–309, 1950. [48]

M. Abercrombie and E. J. Ambrose. Interference microscopy studies of cell contacts in tissue culture. *Experimental Cell Research*, 15:332–345, 1958. [72]

M. D. Abramoff, P. J. Magelhaes, and S. J. Ram. Image processing with ImageJ. *Biophotonics International*, 11(7):36–42, 2004. [13, 76, 80]

J. Als-Nielsen and D. McMorrow. *Elements of Modern X-Ray Physics*. John Wiley & Sons Inc., Chichester, UK, 2001. [46]

J. Als-Nielsen, D. Jacquemain, K. Kjaer, F. Leveiller, M. Lahav, and L. Leiserowitz. Principles and applications of grazing incidence X-ray and neutron scattering from ordered molecular monolayers at the air-water interface. *Physics Reports*, 246: 251–313, 1994. [45]

D. Andelman, F. Broçhard, and J. Joanny. Phase transitions in Langmuir monolayers of planar molecules. *The Journal of Chemical Physics*, 6:3673–3681, 1987. [35, 53]

T. Angata, Els, and E. C. M. Brinkman-Van der Linden. I–type lectins. *Biochim Biophys Acta - General Subjects*, 1572(2-3):294–316, 2002. [70]

L. Belloni. Colloidal interactions. *Journal of Physics: Condensed Matter*, 12:R549–R587, 2000. [27]

H. Brockman. Dipole potential of lipid membranes. *Chemistry and Physics of Lipids*, 73:57–79, 1994. [53]

C. W. Bunn and E. R. Howells. Structures of molecules and crystals of fluorocarbons. *Nature*, 174:549–551, 1954. [45, 50]

J. A. Cape and G. W. Lehman. Magnetic domain structures in thin uniaxial plates with perpendicular easy axis. *Journal of Applied Physics*, 42(13):5732–5756, 1971. [27]

C. Chang, Y. Mingke, P. Wu, T. Jiang, H. Yu, R. Widelitz, and C. Chuong. Sculpting skin appendages out of epidermal layers via temporally and spatially regulated apoptotic events. *Journal of Investigative Dermatology*, 122:1348–1355, 2004. [89]

M. K. Chaudhury and M. J. Owen. Adhesion hysteresis and friction. *Langmuir*, 9(1): 29–31, 1993. [51]

Q. Chu, M. S. Yu, and D. P. Curran. New fluorous/organic biphasic systems achieved by solvent tuning. *Tetrahedron*, 63:9890–9895, 2007. [19]

P. Croce and L. Névot. Sur l'etude des couches superficielles monoatomiques par réflexion 'rasante' (spéculaire ou diffuse) de rayons X, par la méthode de l'empilement 'sandwich'. *Journal of Applied Crystallography*, 8:304–314, 1975. [47]

A. S. G. Curtis. The mechanism of adhesion of cells to glass. *The Journal of Cell Biology*, 20:199–215, 1964. [72]

J. Daillant and A. Gibaud. *X-Ray and Neutron Reflectivity: Principles and Applications*. Springer, Berlin, 1999. [48]

R. de Koker and H. M. McConnell. Circle to dogbone: Shapes and shape transitions of lipid monolayer domains. *The Journal of Physical Chemistry*, 97(50):13419–13424, 1993. [31, 35, 36]

J. M. Deutch and F. E. Low. Theory of shape transitions of two-dimensional domains. *The Journal of Physical Chemistry*, 96(17):7097–7101, 1992. [32]

C. Dietrich, L. A. Bagatolli, Z. N. Volovyk, N. L. Thompson, M. Levi, K. Jacobson, and E. Gratton. Lipid rafts reconstituted in model membranes. *Biophysical Journal*, 80 (3):1417–1428, 2001. [3]

L. East and M. Isacke. The mannose receptor family. *Biochimica et Biophysica Acta - General Subjects*, 1572(2-3):364–386, 2002. [70, 71]

M. Edidin. The state of lipid rafts: From model membranes to cells. *Annual Review of Biophysics and Biomolecular Structure*, 32:257–283, 2003. [69]

P. Español and P. Warren. Statistical mechanics of dissipative particle dynamics. *Europhysics Letters*, 30(4):191–196, 1995. [36]

H. Feinberg, S. Park-Snyder, A. R. Kolatkar, C. T. Heise, M. E. Taylor, and W. I. Weis. Structure of a C–type carbohydrate recognition domain from the macrophage mannose receptor. *The Journal of Biological Chemistry*, 275(28):21539–21548, 2000. [71]

S. Fenz, R. Merkel, and K. Sengupta. Diffusion and intermembrane distance: Case study of avidin and E-cadherin mediated adhesion. *Langmuir*, 25(2):1074–1085, 2009. [91]

M. L. Fiani, J. Beitz, D. Turvy, J. S. Blum, and P. D. Stahl. Regulation of mannose receptor sysnthesis and turnover in mouse J774 macrophages. *Journal of Leukocyte Biology*, 64:85–91, 1998. [72]

G. L. Gaines. *Insoluble Monolayers at Liquid-gas Interfaces*. John Wiley & Sons Inc., 1st edition, 1966. [9]

R. E. Geer, D. A. Stenger, M. S. Chen, J. M. Calvert, and R. Shashidhar. X-ray and ellipsometric studies of self-assembled monolayers of fluorinated chlorosilanes. *Langmuir*, 10(4):1171–1176, 1994. [48]

C. Gege, M. F. Schneider, G. Schumacher, L. Limozin, U. Rothe, G. Bendas, M. Tanaka, and R. R. Schmidt. Functional microdomains of glycolipids with partially fluorinated membrane anchors: Impact on cell adhesion. *ChemPhysChem*, 5 (2):216–224, 2004. [3]

S. Gordon. Pattern recognition receptors: Doubling up for the innate immune response. *Cell*, 111:927–930, 2002. [72]

A. J. Gracía-Sáez and P. Schwille. Stability of lipid domains. *FEBS Letters*, 584(9): 1653–1658, 2010. [3]

S. Hakomori and Y. Igarashi. Functional role of glycosphingolipids in cell recognition and signaling. *The Journal of Biochemistry*, 118(8):1091–1103, 1995. [69]

J. P. Hansen and I. R. McDonald. *Theory of simple liquids*. Elsevier, London, 3rd edition, 2008. [27, 30]

E. Hecht. *Optics*. Addison Wesley, Amsterdam, 4th edition, 2001. [47, 74]

F. Henkler, E. Behrle, K. M. Dennehy, A. Wiscovsky, N. Peters, C. Warnke, K. Pfizenmaier, and W. H. The extracellular domains of FasL and Fas are sufficient for the formation of supramolecular fasl-fas clusters of high stability. *The Journal of Cell Biology*, 168(7):1087–1098, 2005. [96]

Y. Hiller, J. M. Gershoni, E. A. Bayer, and M. Wilchek. Biotin binding to avidin. *Biochemical Journal*, 248(1):167–171, 1987. [91]

P. J. Hoogerbrugge and J. M. V. A. Koelman. Simulating microscopic hydrodynamic phenomena with dissipative particle dynamics. *Europhysics Letters*, 19(3):155–160, 1992. [36]

Y. Hu, K. Meleson, and J. N. Israelachvili. Thermodynamic equilibrium of domains in a two-component Langmuir monolayer. *Biophysical Journal*, 91:444 – 453, 2006. [50]

H. Ibach. *Physics of Surfaces and Interfaces*. Springer, Berlin, 2006. [28]

J. N. Israelachvili. *Intermolecular & Surface Forces*. Academic Press, San Diego, 2nd edition, 1991. [23]

M. Iwamoto and Z. Ou-Yang. Shape deformation and circle instability in two-dimensional lipid domains by dipolar force a shape- and size-dependent line tension model. *Physical Review Letters*, 93(20):206101, 2004. [29]

K. Jacobson, E. D. Sheets, and R. Simson. Revisiting the fluid mosaic model of membranes. *Science*, 268(5216):1441–1442, 1995. [1]

K. Jacobson, O. G. Mouritsen, and R. G. W. Anderson. Lipid rafts: at a crossroad between cell biology and physics. *Nature Cell Biology*, 9(1):7–14, 2007. [1]

T. Kaindl, J. Oelke, A. Pasc, S. Kaufmann, O. Konovalov, S. S. Funari, A. Engel, U. Wixforth, and M. Tanaka. Regulation of adhesion behaviour of murine macrophage using supported lipid membranes displaying tunable mannose domains. *Journal of Physics: Condensed Matter*, 22:285102–11, 2010. [5, 43, 50]

E. Kalb, S. Frey, and L. K. Tamm. Formation of supported planar bilayers by fusion of vesicles to supported phospholipid monolayers. *Biochimica et Biophysica Acta - Biomembranes*, 1103(2):307–316, 1992. [23]

G. Karp. *Mollekulare Zellbiologie*. Springer, Berlin, 2005. [1]

D. J. Keller, J. P. Korb, and Mc. Theory of shape transitions in two-dimensional phospholipid domains. *The Journal of Physical Chemistry*, 91:6417–6422, 1987. [35]

W. Kern and D. A. Puotinen. Cleaning solutions based on hydrogen peroxide for use in silicon semiconductor technology. *RCA Review*, 31:187–206, 1970. [8]

K. Kjaer. Some simple ideas on X-ray reflection and grazing-incidence diffraction from thin surfactant films. *Physica B*, 198:100–109, 1994. [45]

S. Kleber, I. Sancho-Martinez, B. Wiestler, A. Beisel, C. Gieffers, O. Hill, T. Meinolf, W. Mueller, J. Sykora, A. Kuhn, N. Schreglmann, E. Letellier, C. Zuliani, S. Klussmann, M. Teodorczyk, H. Gröne, T. M. Ganten, H. Sültmann, J. Tüttenberg, A. Deimling, von, A. Regnier-Vigouroux, C. Herold-Mende, and A. Martin-Villalba. Yes and PI3K bind CD95 to signal invasion of glioblastoma. *Cancer Cell*, 13(3): 235–248, 2008. [94]

C. Korn and U. S. Schwarz. Efficiency of initiating cell adhesion in hydrodynamic flow. *Physical Review Letters*, 97(13):138103–4, 2006. [105]

P. H. Krammer. CD95’s deadly mission in the immune system. *Nature*, 407(6805): 789–795, 2000. [89, 90, 96]

I. Langmuir. The constitution and fundamental properties of solids and liquids. ii. liquids.1. *Journal of the American Chemical Society*, 39(9):1848–1906, 1917. [27]

B. L. Largent, K. M. Walton, C. A. Hoppe, Y. C. Lee, and R. L. Schnaar. Carbohydrate-specific adhesion of alveolar macrophages to mannose-derivatized surfaces. *The Journal of Biological Chemistry*, 259(3):1764–1769, 1984. [70]

C. Leteux, W. Chai, R. W. Loveless, C. T. Yuen, L. Uhlin-Hansen, Y. Combarnous, M. Jankovic, S. C. Maric, Z. Misulovin, M. C. Nussenzweig, and T. Feizi. The cysteine-rich domain of the macrophage mannose receptor is a multispecific lectin that recognizes chondroitin sulfates A and B and sulfated oligosaccharides of blood group Lewis^a and Lewis^x types in addition to the sulfated N-glycans of lutropin. *The Journal of Experimental Medicine*, 191(7):1117–1126, 2000. [70]

L. Limozin and K. Sengupta. Quantitative reflection interference contrast microscopy (RICM) in soft matter and cell adhesion. *ChemPhysChem*, 10(16):2752–2768, 2009. [73, 74, 76]

H. Lodish, A. Berk, Z. S. L., P. Matsudaira, D. Baltimore, and J. E. Darnell. *Molekulare Zellbiologie*. Spektrum Akademischer Verlag GmbH, Heidelberg, 4th edition, 2001. [1, 78]

M. Mammen, S. Choi, and G. M. Whitesides. Polyvalent interactions in biological systems: Implications for design and use of multivalent ligands and inhibators. *Angewandte Chemie International Edition*, 37(20):2754–2794, 1998. [2]

M. Markko. Applying stereological method in radiology. volume measurement. Master's thesis, University of Tartu, 2008. [13]

B. T. Marshall, M. Long, J. W. Piper, T. Yago, R. P. McEver, and C. Zhu. Direct observation of catch bonds involving cell-adhesion molecules. *Nature*, 423(6936): 190–193, 2003. [105]

A. Martin-Villalba. unpublished results in personal communication. [90]

A. Martin-Villalba, editor. *Die Rolle des Todesrezeptors CD95 (Fas) im ZNS*, Ruprecht-Karls-Universität Heidelberg, 2006. Medizinische Fakultät. [89]

H. M. McConnell. Theory of hexagonal and stripe phases in monolayers. *Proceedings of the National Academy of Sciences of the U.S.A.*, 86:3452–3455, 1986. [38, 68]

H. M. McConnell. Structures and transitions in lipid monolayers at the air-water interface. *Annual Review of Physical Chemistry*, 42:171–195, 1991. [29, 31, 32]

H. M. McConnell and R. de Koker. Note on the theory of the sizes and shapes of lipid domains in monolayers. *The Journal of Physical Chemistry*, 96(17):7101–7103, 1992. [32]

H. M. McConnell and R. de Koker. Equilibrium thermodynamics of lipid monolayer domains. *Langmuir*, 12(20):4897–4904, 1996. [33, 35]

H. M. McConnell and V. T. Moy. Shapes of finite two-dimensional lipid domains. *The Journal of Physical Chemistry*, 92(15):4520–4525, 1988. [31, 32]

H. M. McConnell, T. H. Watts, R. M. Weis, and A. A. Brian. Supported planar membranes in studies of cell-cell recognition in the immune system. *Biochim Biophys Acta - Reviews on Biomembranes*, 864(1):95–106, 1986. [22]

T. J. McIntosh, A. S. Sidney, P. Vierling, C. Santaella, and V. Ravily. Structure and interactive properties of highly fluorinated phospholipid bilayers. *Biophysical Journal*, 71:1853–1868, 1996. [50]

R. J. McMahon. *Avidin-biotin interactions*. Number 418 in Methods in molocular biology. Humana Press, Totowa, NJ-USA, 2008. [65, 91]

J. Mingins, D. Stigter, and K. A. Dill. Phospholipid interactions in model membrane systems. *Biophysical Journal*, 61:1603–1615, 1992. [53]

H. Möhwald. Phospholipid and phospholipid-protein monolayers at the air/water interface. *Annual Review of Physical Chemistry*, 41:441–476, 1990. [27]

H. Möhwald. *Handbook of Biological Physics*, volume 1, chapter 4, pages 161–211. Elsevier Science B. V., 1995. Phospholipid Monolayers. [53]

C. R. F. Monks, B. A. Freiberg, H. Kupfer, N. Sciaky, and A. Kupfer. Three-dimensional segregation of supermolecular activation clusters in T cells. *Nature*, 395:82–86, 1998. [2]

D. J. Müller and A. Engel. Atomic force microscopy and spectroscopy of native membrane proteins. *Nature Protocols*, 2(9):2191–2197, 2007. [2]

N. P. Mullin, K. T. Hall, and M. E. Taylor. Characterization of ligand binding to carbohydrate-recognition domain of the macrophage mannose receptor. *The Journal of Biological Chemistry*, 269(45):28405–13, 1994. [71]

K. Nag and N. K. K. M. W. Boland, C. Rich. Epifluorescence microscopic observation of monolayers of dipalmitoylphosphatidylcholine: dependence of domain size on compression rates. *Biochimica et Biophysica Acta - Biomembranes*, 1068:157–160, 1991. [35]

S. Nagata. Apoptosis by death factor. *Cell*, 88(3):355–365, 1997. [90]

A. Nelson. Co-refinement of multiple-contrast neutron/X-ray reflectivity data using motofit. *Journal of Applied Crystallography*, 39:273– 276, 2006. [48]

C. L. Nilsson, editor. *Lectines Analytical Technologies*. Elsevier, Amsterdam, 1st edition, 2007. [69]

P. Nollert, H. Kiefer, and Jähnig. Lipid vesicle adsorption versus formation of planar bilayers on solid surfaces. *Biophysical Journal*, 69(4):1447–1455, 1995. [22]

E. Nováková, K. Giewekemeyer, and T. Salditt. Structure of two-component lipid membranes on solid support: An x-ray reflectivity study. *Physical Review E*, 74: 051911–9, 2006. [48, 52]

J. Oelke. *Strongly Correlated Micro/Nano-Domains of Functional Lipids for Geometrical Control of Dynamic Cell Adhesion*. PhD thesis, Universität Augsburg, 2008. [43, 50]

J. Oelke, A. Pasc, A. Wixforth, O. Konovalov, and M. Tanaka. Highly uniform, strongly correlated fluorinated lipid nanodomains embedded in biological membrane models. *Applied Physics Letters*, 93:213901–3, 2008. [5]

I. Ofek, J. Goldhar, and Y. Keisari. Nonopsonic phagocytosis of microorganisms. *Annual Review of Microbiology*, 49:239–76, 1995. [72, 88]

L. G. Parratt. Surface studies of solids by total reflection of X-rays. *Physical Review*, 95(2):359 – 369, 1954. [47]

A. L. Patterson. The scherrer formula for X-ray particle size determination. *Physical Review*, 56:978–982, 1939. [45]

M. C. Phillips, R. Williams, and D. Chapman. On the nature of hydrocarbon chain motions in lipid liquid crystals. *Chemistry and Physics of Lipids*, 3:234–244, 1969. [7]

L. Pugliese, A. Coda, M. Malcovati, and M. Bolognesi. Three-dimensional structure of the tetragonal crystal form of egg-white avidin in its functional complex with biotin at 2.7 A resolution. *Journal of Molecular Biology*, 231(3):698–710, 1993. [91]

M. Quesada-Pérez, Callejas-Fernández, and R. Hidalgo-Álvarez. Interaction potentials, structural ordering and effective charges in dispersions of charged colloidal particels. *Advances in Colloid and Interface Science*, 95(2-3):295–315, 2002. [59]

J. Rädler and E. Sackmann. Imaging optical thickness and separation distances of phospholipid vesicles at solid surfaces. *Journal de Physique II*, 3(5):727–748, 1993. [72, 75]

I. Reviakine and A. Brisson. Formation of supported phospholipid bilayers from unilamellar vesicles investigated by atomic force microscopy. *Langmuir*, 16(4): 1806–1815, 2000. [22, 23]

J. G. Riess. Fluorous micro- and nanophases with biomedical perspective. *Tetrahedron*, 58(20):4113–4131, 2002. [3]

A. Rietveld and K. Simons. The differential miscibility of lipids as the basis for the formation of functional membrane rafts. *Biochimica et Biophysica Acta - Reviews on Biomembranes*, 1376(3):467–479, 1998. [3]

E. Sackmann and R. Merkel. *Lehrbuch der Biophysik*. Wiley-VCH Verlag GmbH & Co. KGaA, Weinheim, 1st edition, 2010. [23]

H. Sahly, Y. Keisari, E. Crouch, N. Sharon, and I. Ofek. Recognition of bacterial surface polysaccharides by lectins of the innate immune system and its contribution to defense against infection: the case of pulmonary pathogens. *Infection and Immunity*, 76(4):1322–1332, 2008. [72]

B. E. A. Saleh and M. C. Teich. *Fundamentals of Photonics*. John Wiley & Sons Inc., Hoboken, 2nd edition, 2007. [73]

J. Schilling, Sengupta, S. K. Goennenwein, A. R. Bausch, and E. Sackmann. Absolute interfacial distance measurements by dual-wavelength reflection interference contrast microscopy. *Physical Review E*, 69:021901–9, 2004. [72]

M. F. Schneider, D. Andelman, and M. Tanaka. Stripes of partially fluorinated alkylchains: Dipolar langmuir monolayers. *The Journal of Chemical Physics*, 122: 094717 – 5, 2005. [53]

M. F. Schneider, Z. Guttenberg, S. Schneider, K. Sritharan, V. M. Myles, U. Pamukci, and A. Wixforth. An acoustically driven microliter flow chamber on a chip (μFCC) for cell-cell and cell-surface interaction studies. *ChemPhysChem*, 9(4):641–645, 2008. [106]

K. Sengupta, H. Arana-Espinoza, L. Smith, P. Janmey, and D. Hammer. Spreading of neutrophils: From activation to migration. *Biophysical Journal*, 91(12):4638–4648, 2006. [76]

M. Seul and D. Andelman. Domain shapes and patterns: The phenomenology of modulated phases. *Science*, 267(5197):476–483, 1995. [27, 29, 35]

V. L. Shepherd, Y. C. Lee, P. H. Schlesinger, and P. D. Stahl. L-fuctose-terminated glycoconjugates are recognized by pinocytosis receptors on macrophages. *Proceedings of the National Academy of Sciences of the U.S.A.*, 78(2):1019–1022, 1981. [70]

J. R. Silvius and R. McElhaney. Effects of phospholipid acylchain structure on thermotropic phase properties. 2: Phosphatidylcholines with unsaturated or cyclopropane acyl chains. *Chemistry and Physics of Lipids*, 25(2):125 – 134, 1979. [7]

K. Simons and E. Ikonen. Functional rafts in cell membranes. *Nature*, 387:569–572, 1997. [69]

J. S. Singer and G. L. Nicolson. The fluid mosaic model of the structure of cell membranes. *Science*, 175(4023):720–731, 1972. [1]

D. M. Smilgies. High-resolution grazing-incidence scattering using a combination of analyzer crystal and linear detector. *Review of Scientific Instruments*, 74(9): 4041–4047, 2003. [43]

H. Steller. Mechanisms and genes of cellular suicide. *Science*, 267(5203):1445–1449, 1995. [89]

T. S. Suda, H. Hashimoto, M. Tanaka, T. Ochi, and S. Nagata. Membrane Fas ligand kills human peripheral blood T lymphocytes, and soluble Fas ligand blocks the killing. *Journal of Ex*, 186(12):2045–2050, 1997. [90]

M. Tanaka and E. Sackmann. Polymer-supported membranes as models of the cell surface. *Nature*, 437:656–663, 2005. [2, 72]

C. Tanford. The hydrophobic effect and the organization of living matter. *Science*, 200:1012–1018, 1978. [2]

M. E. Taylor, K. Bezouška, and K. Drickamer. Contribution to ligand binding by multiple carbohydrate-recognition domains in the macrophage mannose receptor. *The Journal of Biological Chemistry*, 267(3):1719–1726, 1992. [70, 71]

W. Thomas. Catch bonds in adhesion. *Annual Review of Biomedical Engineering*, 10:39–57, 2008. [105]

A. Thompson, I. Lindau, D. Attwood, Y. Liu, D. Gullikson, P. Pianetta, M. Howells, A. Robinson, K. Kim, J. Scofield, J. Kirz, J. Underwood, J. Kortright, G. Williams, and H. Winick. X-ray data booklet. http://xdb.lbl.gov, Lawrence Berkley National Laboratory, CA-USA, 2009. [50]

I. M. Tidswell, B. M. Ocko, and P. S. Pershan. X-ray specular reflection studies of silicon coated by organic monolayers (alkylsiloxanes). *Physical Review B*, 41(2): 1111–1128, 1990. [50]

S. Tristram-Nagle, H. I. Petrache, and J. F. Nagle. Structure and interactions of fully hydrated dioleoylphosphatidylcholine bilayers. *Biophysical Journal*, 75:917–925, 1998. [52]

A. S. Ulrich, M. Sami, and A. Watts. Hydration of DOPC bilayers by differential scanning calorimetry. *Biochim Biophys Acta*, 1191(1):225–230, 1994. [7]

T. K. Vanderlick and H. Möhwald. Mode selection and shape transitions of phospholipid monolayer domains. *The Journal of Physical Chemistry*, 94(2):886–890, 1990. [35]

S. L. Veach, K. Gawrisch, and S. L. Keller. Closed-loop miscibility gap and quantitative tie-lines in ternary membranes containing diphytanoyl PC. *Biophysical Journal*, 90:4428–4436, 2006. [3]

G. H. Vineyard. Grazing-incidence diffraction and the distorted-wave approximation for the study of surfaces. *Physical Review B*, 26:4146–4159, 1982. [46]

T. H. Watts, H. E. Gaub, and H. M. McConnell. T-cell-mediated association of peptide antigen and major histocompatibility complex protein detected by energy transfer in an evanescent wave-field. *Nature*, 320(6060):179–, 1986. [22]

R. M. Weis and H. M. McConnell. Two-dimensional chiral crystals of phospholipids. *Nature*, 310:47–49, 1984. [27]

A. Wixforth, C. Strobl, C. Gauer, A. Toegl, J. Scriba, and Z. Guttenberg. Acoustic manipulation of small droplets. *Analytical and Bioanalytical Chemistry*, 379(7-8): 982–991, 2004. [106]

S. Wurlitzer. *Statische und Dynamische Eigenschaften von Mikrostrukturen in Langmuir- Monolagen*. PhD thesis, Universität Leipzig, 2001. [28, 32, 38]

S. Wurlitzer, T. M. Fischer, and S. H. Equilibrium size of circular domains in langmuir monolayers. *The Journal of Chemical Physics*, 116(24):10877–10881, 2002. [31, 38, 68]

M. S. Yu, D. P. Curran, and T. Nagashima. Increasing fluorous partition coefficients by solvent tuning. *Organic Letters*, 7(17):3677–3680, 2005. [19]

S. Zamze, L. Martinez-Pomares, H. Jones, P. R. Taylor, R. S. Stillion, S. Gordon, and S. Y. C. Wong. Recognition of bacterial capsular polysaccharides and lipopolysaccharides by the macrophage mannose receptor. *The Journal of Biological Chemistry*, 277(44):41613–41623, 2002. [70, 72]

A. Zilker, M. Ziegler, and E. Sackmann. Spectral analysis of erytrocyte flickering in the 0.3–4-μm^{-1} regime by microinterferometry combined with fast image processing. *Physical Review A*, 46(12):7998–8001, 1992. [72]